Aix*Marseille université
Socialement engagée

NNT : 0000AIXM0000

THÈSE DE DOCTORAT

Soutenue à Aix-Marseille Université
Le 21 Février à Marseille par

Karthik BHAIRAPURADA

Study of Thermoacoustic Instabilities using the Lattice Boltzmann Method

Discipline
Sciences pour l'Ingénieur

Spécialité
Mécanique et physique des fluides

École doctorale
ED 353 : Sciences pour l'Ingénieur : Mécanique, Physiques, Micro et Nanoélectronique.

Laboratoire/Partenaires de recherche
M2P2 : Laboratoire de Mécanique, Modélisation et Procédés Propres

Composition du jury

Françoise BAILLOT Professeure, CORIA de Rouen, France	Rapporteure
Vadim KURDYUMOV Senior Researcher, CIEMAT, Espagne	Rapporteur
Laurent GICQUEL Senior Researcher, CERFACS, France	Examinateur
Luc VERVISCH Professeur, INSA de Rouen, France	Examinateur
Julien FAVIER Professeur, AMU, France	Président
Pierre BOIVIN Chargé de Recherche, CNRS, France	Directeur de thèse
Bruno DENET Professeur, AMU, France	Co-Directeur de thèse

M2P2 cnrs Ecole Doctorale ED 353 Sciences Pour l'Ingénieur Centrale Marseille

Affidavit

I, undersigned, Karthik Bhairapurada, hereby declare that the work presented in this manuscript is my own work, carried out under the scientific direction of Pierre Boivin, and Bruno Denet, in accordance with the principles of honesty, integrity and responsibility inherent to the research mission. The research work and the writing of this manuscript have been carried out in compliance with both the french national charter for Research Integrity and the Aix-Marseille University charter on the fight against plagiarism.

This work has not been submitted previously either in this country or in another country in the same or in a similar version to any other examination body.

Marseille, 10 December 2023



Karthik Bhairapurada

Cette œuvre est mise à disposition selon les termes de la Licence Creative Commons Attribution - Pas d'Utilisation Commerciale - Pas de Modification 4.0 International.

Liste de publications et participation aux conférences

Liste des publications réalisées dans le cadre du projet de thèse:

1. **Karthik Bhairapurada**, Bruno Denet and Pierre Boivin. A Lattice-Boltzmann study of premixed flames thermo-acoustic instabilities. Combustion and Flame, 240: 112049, 2022.
2. Song Zhao, **Karthik Bhairapurada**, Muhammad Tayyab, Renaud Mercier, and Pierre Boivin. Lattice-boltzmann modeling of the quiet and unstable preccinsta burner modes. Computers and Fluids, 260:105898, 2023
3. **Karthik Bhairapurada**, Alejandro Millán-Merino, Song Zhao, Bruno Denet and Pierre Boivin. Sound generation by Hydrogen flame annihilation. (En preparation)

Participation aux conférences au cours de la période de thèse :

1. 18th International Conference on Numerical Combustion (ICNC2022), 2022, San Diego, USA.
2. 11th European Combustion Meeting (ECM2023), 2023, Rouen, France

Abstract

In the quest to address global warming, renewable energy has emerged as a critical focus. Yet, the reality of our current energy landscape renders the complete abandonment of combustion technologies unfeasible. Innovations such as 'Lean Burn' combustion and the integration of cleaner fuels like Hydrogen offer a compromise, balancing immediate energy demands with environmental objectives. However, these advancements also introduce significant challenges, especially the heightened risk of thermoacoustic instabilities in combustion systems, which could lead to catastrophic failures.

Traditional experimental methods for studying and mitigating these instabilities are not only prohibitively expensive but also often impractical. Consequently, there is a growing advocacy for the adoption of advanced numerical methods as efficient and cost-effective alternatives. This thesis underscores the potential of one such method, known as the Lattice Boltzmann Method (LBM). LBM is a numerical method renowned for its distinctive algorithmic structure that facilitates linear interactions between adjacent nodes and enables the local evaluation of non-linear terms. These inherent features endow LBM with computational efficiency and low dissipation properties for acoustics transport, making it a promising tool for simulating flame-acoustic interactions and addressing thermoacoustic instabilities.

The research validates the capabilities of LBM in effectively resolving such instabilities. Through foundational affirmations of simple flame-acoustic interactions and simulations within narrow channels, the reliability of the method for investigating combustion instabilities across various scenarios is established. Furthermore, the thesis also explores the field of 'Combustion Noise', demonstrating the potential of LBM in investigating sound generation and propagation phenomena, particularly in hydrogen-fueled combustion scenarios. Finally, the robustness and versatility of LBM in handling thermoacoustic instabilities of turbulent reactive flows in complex geometries are demonstrated through the simulation of an aeronautical burner configuration called PRECCINSTA.

Overall, guided by the importance of innovative numerical methods in bridging the gap between current energy needs and long-term environmental sustainability, this thesis underscores the potential of LBM. Through varied investigations, it not only highlights the capabilities of the method but also contributes to a broader understanding of thermoacoustic phenomena across various settings.

Keywords: Lattice Boltzmann Method, Thermoacoustic Instabilities, Flame-acoustic interaction, Combustion noise, Flame annihilation, Preccinsta burner

Resumé

Dans la lutte contre le réchauffement climatique, les énergies renouvelables sont devenues une priorité essentielle. Pourtant, la réalité de notre paysage énergétique actuel rend l'abandon complet des technologies de combustion non réalisable. Des innovations telles que la combustion 'Lean Burn' et l'intégration de carburants plus propres comme l'Hydrogène offrent un compromis, équilibrant les demandes énergétiques immédiates avec les objectifs environnementaux. Cependant, ces avancées introduisent également des défis significatifs, en particulier le risque accru d'instabilités thermoacoustiques dans les systèmes de combustion, qui pourraient conduire à des échecs catastrophiques.

Les méthodes expérimentales traditionnelles pour étudier et atténuer ces instabilités sont non seulement prohibitivement coûteuses, mais aussi souvent impraticables. Par conséquent, Il existe une motivation croissante pour l'adoption de méthodes numériques avancées comme alternatives efficaces et rentables. Cette thèse explore le potentiel d'une telle méthode, connue sous le nom de Méthode de Lattice Boltzmann (LBM). La LBM est une méthode numérique renommée pour sa structure algorithmique distinctive qui facilite les interactions linéaires entre les nœuds adjacents et permet l'évaluation locale des termes non linéaires. Ces caractéristiques inhérentes confèrent à la LBM une efficacité computationnelle et des propriétés de faible dissipation pour le transport acoustique, en faisant un outil prometteur pour simuler les interactions flamme-acoustique et adresser les instabilités thermoacoustiques.

Ce travail explore les capacités de la LBM pour résoudre de telles instabilités. Ceci est réalisé via des études fondamentales, telles que des interactions élémentaires flamme/acoustique et des simulations d'écoulements dans des canaux étroits. Ces cas académiques permettent d'établir la validité de la méthode dans ce domaine de la combustion. Pour aller plus loin, le bruit de combustion généré par des flammes canoniques d'hyrdogène est également étudié, montrant le potentiel de la méthode pour comprendre de nouveaux phénomènes. Dans le dernier chapitre, la robustesse et la versatilité de la LBM sont mises en exergue pour la prédiction d'instabilités thermoacoustiques d' écoulements réactifs turbulents dans des géométries complexes. Pour cette dernière démonstration le brûleur PRECCINSTA, un injecteur expérimental de type aéronautique, a été retenu.

Dans l'ensemble, guidée par l'importance des méthodes numériques innovantes pour combler le fossé entre les besoins énergétiques actuels et la durabilité environnementale à long terme, cette thèse souligne le potentiel de la LBM. À travers une recherche variée, elle met non seulement en évidence les capacités de la méthode, mais contribue également à une compréhension plus large des phénomènes thermoacoustiques dans divers contextes.

Acknowledgements

I extend my sincere gratitude to my supervisors, Pierre BOIVIN and Bruno DENET, for their invaluable guidance throughout my thesis.

Pierre BOIVIN, in particular, has been instrumental in my academic and personal development, offering me opportunities to explore my passion from my Master's internship to my PhD. His patience and mentorship, particularly when facing challenges, have profoundly shaped my approach to both academic challenges and life perspectives. This work would not have been possible without his constant support. I have learned immensely from him and would like to extend my sincere appreciation for his dedicated efforts.

Bruno DENET's knowledge and expertise in explaining complex theories about instabilities has greatly enhanced my understanding and interest in our field. His insightful feedback and guidance during this thesis have been indispensable. The time spent discussing theoretical analysis has greatly enriched my learning experience, for which I am profoundly grateful.

I must also acknowledge Song ZHAO for his continuous guidance and encouragement, which have been pivotal in my growth. His vast knowledge, though sometimes overwhelming, has consistently pushed me to excel. I am particularly thankful for his encouraging words after each of my presentations, a kindness that words alone cannot fully express.

It would be amiss not to mention the impactful guidance and knowledge that Alejandro imparted during his brief tenure at M2P2. His insights, though shared during a brief period, have left a profound impact on my work. Equally, my heartfelt thanks go to Tayyab for his warm welcome to M2P2 and for adeptly showing me the ins and outs of our extensive code. Collaborating with him on various projects was not only effortless but also a thoroughly enjoyable and enriching experience. I appreciate the contributions of post-docs particularly Gabriel and Said, whose discussions have been consistently helpful.

My gratitude extends to all my colleagues including, Giacomo, Gang, Marc, Stefano, Marcello, Felix, Ziyin, Ziwen, Jose, and Mostafa for creating a supportive lab environment, and also to my other friends Sunil, Sai, Nishta, Uday, Preran, and Jeevitha for their unwavering support and camaraderie.

Finally, I would like to thank my parents and the family, whose steadfast support has been the foundation of all my achievements. This journey and its successes if any, are a tribute to them.

Table of Contents

Introduction **1**

1 Premixed Flame Combustion **7**
1.1 Introduction . . . 7
1.2 Governing equations for Reacting flows . . . 8
1.2.1 Conservation laws . . . 8
1.2.2 Closure Models . . . 10
1.3 Premixed Flames . . . 13
1.3.1 Asymptotic Analysis . . . 14
1.3.2 Parameters of Interest . . . 16
1.4 Summary . . . 19

2 Premixed Flame Combustion Instabilities **20**
2.1 Introduction . . . 20
2.2 Hydrodynamic Instabilities . . . 21
2.2.1 Darrieus-Landau Mechanism . . . 21
2.2.2 Corrections to the DL Instability Model . . . 25
2.3 Thermoacoustic Instabilities . . . 29
2.3.1 Flame Response to Acoustic waves . . . 29
2.3.2 Combustion Noise . . . 32
2.3.3 Coupling and Amplification of Instability . . . 34
2.3.4 Flame propagation in Channel . . . 36
2.4 Summary . . . 42

3 Numerical Combustion with Lattice Boltzmann Method **43**
3.1 Introduction . . . 43

3.2 Lattice Boltzmann Method . . . 44
3.2.1 Boltzmann Equation . . . 44
3.2.2 Discrete Velocity Boltzmann Equation . . . 46
3.2.3 Lattice Boltzmann Equation . . . 47
3.2.4 Typical Algorithm of Lattice Boltzmann Method . . . 49
3.3 Hybrid Lattice Boltzmann Method for Reactive Flows . . . 54
3.3.1 Hybrid Solver . . . 55
3.3.2 Collision Kernels . . . 56
3.3.3 Pressure based LBM . . . 57
3.4 Boundary Conditions . . . 59
3.4.1 NRI-NSCBC . . . 61
3.5 Summary . . . 62

4 LBM for Premixed Laminar Flame Instabilities 64
4.1 Introduction . . . 64
4.2 Preliminary numerical definitions . . . 66
4.3 Darrieus-Landau Instability . . . 66
4.3.1 Impact of Boundary Conditions on the Cut-off Wavelength . . . 67
4.3.2 Symmetric and non-symmetric flames in a channel . . . 69
4.4 Acoustically forced flames . . . 72
4.4.1 Parametric instability of freely propagating flames . . . 72
4.5 Self-excited flames in narrow channels . . . 75
4.5.1 Eigenmode analysis . . . 76
4.5.2 Parametric studies on the gain of instability . . . 78
4.5.3 Flame dynamics in long-narrow channels . . . 82
4.6 Conclusion . . . 88

5 Sound Generation due to Combustion 89
5.1 Introduction . . . 89
5.2 LBM for Acoustic wave transport . . . 90
5.2.1 Planar Standing Wave . . . 91
5.2.2 Planar pulse propagation . . . 93
5.2.3 2D Acoustic Pulse . . . 96
5.3 Sound generation and propagation . . . 98
5.3.1 Acoustically excited premixed flames . . . 98
5.3.2 Setups to study sound generation during flame annihilation . . . 102
5.3.3 Effect of Lewis Number . . . 106

5.4 Sound generation by Hydrogen flames . . . 108
5.4.1 Effect of Chemistry . . . 109
5.4.2 Parametric study of sound generation by hydrogen flames . . . 111
5.4.3 Pressure peaks in Planar flame Annihilation . . . 113
5.5 Conclusion . . . 119

6 Large Eddy Simulation of PRECCINSTA Burner 121
6.1 Introduction . . . 121
6.2 Filtered LES Equations for Reactive Flows . . . 123
6.2.1 Closure Models . . . 123
6.3 Preccinsta burner . . . 126
6.3.1 Numerical Setup . . . 127
6.4 Non-Reacting case . . . 129
6.5 Reacting case . . . 130
6.5.1 Quiet case ($\phi = 0.83$) . . . 130
6.5.2 Pulsating case ($\phi = 0.7$) . . . 133
6.6 Heat Losses . . . 140
6.7 Summary . . . 142

Conclusion and Perspectives 144

A Simulation parameters 158

B F→P chemistry model 160

List of Figures

1.1 Internal flame structure 16

2.1 Deviation of Streamlines in a Conical flame 23
2.2 Illustration of Darrieus-Landau Instability 24
2.3 Influence of Interface Curvature 26
2.4 Theoretical Darrieus Landau growth rate 28
2.5 Typical Theoretical Thermoacoustic Instability Diagram 31
2.6 Frequency response of an Acoustically Excited Conical Flame 33
2.7 Illustration of the feedback process responsible for combustion instability 35
2.8 Illustration of flame inside a channel 39

3.1 Illustration of D3Q19 lattice 46
3.2 Streaming step 50
3.3 Hybrid Lattice Boltzmann algorithm 60

4.1 Growth/decay of DL instability in a periodic domain 68
4.2 Growth/Decay of DL instability in between slip walls 69
4.3 Growth/Decay of DL instability in between non-slip walls 69
4.4 Flame consumption speed in slip and non-slip walls 70
4.5 Symmetric and non-symmetric flame shapes 71
4.6 Schematics of externally excited flames 72
4.7 Stability diagrams for parametrically excited flames 73
4.8 Illustration of parametrically excited flames 74
4.9 A sketch of the narrow channel under consideration. 76
4.10 Eigenmodes of a channel with flame propagation 77
4.11 Amplification of instabilities on symmetric and non-symmetric flames . 79
4.12 Comparision between ProLB and NTMIX 80

4.13 Investigation of the impact of channel width on thermoacoustic instability 82
4.14 Study of self-excited thermoacoustic instability within a non-slip channel 83
4.15 Flame dynamics due to the instability within a non-slip channel 84
4.16 Study of self-excited thermoacoustic instability within a slip channel . . 86
4.17 Flame dynamics due to the instability within a slip channel 87
4.18 Three-quarter wave mode 87

5.1 Dissipation and Dispersion properties of LBM: Setup 1 93
5.2 Dissipation and Dispersion properties of LBM: Setup 2 95
5.3 Dissipation and Isotropic properties of LBM: Setup 3 97
5.4 Schematics of computational domain 98
5.5 Sound generation and propagation 100
5.6 Pressure fluctuation signals during Flame annihilation and Pinch-off . . 101
5.7 Correlation between HRR fluctuations and sound generation 102
5.8 Configuration of 1D planar and circular flame annihilation. 103
5.9 Planar flame annihilation 104
5.10 Circular flame annihilation 105
5.11 Lewis number effects: Planar flames' annihilation 107
5.12 Lewis number effects: Circular flame implosion 108
5.13 Effects of chemistry: Planar flames' annihilation 110
5.14 Effects of chemistry: Circular flame implosion 111
5.15 Influence of the Lewis Number on sound generation 112
5.16 Influence of the ambient pressure on sound generation 114
5.17 Effect of Lewis number: 1S-H_2-Air Model 115
5.18 Different approximations of effective Lewis numbers 116
5.19 Effect of Lewis number: Detailed-H_2-Air Model 117
5.20 Effect of equivalence ratio and elevated pressures 117
5.21 Planar flames pressure peak correlation with effective lewis number and ϵ 118

6.1 Preccinsta Burner 127
6.2 Illustration of Preccinsta Mesh Configuration 128
6.3 Illustration of Precessing Vortex Core in Cold flows 129
6.4 Illustration of Quiet mode of Preccinsta burner 131
6.5 Cut-plane Statistics for the Quiet case 132
6.6 Comparison between the Quiet and Pulsating modes of Preccinsta . . . 134
6.7 Cut-plane Statistics for the pulsating case 136
6.8 Acoustic Analysis of the Pulsating case 137

6.9 Rayleigh Criterion for Pulsating case 137
6.10 Self-sustained oscillation cycle of Pulsating Preccinsta mode 138
6.11 Cut-plane Statistics for the quiet case with non-adiabatic walls 141
6.12 Flame shapes with and without heat-losses on the wall boundaries . . . 142

List of Tables

3.1 Discrete velocities $\boldsymbol{c}_i$ and weights w_i of a D3Q19 velocity set. 47
3.2 Generic structure of an LBM 53

5.1 Relative dispersion and dissipation numerical error 92

6.1 Simulation parameters for the quiet and pulsating modes of Preccinsta. 130

A.1 Parameters used in Sec. 4.3 and Sec. 4.5 158
A.2 Parameters used in Sec. 4.4 159
A.3 Mass fraction composition 159

B.1 NASA polynomials for $F \rightarrow P$ chemistry 161
B.2 Parameters set for $F \rightarrow P$ chemistry 162

Introduction

Combustion in the Age of Renewables

In our battle against global warming, renewable energy sources have taken center stage, and rightly so. The urgency to transition away from fossil fuels has never been more pressing. Technologies such as solar panels, wind turbines, and hydroelectric dams hold the promise of a cleaner, more sustainable future. However, the intermittent nature of some of these renewables, poses a formidable challenge: the need for consistent and reliable power generation. It is within this context that combustion, despite its environmental drawbacks, remains a reliable and high-energy-density source. Therefore, it is likely to retain its significance in our energy landscape, possibly complementing renewable sources. This becomes particularly evident in sectors where the energy demands have yet to discover a viable, carbon-neutral alternative.

For instance, the world of commercial aviation highlights this predicament. While the allure of fully electric, long-haul airplanes is enticing, practical considerations make it elusive [91]. The energy requirements of an 80-ton Airbus A320 would demand approximately 900 tons of state-of-the-art batteries, emphasizing the challenges faced in replacing combustion in such sectors. Additionally, the pursuit of space exploration underscores another realm where combustion remains pivotal. The propulsion systems of rockets are a testament to the formidable power and efficiency that combustion processes can offer [98].

Given these scenarios, rather than viewing combustion as an adversary or relegating it to a secondary role in our efforts to address climate change, there is a need to innovate and refine existing combustion technologies. By unlocking the potential for cleaner and more efficient combustion, we can strike a delicate balance between fulfilling our immediate energy requirements and advancing our long-term environmental objectives.

Substantial progress has already been achieved in pursuit of this objective. One notable advancement is the widespread adoption of the "RQL" (Rich-Quench-Lean) architecture for the gas turbine combustion systems. In this design, an enriched primary zone is initially established to bolster stability, promptly followed by swift mixing, which reduces the temperature and consequently diminishes the production of NO_x(nitrogen oxides). However, this method is not very effective in suppressing soot oxidation.

A more recent shift in focus has been towards the "Lean Burn" methodology, also known as Lean Premix Prevapourised (LPP). In this approach, the fuel nozzle is either retracted or the fuel injection is distributed circumferentially, ensuring a well-evaporated mixture enters the combustion chamber. The resulting flames, resembling premixed flames, exhibit both low NO_x and soot levels due to the reduction in regions with stoichiometric or fuel-rich compositions. Furthermore, in a bid to reduce carbon emissions, significant research efforts have been directed towards either completely replacing hydrocarbon fuels with hydrogen or using them in tandem with other carbon-free fuels. Both of these innovations, the adoption of Lean Burn and the integration of hydrogen fuel, although significant, introduce new challenges due to their heightened susceptibility to thermoacoustic instabilities.

Thermoacoustic Instabilities

Thermoacoustic instabilities arise due to the coupled interaction between the oscillatory flow (mostly due to acoustic waves) and the unsteady heat release of the flame, giving rise to undesirable, large-amplitude oscillations corresponding to one or more natural acoustic modes of a combustion system. In general, the occurrence of these instabilities is problematic because they produce large amplitude pressure and velocity oscillations that could result in thrust oscillations, leading to severe vibrations of the whole system. Nonetheless, the challenges posed by these instabilities are not novel; they have persisted since the inception of high-performance propulsion systems for aeronautical and space applications [57]. These instabilities have, at times, resulted in catastrophic failures, with one of the most infamous cases being the F-1 engine propelling the Saturn V during the Apollo missions of the 1960s and 1970s [28]. In the early stages of its development, the combustion instabilities were so severe that they caused the complete destruction of the combustion chamber. To address this issue, engineers from Rocketdyne and NASA embarked on a trial-and-error test campaign, primarily focusing on the spatial layout of the injectors on the injection plate as the main design parameter. While this strategy

eventually led to the creation of one of the most powerful liquid rocket engines ever built, it came at a significant cost, involving the destruction of numerous prototypes and substantial budget overruns.

However, the current landscape is distinct from the Cold War-era space race, and the challenges faced by commercial aviation are mounting. Allocating billions for the assessment and enhancement of these low-emssion systems is neither practical nor justifiable. This is where the advancements in numerical methods become invaluable, offering an efficient, cost-effective pathway to address these issues.

Numerical Methods: A Modern Solution

The evolution of computational power over the last few decades has revolutionized all fields of engineering, with numerical methods standing at the forefront of this transformation. These methods, essentially mathematical algorithms used to model complex physical phenomena, have become indispensable tools in addressing various issues, where experimental trial-and-error can be prohibitively expensive and/or hazardous. This approach now termed as Computational Fluid Dynamics (CFD) has become pivotal in addressing challenges as complex as combustion/thermoacoustic instabilities. Engineers can now harness the power of simulations (CFD) not only to predict combustion behaviors but also to access data that was once out of reach. They can optimize parameters and pinpoint potential issues at just a fraction of the costs traditionally associated with such endeavors.

However, while numerical methods offer significant advantages, they also come with their unique set of intrinsic challenges. Foremost among these is ensuring the accuracy and reliability of simulations, which necessitates rigorous validation against empirical data. Moreover, simulating even a scaled-down model of a gas turbine can be resource-intensive due to the sheer complexity involved, not to mention the plethora of modeling issues one might encounter. For instance, while studying thermoacoustic instabilities, the stark disparity in timescales, with thermoacoustic oscillations on the order of $10^{-2}\,\mathrm{s}$ and flame chemical timescales as brief as $10^{-9}\,\mathrm{s}$, coupled with a vast range of length scales spanning from acoustic wavelengths of $50\,\mathrm{cm}$ to flame thicknesses smaller than $0.1\,\mathrm{mm}$, present formidable obstacles for achieving both accurate and computationally efficient simulations.

Potential of Lattice Boltzmann Method

In light of these challenges, we turn our attention to a numerical method rooted in the kinetic theory of gases known as the Lattice Boltzmann Method (LBM). The distinctive algorithmic structure of this method, primarily composed of "Stream and Collide" steps, facilitates linear interactions between adjacent nodes and enables the evaluation of non-linear terms locally within each node. These inherent features have endowed the LBM with two favorable attributes: computational efficiency, arising from limited interactions between nodes, and low dissipation properties for acoustics transport [64].

Unsurprisingly, the LBM has gained significant prominence in the field of aeroacoustics [95]. More recently, its potential has been demonstrated in simulating reactive flows with remarkable computational efficiency [10]. Given this low-dissipation for acoustics transport and its cost-effective capabilities for simulating reactive flows, a pertinent question arises: **Can it effectively resolve flame-acoustic interactions and tackle thermoacoustic instabilities?** This question forms the cornerstone of our thesis research.

Objectives of the PhD research

The primary objective of our research is to validate the capabilities of the Hybrid-LBM method [10, 36], in effectively resolving thermoacoustic instabilities. Our research spans from systematically validating straightforward flame-acoustic interactions to modeling thermoacoustic instabilities in a complex aeroburner. While validating canonical cases is a primary goal, we also strive to enhance our understanding of flame-acoustic interactions and thermoacoustic instabilities within these scenarios. Additionally, part of this thesis centers on the sound generation by flames, often termed "Combustion Noise", with a specific focus on examining the acoustic characteristics associated with the implosion of hydrogen flames. A detailed outline of the thesis is provided below.

Outline of the thesis

The thesis consists of six chapters that collectively explore the capabilities of the Lattice Boltzmann Method in simulating flame-acoustic interactions and addressing thermoacoustic instabilities.

- **Chapter 1:** This chapter provides an introduction to the fundamental governing equations of combustion. It focuses specifically on premixed flames and employs Activation Energy Asymptotics (AEA) to delve into their internal structure. This

analysis serves as the foundation for the subsequent exploration of instabilities affecting premixed flames. The chapter also highlights the critical parameters that characterize these flames.

- **Chapter 2:** This chapter explores the instabilities impacting premixed flames, focusing on the hydrodynamic Darrieus Landau Instability and thermoacoustic instability. It delves into the mechanisms responsible for generating and amplifying these instabilities, employing both physical reasoning and theoretical analyses. Additionally, the chapter derives the system eigenmodes associated with flame propagation in an semi-open channel.

- **Chapter 3:** This chapter provides a comprehensive overview of the Hybrid Lattice Boltzmann method employed in the study. It commences with a general introduction to LB Methods, outlines the fundamental algorithm, and proceeds to detail the specific modifications required for simulating reactive flows, specifically the Pressure-based Hybrid Lattice Boltzmann Method.

- **Chapter 4:** This chapter is dedicated to the comprehensive evaluation of the capability of the Lattice Boltzmann Method in accurately simulating flame-acoustic interactions and addressing thermoacoustic instabilities in narrow channels. The assessment begins with the validation of the accuracy of the method in simulating the response of the flame to external acoustic excitation. Subsequently, it highlights the correspondence between the generated thermoacoustic instability and the intrinsic eigenmodes of the channel. Additionally, our findings related to self-excited thermoacoustic instability in channels are cross-validated through comparison with existing literature and numerical simulations. Beyond these primary objectives, the chapter delves into exploring the impact of variations in boundary conditions, flame shapes, and channel dimensions on channel-bound combustion instabilities, thus enhancing the understanding of this intricate phenomenon.

- **Chapter 5:** This chapter delves into the intricacies of sound generation in combustion processes, examined using the Lattice Boltzmann Method. It begins with an assessment of our method, emphasizing its capability to simulate acoustic transport by focusing on its dissipative and isotropic properties crucial for analyzing sound propagation. A significant portion of the chapter is dedicated to exploring the mechanisms of sound generation, with a particular emphasis on the Flame Annihilation process. The chapter also addresses the complexities of studying sound generation when employing hydrogen as a fuel source. It sheds

light on the challenges associated with using simplified chemistry models in such scenarios. Additionally, the chapter investigates the numerous factors that influence the amplitude of sound generated during hydrogen-air combustion, providing insights into this complex phenomenon.

- **Chapter 6:** This chapter demonstrates the potential of Lattice Boltzmann Methods (LBM) in resolving thermoacoustic instability, even in complex industrial scenarios characterized by intricate geometries, multilevel refinements, and high Reynolds numbers. The chapter begins by introducing the turbulent models used in conjunction with LBM, essential for conducting a reactive Large Eddy Simulation (LES) of a micro gas turbine aeroburner known as "Preccinsta." The approach involves validating the LBM-LES method on various thermal configurations of this burner, ranging from cold to unstable reactive configurations. The analysis within this chapter delves into the assessment of thermoacoustic instability in the burner, comparing the findings with experimental data and prior research. Furthermore, the chapter briefly emphasizes the significance of considering heat losses at the boundaries in such simulations.

The thesis concludes with a summary of findings and outlines the potential avenues for future research.

Chapter 1

Premixed Flame Combustion

Contents

1.1 Introduction 7

1.2 Governing equations for Reacting flows 8

1.2.1 Conservation laws 8

1.2.2 Closure Models 10

1.3 Premixed Flames 13

1.3.1 Asymptotic Analysis 14

1.3.2 Parameters of Interest 16

1.4 Summary 19

1.1 Introduction

Combustion phenomena encompass a wide range of combustion modes and regimes, which can be broadly categorized into: fully premixed and non-premixed, and turbulent and laminar combustion. While turbulent combustion underlies many industrial and natural phenomena, providing a complete description remains a significant challenge, even for advanced computational tools, not to mention theoretical analysis. Therefore, the study of laminar flames, particularly premixed laminar flames, provides a compelling starting point for delving into the complexities of combustion.

However, a complete description of premixed flames is not straightforward either, as the description of the burning process (chemical kinetics) can involve hundreds, if not thousands, of reactions. Fortunately, due to the disparity in length and time scales

involved in laminar premixed flames, the entire burning process can be adequately described by a simplified irreversible reaction that transforms the fresh fuel mixture into burned products. Leveraging this fact, Activation Energy Asymptotics (AEA) [58, 112, 115] has been developed, which now serves as the fundamental framework for understanding the physics of premixed laminar flames.

In this chapter, we present the fundamental equations governing most of the combustion processes. We introduce the structural characteristics of premixed flames using Activation Energy Asymptotics (AEA) and provide a concise overview of the key parameters that define premixed flames. This knowledge will serve as a crucial foundation for our subsequent theoretical analysis of flame instabilities and other critical modeling aspects of turbulent combustion.

1.2 Governing equations for Reacting flows

A comprehensive examination of fluid flows, whether through analytical or numerical methods, necessitates an in-depth understanding of the governing equations that define them. These equations, known collectively as the Navier-Stokes (NS) system, are derived from first principles and encompass the conservation of mass, momentum, and energy. They form the backbone of fluid dynamics.

1.2.1 Conservation laws

In our investigation, which centers on reactive flows with multiple species, we utilize the classical, fully compressible Navier-Stokes equations in their conservative form. The Einstein notation representation of these equations is provided below:

- **Conservation of Mass :** The equations governing the conservation of mass are given by:

$$\boxed{\frac{\partial \rho Y_k}{\partial t} + \frac{\partial \rho u_\alpha Y_k}{\partial x_\alpha} = \frac{\partial J_\alpha^k}{\partial x_\alpha} + \dot{\omega}_k} \tag{1.1}$$

  Equation (1.1) outlines the conservation of mass for each individual species k, where the index k ranges from 1 to N_{sp}, representing the total number of species present. Species are characterized by their mass fractions Y_k, denoted as $Y_k = m_k/m$, where m_k is the mass of the individual species and m is the total mixture mass.

In addition, u_α denotes the α-th component of velocity. The terms J^k_α and $\dot{\omega}_k$ correspond to the species diffusion and chemical source terms respectively, which are be subject to modeling.

And given that mass remains conserved throughout the chemical process, the summation of the individual species mass conservation equations eq.(1.1) leads to the total mass conservation, or continuity equation:

$$\boxed{\frac{\partial \rho}{\partial t} + \frac{\partial \rho u_\alpha}{\partial x_\alpha} = 0} \tag{1.2}$$

- **Conservation of Momentum :** Derived from the Newton's second law of motion, the equation governing the conservation of momentum is expressed as:

$$\boxed{\frac{\partial \rho u_\beta}{\partial t} + \frac{\partial \rho u_\beta u_\alpha}{\partial x_\alpha} = -\frac{\partial p}{\partial x_\beta} + \frac{\partial \mathcal{T}_{\alpha\beta}}{\partial x_\alpha}} \tag{1.3}$$

Equation (1.3) captures the balance of momentum within a Newtonian fluid. In this equation, p denotes pressure and $\mathcal{T}_{\alpha\beta}$ represents the viscous tensor. If the viscous tensor is absent, Equation (1.3) simplifies to the Euler equations. The viscous tensor $\mathcal{T}_{\alpha\beta}$ is also determined through modeling.

- **Conservation of Energy :** Derived from the first law of thermodynamics, the equation governing energy conservation is expressed as:

$$\boxed{\frac{\partial \rho E}{\partial t} + \frac{\partial \rho u_\alpha H}{\partial x_\alpha} = \frac{\partial \mathcal{T}_{\alpha\beta} u_\beta}{\partial x_\alpha} - \frac{\partial q_\alpha}{\partial x_\alpha}} \tag{1.4}$$

Here, H represents the total enthalpy, given by $E + p/\rho$, and E is the total energy consisting of internal energy e and kinetic energy κ:

$$E = e + \kappa = h - \frac{p}{\rho} + \frac{1}{2}u^2 \tag{1.5}$$

Additionally, q_α in Equation (1.4) represents the energy flux term, subject to modeling.

Several terms within the Navier-Stokes system remain unresolved and require further explicit modeling. The constitutive relations employed to address these aspects are given in the upcoming section.

1.2.2 Closure Models

- **Thermodynamic Closure :** The Ideal Gas Equation of State (EOS) serves as a closure to the under-determined NS system.

  Internal energy (e) and enthalpy (h) are linked to the temperature T and mass fractions Y_k through the classical NASA polynomials [59].

$$h = \sum_{k=1}^{N_{SP}} (Y_k h_k), \quad h_k = \underbrace{\int_{T_0}^{T} c_{p,k}(\theta) d\theta}_{\text{sensible}} + \underbrace{\Delta^0 h_k}_{\text{chemical}} \tag{1.6}$$

$$\begin{aligned} \frac{C_{p,k}}{R} &= a_1 + a_2 T + a_3 T^2 + a_4 T^3 + a_5 T^4, \\ \frac{h_k}{RT} &= a_1 + a_2 \frac{T}{2} + a_3 \frac{T^2}{3} + a_4 \frac{T^3}{4} + a_5 \frac{T^4}{5} + \frac{a_6}{T}, \end{aligned} \tag{1.7}$$

  Here, $c_{p,k}$ signifies the constant pressure heat capacity of species k, and $\Delta^0 h_k$ is the formation enthalpy assigned to each species at the reference temperature ($T_0 = 298.15$K). The numerical coefficients a_n values can be obtained from [71]. Temperature T can be determined using h_k and y_k through the Newton iterative procedure [42].

  Subsequently, the pressure p, associated with density ρ, temperature T and mass fractions Y_k is expressed by:

$$p = \sum_{k=1}^{N_{sp}} p_k = \sum_{k=1}^{N_{sp}} \rho_k \frac{R}{W_k} T = \rho \frac{R}{W} T \tag{1.8}$$

  Here, $R = 8.3145 \text{J mol}^{-1} \text{K}^{-1}$ is the universal gas constant and the mean molecular weight W is associated with mixture through mass fractions and molecular weight of each species (W_k) as:

$$\frac{1}{W} = \sum_{k=1}^{N_{sp}} \frac{Y_k}{W_k} \tag{1.9}$$

- **Transport closure :** The constitutive relations supplementing the NS system for the unresolved terms that govern the transport are given by:

  - **Viscous Stress tensor ($\tau_{\alpha\beta}$) :** For a Newtonian fluid, considering stokes hypothesis, $\mathcal{T}_{\alpha\beta}$ is expressed as

$$\mathcal{T}_{\alpha\beta} = \mu\left(-\frac{2}{3}\frac{\partial u_\gamma}{\partial x_\gamma}\delta_{\alpha\beta} + \frac{\partial u_\alpha}{\partial x_\beta} + \frac{\partial u_\beta}{\partial x_\alpha}\right) + \eta_B \frac{\partial u_\gamma}{\partial x_\gamma}\delta_{\alpha\beta} \tag{1.10}$$

Here, μ represents the dynamic viscosity, which is temperature-dependent and follows a power-law relationship:

$$\mu = \mu_0 \left(\frac{T}{T_0}\right)^{\beta_v}, \tag{1.11}$$

In this equation, μ_0 and T_0 represent the reference dynamic viscosity and temperature respectively, which are chosen based on the gas mixture.

Additionally, in the eq.(1.10), η_B signifies bulk/volume viscosity, and it is set to zero in our investigation of low-Mach combustion flows. The Kronecker symbol $\delta_{\alpha\beta}$ is defined as $\delta_{\alpha\beta} = 1$ if $\alpha = \beta$, and 0 otherwise.

– **Species diffusion flux (J_α^k) :** Using the Hirschfelder and Curtiss approximation, J_α^k is expressed as:

$$J_\alpha^k = -\rho V_{k,\alpha} Y_k = -\rho D_k \frac{W_k}{W}\frac{\partial X_k}{\partial x_\alpha} + \underbrace{\rho \sum_{k=1}^{N} D_k \frac{W_k}{W}\frac{\partial X_k}{\partial x_\alpha} Y_k}_{\text{correction velocity term}} \tag{1.12}$$

where for each species k: D_k is the molecular diffusion coefficient, $V_{k,\alpha}$ is the α-th component of diffusion velocity V_k and X_k is the molar fraction given by $X_k = \frac{W}{W_k} Y_k$. Additionally, to ensure the total mass conservation eq.(1.2), a correction velocity term V_α^c – last term on the right-hand side, is introduced.

– **Energy diffusion flux (q_α) :** This flux q_α expressed as:

$$q_\alpha = -\lambda_f \frac{\partial T}{\partial x_\alpha} + \rho \sum_{k=1}^{N} h_k Y_k V_{k,\alpha} \tag{1.13}$$

where the first term accounts for the heat diffusion according to Fourier's law via thermal conductivity λ_f and temperature gradient, and the second term accounts for the diffusion of species with varying enthalpies.

Furthermore, the closure of transport properties in momentum, energy, and species equations, require defining the coefficients for dynamic viscosity μ, thermal conductivity λ_f or thermal diffusion D_T, and species diffusion D_k. In this thesis, both mixture-averaged, and simplified transport properties relying on Prandtl

(Pr) and Schmidt (Sc_k) numbers are employed. And also notably, the Soret effects and Dufour effects are neglected in this thesis.

As outlined in [83], for a simplified transport model, the coefficients for thermal conductivity (λ_f), thermal diffusion (D_T), and species diffusion (D_k) can be determined using constant Prandtl (Pr), and constant Schmidt numbers for each species k (Sc_k). They are expressed as :

$$D_T = \frac{\nu}{Pr}, \qquad D_k = \frac{\nu}{Sc_k}, \qquad \lambda_f = \frac{\mu}{Pr}\sum_{k=1}^{N} Y_k C_{p,k}. \tag{1.14}$$

Here, ν represents the kinematic viscosity, conventionally expressed as $\nu = \mu/\rho$ is also temperature-dependent eq.(1.11). Additionally, the Lewis number Le_k for each species, expressing the ratio of thermal to molecular diffusion can be defined as:

$$Le_k = \frac{Sc_k}{Pr} \tag{1.15}$$

For turbulent combustion flows, additional modeling of transport properties is necessary and will be addressed in the chapter on Large Eddy Simulation (chap:6).

- **Chemical kinetics closure :** Chemical processes are often quite complex, necessitating the modeling of numerous species and reactions. Despite this complexity, the general methodology for computing the source term ($\dot{\omega}_k$), denoting the rate of mass production or consumption for each species k, remains relatively consistent.

  The conventional approach involves the applying Arrhenius law to model ($\dot{\omega}_k$) [83]. To streamline the discussion, and also to introduce the simplified chemistry, referred to as F $\longrightarrow$ P, which is sometimes utilized in our studies, we will now present the reaction rate formulation defined for this simplified chemical scenario.

  For example, considering a simple, single-step irreversible reaction F $\longrightarrow$ P, the reaction rate per unit volume for the reactant F, denoted as $\dot{\omega_F}$ can be expressed using the Arrhenius law as:

$$\dot{\omega_F} = \rho^n Y_F A \exp\left(\frac{-E_a}{RT}\right) \tag{1.16}$$

  Here, Y_F is the dynamic mass fraction of the reactant F. And the parameters A and E_a, are the pre-exponential factor and activation energy for this reaction

respectively. These parameters are often provided within chemical schemes.

Furthermore, although the exponent $n = 1$, is used for this simplified chemistry. In most of the chemical scenarios of this thesis, an order-two global reaction with $n = 2$ indicating the partial densities of deficient and abundant reactants is considered.

Having established the foundational governing equations of reactive flows, we can now leverage these equations to delve deeper into explaining the requisite concepts essential study combustion instabilities. Notably, our focus is exclusively centered on premixed flames, as this constitutes the cornerstone of our investigation into combustion instabilities.

1.3 Premixed Flames

A homogeneous mixture of fuel and oxidizer, collectively referred to as a "reactive premix," constitutes a dynamic system that aims to reach thermodynamic equilibrium. At room temperature ($T = 300\,\mathrm{K}$), this system requires a substantial reaction time of approximately $\tau_r \approx 10 \times 10^{19}\,\mathrm{s}$ [87] to approach equilibrium, a state often referred to as 'chemically frozen'.

Equation (1.16), utilizing the Arrhenius law, establishes a relationship between the reaction rate ($\dot{\omega} = 1/\tau_r$) and the frequency of elastic collisions ($A \approx 1/\tau_c$), which reinstates the local Maxwell-Boltzmann distribution and leads to thermodynamic equilibrium. This relationship can be reformulated as:

$$\frac{1}{\tau_r} \propto \frac{1}{\tau_c} \exp\left(\frac{-E_a}{RT}\right) \text{ with } \frac{E_a}{RT} \gg 1 \tag{1.17}$$

Furthermore, the condition $\frac{E_a}{RT} \gg 1$ – a common feature of exothermic chemical processes – implies that even slight increase in temperature leads to a substantial reduction in the reaction time required to reach equilibrium. ($\tau_r \approx 10 \times 10^{-6}\,\mathrm{s}$ at $T = 2000\,\mathrm{K}$)

Therefore, by introducing a localized energy input that exceeds the activation energy E_a, a self-sustaining reaction can be effectively initiated. This input prompts molecules to react and release energy, causing a rise in gas temperature. Consequently, the adjacent fresh gases are heated through diffusion, gradually initiating the reaction in that vicinity. This gradual progression ultimately results in the formation of reaction-diffusion wave, or commonly known as premixed flame in this context, which further propagates throughout the available reactive medium.

Since, this propagation arises due to the direct coupling between the diffusion process and the reaction rate, the velocity of this reaction-diffusion wave, denoted as S_l, can be estimated using dimensional analysis as

$$S_l \propto \sqrt{D_T/\tau_r} \tag{1.18}$$

And according to kinetic theory, $D_T \approx c^2\tau_c$ [18], with c indicating the speed of sound. Consequently, from Equation (1.17), it can be shown that the Mach number of the premixed flame propagation is :

$$M = S_l/c \approx \sqrt{\exp(-E/RT)} \tag{1.19}$$

rendering it to be distinctly subsonic. A more comprehensive theoretical analysis of premixed flames can be undertaken using the Activation Energy Asymptotics (AEA) methodology [58, 112, 115].

In the forthcoming section, aided by the simplifications introduced by the Activation Energy Asymptotics (AEA) in the Navier-Stokes system, we will delve into the examination of the structure of premixed flames. This analysis will lay the groundwork for understanding the potential emergence of instabilities within these flames.

1.3.1 Asymptotic Analysis

The energy conservation equation, as shown in eq. (1.4), is originally formulated in terms of total energy (E), which is the formulation adopted in our numerical implementation. However, it can alternatively be expressed in terms of total enthalpy or temperature, both of which are equivalent representations. The detailed transformations can be found in [83]. For the sake of analytical derivations, we will utilize the temperature formulation (assuming constant C_p with temperature), a choice that offers analytical convenience while maintaining the integrity of the overall results. This formulation is expressed as:

$$\rho C_p \left(\frac{\partial T}{\partial t} + u_\alpha \frac{\partial T}{\partial x_\alpha}\right) = \dot{\omega}'_T + \frac{\partial}{\partial x_\alpha}\left(\lambda \frac{\partial T}{\partial x_\alpha}\right) - \rho \frac{\partial T}{\partial x_\alpha}\left(\sum_{k=1}^{N} C_{p,k} Y_k V_{k,\alpha}\right) \tag{1.20}$$

Here, $\dot{\omega}'_T = -\sum_{k=1}^{\mathrm{N_{SP}}} -h_k\dot{\omega}_k$ represents the heat release term only in the temperature equation.

Let us now consider one-dimensional laminar premixed flame propagating with a

laminar flame velocity S_l. When the flame is steady, placing ourselves in the reference of the flame (moving at speed S_l), the NS equations can be reduced to:

$$\rho_f S_l = \rho_b u_b = \text{constant} \tag{1.21}$$

$$\frac{\partial}{\partial x}\left(\rho\left(u+V_k\right)Y_k\right) = \dot{\omega}_k \tag{1.22}$$

$$\rho C_p u \frac{\partial T}{\partial x} = \dot{\omega}'_T + \frac{\partial}{\partial x}\left(\lambda \frac{\partial T}{\partial x}\right) - \frac{\partial T}{\partial x}\left(\rho \sum_{k=1}^{N} C_{p,k} Y_k V_k\right) \tag{1.23}$$

Equation.(1.21) describes the continuity of mass flux across the flame from fresh (x_f) to burnt (x_b).

The above equations still remains analytically challenging due to the complex chemical process involving numerous reactions and species. To address this, we can utilize the previously introduced single-step irreversible F $\longrightarrow$ P chemistry. By assuming a constant heat capacity C_p, unity Lewis number $Le = 1$ and considering only the limiting reactant F, the above system of can be reduced to:

$$\rho_f S_l \frac{\partial \theta}{\partial x} - \frac{\partial}{\partial x}\left(\frac{\lambda}{C_p}\frac{\partial \theta}{\partial x}\right) = S(\theta) \tag{1.24}$$

In this context, $\theta = (T - T_f)/(T_b - T_f) = 1 - (Y_F/Y_F^1)$ serves as the progress variable. Here, Y_F signifies the mass fraction of the reactant, and Y_F^1 represents its unburnt value. The source term $S(\theta)$, derived from eq.(1.16), is proportional to

$$S(\theta) \;\propto\; (1-\theta)\; exp\left[-\frac{\beta(1-\theta)}{1-\alpha(1-\theta)}\right] \tag{1.25}$$

In eq.(1.25), terms

$$\beta = \frac{E_a}{RT_b}\alpha \quad \text{with} \quad \alpha = 1 - \frac{T_f}{T_b} \tag{1.26}$$

Notably, as $\beta \to \infty$, indicative of a high activation energy, the source term becomes exponentially small ($\sim \mathcal{O}\left(e^{-\beta}\right)$), rendering it practically negligible across the majority of the domain. However, in a localized region where $\beta(1-\theta) \sim \mathcal{O}(1)$, the source term retains significance. In simpler terms, this source term is negligible except in a narrow region close to the burnt gas temperature, where $1 - \theta \sim \mathcal{O}(1/\beta)$. Furthermore, the source term is zero at $\theta = 0$ and $\theta = 1$. This structural behavior of the F $\longrightarrow$ P chemistry flame (Appendix B), specifically at $\beta = 8$, is illustrated in Figure 1.1.

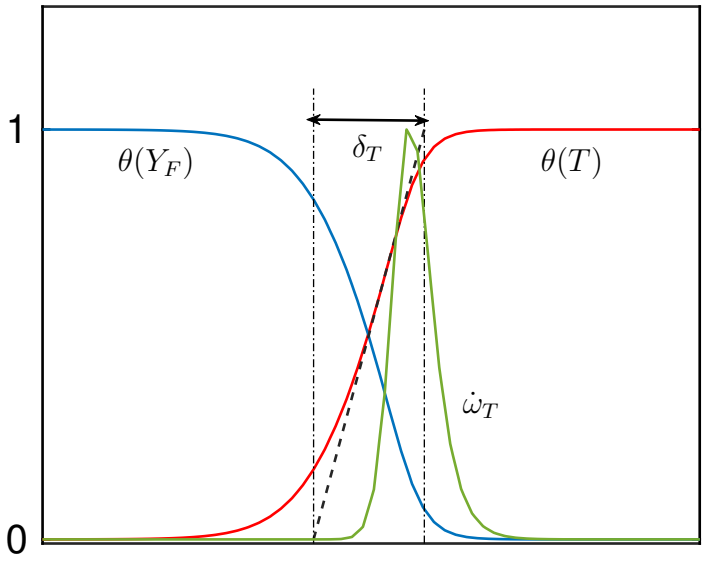

Figure 1.1: Flame structure of F $\longrightarrow$ P for $\beta = 8$: $\theta(Y_F)$ and $\theta(T)$, represent the progress variables of reactant and temperature respectively. $\dot{\omega}_T$ is the profile of the Heat Release Rate and δ_T is the thermal flame thickness.

These findings facilitate the identification of two distinct regions: (i) an outer convection-diffusion zone present on both the fresh and burnt sides, and (ii) an inner, more compact diffusive-reaction zone situated in close proximity to the burnt gases.

This behavior allows us to perceive the premixed flame as a "hydrodynamic discontinuity" that effectively separates the two convection-diffusion zones. Furthermore, owing to the subsonic characteristics of premixed flames, these regions can be approximated as incompressible regions. Consequently, the problem can be simplified to solving the incompressible flow equations for varying densities, ρ_0 and ρ_b, upstream and downstream of the flame, separated by an active interface where jump conditions need to be applied to account for the conservation laws.

1.3.2 Parameters of Interest

Before delving into the discussion of instabilities affecting the premixed flames, let us to establish the fundamental parameters employed to characterize these flames.

- **Equivalence Ratio (ϕ) :** The equivalence ratio ϕ is a crucial parameter used to characterize the composition of the reactant mixture. It is intimately related with the essential features of premixed flames, including flame speed and flame

thickness.

For instance, let's consider a reaction where ν_F moles of fuel (F) react with ν_O moles of oxidizer (O), resulting in product formation:

$$\nu_{\mathrm{F}}\,\mathrm{F} + \nu_{\mathrm{O}}\,\mathrm{O} \longrightarrow \text{Products}$$

The equivalence ratio is determined by the ratio of the actual fuel-to-oxidizer ratio to the fuel-to-oxidizer ratio at stoichiometry.

$$\phi = s\,\frac{Y_F}{Y_O} \tag{1.27}$$

Here, s, the stoichiometric ratio, represents the precise amount of oxidizer and fuel necessary for the complete consumption of both reactants:

$$s = \left(\frac{Y_O}{Y_F}\right)_{st} = \frac{\nu_O W_O}{\nu_F W_F} \tag{1.28}$$

W_O and W_F are the molecular weights of the oxidizer and fuel, and ν_O and ν_F are their stoichiometric coefficients in the balanced reaction equation.

The equivalence ratio ϕ, offers a framework for categorizing distinct flame regimes: $\phi < 1$ corresponds to lean mixtures (excess of oxidizer), $\phi > 1$ signifies rich mixtures (excess of fuel), and $\phi = 1$ indicates the stoichiometric mixture.

- **Laminar flame speed (S_l) :** It is an intrinsic feature of premixed flames, characterizing the propagation of flame into an homogeneously mixed region of unburned reactants. Numerous formulations for computing S_l exist in the literature [83], with one widely adopted approach based on the speed of consumption of reactants ($\dot{\omega}$):

$$S_l = -\frac{1}{\rho_f Y_F^f}\int_{-\infty}^{+\infty} \dot{\omega}_F dn \tag{1.29}$$

here ρ_f and Y_F^f are the density, and fuel mass fraction in the unburned reactants. And as perviously mentioned $\dot{\omega}_F$ is chemistry specific, and is expressed using partial densities of both the abundant and deficient reactants.

- **Flame thickness (δ_T & δ_D) :** The flame thickness as shown in Fig.1.1 represents the spatial extent or stiffness of the reaction region within the flame. Various

formulations for calculating flame thickness can be found in the literature [83], but the important ones are:

- Diffusive Flame Thickness (δ_D): This flame thickness is derived from scaling laws based on laminar flame speed S_l and the thermal diffusivity of the unburnt gases D_T^f:

$$\delta_D = \frac{D_T^f}{S_l} \tag{1.30}$$

- Thermal Flame Thickness (δ_T): This flame thickness is determined by calculating the maximum temperature gradient of a 1D developed flame profile Fig.1.1.

$$\delta_T = \frac{T_b - T_f}{max(|\frac{\partial T}{\partial x}|)} \tag{1.31}$$

Here, T_f and T_b corresponds to fresh and burned temperatures respectively.

- **Progress Variable ($\theta(T)$ & $\theta(Y)$) :** The progress variable is a dimensionless parameter used to quantify the progress of a chemical reaction. It is normalized between zero and one, ranging from unburnt to fully burnt gases. Typically, the progress variable can be defined based on temperature or species mass fractions. We present both definitions here:

$$\theta(T) = \frac{T - T_f}{T_b - T_f}, \tag{1.32}$$

$$\theta(Y) = \frac{Y - Y_f}{Y_b - Y_f}, \tag{1.33}$$

In these equations, Y_f and Y_b represent the mass fractions of the mixture in the unburnt and fully burnt states, respectively. The progress variable based on mass fraction can be applied using the mass fraction of any species k.

- **Heat Release Rate ($\dot{\omega_T}$) :** Abbreviated as **HRR**, this term quantifies the rate at which energy is released due to combustion per unit volume. The HRR is defined by the equation:

$$\dot{\omega}_T = -\sum_{k=1}^{N} \Delta h_{f,k}^0 \dot{\omega}_k. \tag{1.34}$$

Here $\Delta h^0_{f,k}$ is the enthalpy of formation. The heat release rate is a key parameter for evaluating the efficiency of the combustion process, and it can be utilized to calculate the thermal power as $P_{th} = \int_V \dot{\omega_T}$.

1.4 Summary

In this chapter, we introduced the fundamental governing equations of combustion. We discussed the concept of premixed flames and, utilizing the large activation energy asymptotics, demonstrated that the analysis of premixed flames can be simplified into two convection-diffusion zones where incompressible equations are applicable, separated by thin hydrodynamic discontinuity (flame) across which jump conditions can be employed. We also highlighted the essential parameters that define these flames.

With this foundational understanding we can now delve into an exploration of the instabilities that impact these flames.

Chapter 2

Premixed Flame Combustion Instabilities

Contents

2.1 Introduction 20

2.2 Hydrodynamic Instabilities 21

2.2.1 Darrieus-Landau Mechanism 21

2.2.2 Corrections to the DL Instability Model 25

2.3 Thermoacoustic Instabilities 29

2.3.1 Flame Response to Acoustic waves 29

2.3.2 Combustion Noise 32

2.3.3 Coupling and Amplification of Instability 34

2.3.4 Flame propagation in Channel 36

2.4 Summary 42

2.1 Introduction

Laminar premixed flame fronts, even when left to evolve in an open medium, are inherently predisposed to instability [18, 26]. This predisposition arises from the fact that flame propagation is always associated with gas motion and generation of pressure waves, which influence the flame shape and subsequently its dynamics. Key instabilities contributing to this phenomenon include the Darrieus-Landau hydrodynamic instability [26, 55] and thermodiffusive instabilities [97]. These instabilities induce folding and wrinkling in the flame, which can potentially lead to the transition from laminar flames to turbulence and, in extreme cases, detonation.

Furthermore, when these flames are confined or semi-confined within boundaries [1], the pressure waves they generate can couple with the acoustic modes of the system, giving rise to thermoacoustic instabilities. All these instabilities have practical implications potentially challenging the system efficiency and, in severe instances, causing irreversible damage to burners. Therefore, understanding these instability mechanisms is vital for improving the overall efficiency and safety of combustion systems.

In this chapter, we delve into the mechanisms of the Darrieus-Landau Instability and the mechanisms responsible for generation and coupling of Thermoacoustic instabilities with the system modes. We also delve briefly into the theory of combustion noise. Additionally, we employ linearized acoustics theory within reacting flows to derive the system eigenmodes of a flame propagating inside a channel. These fundamental analysis forms the basis for validating our findings in the subsequent chapters.

2.2 Hydrodynamic Instabilities

The exothermic chemical reactions occurring during combustion processes result in gas expansion. In line with the conservation laws, this phenomenon causes deviations in the stream lines, rendering the hydrodynamic discontinuity – the flame – unstable. This forms the foundation of one of the most significant intrinsic instabilities known as the Darrieus-Landau (DL) hydrodynamic instability. In the upcoming sections, without delving into rigorous mathematical analysis, we aim to provide the insights into the mechanism of this instability and its growth characteristics.

2.2.1 Darrieus-Landau Mechanism

Our exploration begins by scrutinizing the original model proposed by Darrieus [26] and Landau [55], with the goal of identifying its limitations.

The displacement speed S_d, the speed at which the interface propagates relative to the flow can be written as:

$$S_d = (u_{f,\alpha} - w_\alpha)n_\alpha = S_l \tag{2.1}$$

In this context, $u_{f,\alpha}$ is the flow upstream the flame in the laboratory frame of reference, w_α is the propagation speed of the interface in the same reference frame and n_α is the unit normal vector to the flame interface, oriented towards the burnt

[1] Thermoacoustic instabilities have been recently shown to inherently exist in anechoic chambers. [25, 35]

gases. Additionally, similar to the original DL hypothesis [26, 55], we consider that the displacement flame speed (S_d) is equal to the laminar flame speed (S_l).

Given the outcomes of the asymptotic analysis and the subsonic behavior of premixed flames, Euler equations can used to describe the incompressible and inviscid (to the first approximation) fluids on both sides of the flame , while jump conditions ensuring the conservation of mass and momentum can be applied across the flame interface.

By neglecting viscous terms and assuming incompressibility, the mass conservation equation (1.2) and the momentum conservation equation (1.3) can be adapted to derive the hydrodynamic Euler equations:

$$\begin{aligned} \frac{\partial u_\alpha}{\partial x_\alpha} &= 0 \\ \rho\left(\frac{\partial u_\beta}{\partial t} + u_\alpha \frac{\partial u_\beta}{\partial x_\alpha}\right) &= -\frac{\partial p}{\partial x_\beta} \end{aligned} \tag{2.2}$$

The jump conditions between the upstream and downstream regions of the flow can expressed as [68]:

$$\begin{aligned} [\![\rho(u_\alpha - w_\alpha)n_\alpha]\!] &= 0 \\ [\![\epsilon_{\alpha\beta\gamma} u_\alpha n_\gamma]\!] &= 0 \\ [\![p + \rho((u_\alpha - w_\alpha)n_\alpha)^2]\!] &= 0 \end{aligned} \tag{2.3}$$

Here, $[\![f]\!] = f_b - f_f$ represents the difference between variables downstream and upstream of the flame, and $\epsilon_{\alpha\beta\gamma}$ is the Levi-Civita symbol denoting the cross product between two-vectors.

By applying the system of equations described above, it is evident that due to mass conservation, the density jump across the flame, characterized by the expansion parameter $\Gamma = (\rho_f - \rho_b)/\rho_f$, causes the flow speed to increase by a factor of $\frac{1}{1-\Gamma}$ across the flame front. Additionally, the principle of momentum conservation (cross product between u_α and n_α equal to 0) dictates the continuity of tangential speed across the flame front, leading to an increase in speed exclusively along the normal component to the interface. Assuming the reference of flame, these effects can be expressed using the jump conditions as follows:

$$\begin{aligned} [\![u_\alpha n_\alpha]\!] &= \left(\frac{1}{1-\Gamma} - 1\right) S_l \\ [\![\epsilon_{\alpha\beta\gamma} u_\alpha n_\gamma]\!] &= 0 \\ [\![p]\!] &= -\left(\frac{1}{1-\Gamma} - 1\right) \rho_f S_l^2 \end{aligned} \tag{2.4}$$

Consequently, when considering a streamline inclined at an angle to the interface, as observed in the case of slanted flames such as premixed conical flames. In order to conserve the tangential speed, the streamline undergoes a deflection towards the normal direction upon crossing the front. For instance, the deviation of streamlines towards the normal as they cross the flame front in case of premixed conical flames are shown in fig.2.1.

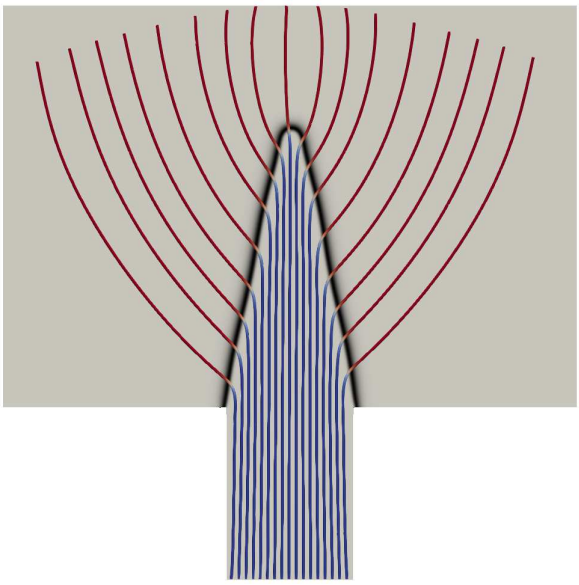

Figure 2.1: Illustration of the streamlines deviating towards the normal in case of a conical premixed flame for F $\longrightarrow$ P chemistry. The streamlines are coloured as function of temperature.

Therefore, for a planar front perturbed by a wavelength $\lambda = 2\pi/k$, where k denotes the wavenumber of the wrinkling, the curvature of the flame front (concave or convex) leads to the convergence or divergence of streamlines, resulting in local variations in flow speed. This, in turn, causes local deceleration or acceleration of the flame front. These local variations give rise to further distortions in the streamlines, ultimately leading to the unconditional amplification of the flame perturbation. These phenomena are vividly demonstrated in Figure 2.2 for a perturbed flame front. In Figure 2.2a, the initial

stages are depicted, illustrating the perturbed flame front and the converging/diverging streamlines. Figure 2.2b, on the other hand, shows the flame front and the streamlines after the DL instability has sufficiently grown.

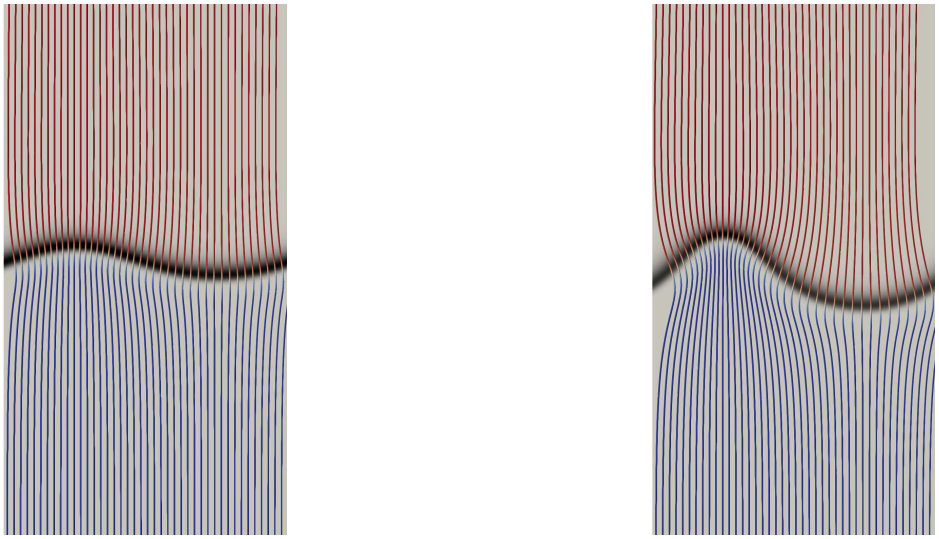

(a) Initial stages of DL instability (b) DL instability after sufficient growth

Figure 2.2: Illustration of growth of Darrieus-Landau Instability. Streamlines colored by temperature can be seen converging/diverging towards concave/convex curvatures (as seen from the side of fresh gases - blue), leading to an increase/decrease in the flow speed giving rise to further amplification of the disturbance.

And hence, Darrieus [26] and Landau [55] postulated that any slightest perturbation within the flow or flame front would inevitably trigger a hydrodynamic instability, with its growth rate (σ) intrinsically determined by the expansion parameter Γ and laminar flame speed S_l. Following this line of reasoning, a linear perturbation analysis was performed on the perturbed flame front position $\phi(x,t)$ using Fourier modes – $\hat{\phi}\,\exp(ikx+\sigma t)$, yielding a quadratic equation that describes the evolution of the flame front and determines the growth rate σ [38, 68, 79, 80]: .

$$\begin{aligned}(2-\Gamma)\frac{\partial^2\widehat{\phi}}{\partial t^2}+2kS_l\frac{\partial\widehat{\phi}}{\partial t}-\frac{\Gamma}{1-\Gamma}S_l^2k^2\widehat{\phi}=0\\ \Leftrightarrow(2-\Gamma)\sigma^2+2kS_l\sigma-\frac{\Gamma}{1-\Gamma}S_l^2k^2=0\end{aligned}\tag{2.5}$$

For $0\leq\Gamma<1$, which is always the case due to the exothermic nature of the reaction, the growth rate σ possesses two real roots, one of which is always positive and takes the form:

$$\sigma = \frac{\sqrt{\Gamma + 1/(1-\Gamma)} - 1}{2 - \Gamma} S_l k \tag{2.6}$$

From the above dispersion relation, it is evident that planar flames are unconditionally unstable, with disturbances of all wavelengths undergoing amplification. Furthermore, the amplification rate escalates as Γ increases, and the growth rate which is seen to have a linear dependency on wavenumbers k intensifies with larger values of k, indicating that shorter waves undergo more rapid growth compared to longer waves. These are the precise relationships originally formulated by Darrieus [26] and Landau [55].

However the conclusions drawn from the Darrieus-Landau (DL) analysis, particularly the proposition that shorter waves (λ) exhibit more rapid growth compared to longer waves, seem to contradict experimental observations. And also the proposal that the flames were unconditionally unstable was also in contradiction to the observations. These discrepancies spurred researchers to consider the impact of internal flame structures, prompting a deeper exploration of the phenomenon.

2.2.2 Corrections to the DL Instability Model

In contrast to original DL model that assumes $S_d = S_l$, Markstein [66] took an alternative approach while still treating the flame as a discontinuity. He introduced the notion that the flame speed might depend on the local curvature of the flame front. Additionally, Pelce and Clavin [80], Matalon and Matkowsky [68], Clavin and Garcia [19], and Frankel and Sivashinsky [38], through comprehensive multi-scale analysis using asymptotic analysis, extended this concept further to incorporate diffusion effects, mixture properties, and strain rates in conjunction with considerations of curvature effects.

In this broader framework, the displacement speed is expressed as [68]:

$$S_d = S_l - \mathcal{L}\kappa \tag{2.7}$$

where κ is the flame stretch rate which includes both, the effect of the flame curvature and hydrodynamic strain experienced by the flame. And $\mathcal{L}$, the Markstein length, is defined in terms of Markstein Number $\mathcal{M} = \mathcal{L}/\delta_D$, where Markstein Number $\mathcal{M}$ is the measure of the sensitivity of the local flame velocity to the curvature and stretch.

For a simplified flame model involving a one-step chemical reaction (e.g., F $\longrightarrow$ P), asymptotic expansion can be employed as $\beta >> 1$. Considering a constant Prandtl number, the resulting expression for the Markstein number is given by [94]:

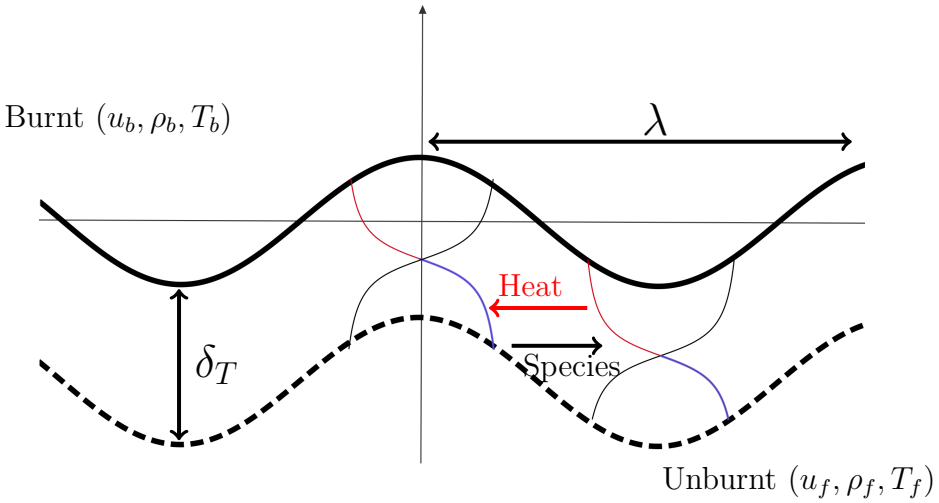

Figure 2.3: Influence of Interface Curvature: Depending on Lewis number(Le), wavelengths $\lambda \sim \mathcal{O}(\delta_T)$ can be stabilized.

$$\mathcal{M} = \frac{J}{\Gamma} - \frac{1}{2}\beta(Le-1)\int_0^1 \frac{h(\theta)\ln(\theta)\mathrm{d}\theta}{1+\theta\Gamma/(1-\Gamma)} \tag{2.8}$$

In this context, θ represents the progress variable/ normalized temperature eq.(1.32). The term $h(\theta)$ signifies the ratio of thermal diffusivity (D_T) multiplied by the density at temperature θ to its value in the unburned gases. Meanwhile, h_b corresponds to the value of $h(\theta)$ in the burned gases. Additionally, the integral J can be defined as:

$$J = \frac{\Gamma}{1-\Gamma}\int_0^1 \frac{h(\theta)}{1+\theta\Gamma/(1-\Gamma)}\mathrm{d}\theta, \tag{2.9}$$

As evident from Equation (2.8), the sign of the Markstein number $\mathcal{M}$ depends on the value of the Lewis number (Le). Specifically, $\mathcal{M}$ can be either positive or negative, where $\mathcal{M} > 0$ indicates stabilization due to diffusion at large wavenumbers, while $\mathcal{M} < 0$ implies no stabilization.

This effect of Le number is demonstrated in Figure 2.3. Due to the curvature of the flame front, the internal flame structure experiences traverse flux of temperature and species. A fluid particle situated in a convex area of the front (observed from the perspective of cooler gases) will possess a higher temperature compared to its neighbor in the concave region. This facilitates the transfer of heat from convex regions to concave ones, thereby generating a stabilizing effect. Notably, this influence becomes particularly pronounced on scales closely aligned with the flame thickness ($\lambda \sim \mathcal{O}(\delta_T)$).

In contrast, diffusive fluxes of species act in the opposite direction. These fluxes drain reactants from concave front regions and enrich convex areas. Consequently, the

propagation speed experiences further augmentation, thereby contributing to destabilization. The equilibrium between these opposing effects hinges on the ratio of thermal diffusion, to mass diffusion coefficients of the reactants – quantified by the Lewis number (Le).

Additionally, it was also observed that acceleration effects, such as gravity, also exerted some stabilizing influence, primarily at smaller wavenumbers [80].

Incorporating these corrections, the evolution equation for the flame front $\phi(x,t)$ in Fourier modes and the dispersion relation for the growth rate σ can now be expressed as follows:

$$\begin{aligned} &A(k)\frac{\partial^2\widehat{\phi}}{\partial t^2} + B(k)\frac{\partial\widehat{\phi}}{\partial t} + C(k)\widehat{\phi} = 0 \\ \Leftrightarrow\ &A(k)\sigma^2 + B(k)\sigma + C(k) = 0 \end{aligned} \tag{2.10}$$

where the co-coefficients $A(k)$, $B(k)$ and $C(k)$ are expressed as:

$$\begin{aligned} A(k) =&(2-\Gamma) + \Gamma k\delta_D(\mathcal{M} - J/\Gamma) \\ B(k) =&2S_l k\left(1 + \frac{1}{1-\Gamma}k\delta_D(\mathcal{M}-J)\right) \\ C(k) =&\frac{\Gamma}{1-\Gamma}S_l^2 k\left(\frac{1}{2}k_g - k\left(\delta - \frac{k}{k_c}\right)\right) \end{aligned} \tag{2.11}$$

This system exhibits the characteristics of a damped harmonic oscillator. In contrast to the original Darrieus-Landau hypothesis, the flame is no longer unconditionally unstable. Stability prevails for wavenumbers $k < k_g$ due to the influence of acceleration effects such as gravity, and for wavenumbers $k > k_c$ due to the impact of diffusive effects. Additionally, the terms k_g, k_c, and δ in Equation (2.11) are defined as follows:

$$\begin{aligned} k_g &= 2(1-\Gamma)\frac{g}{S_l^2} \\ \delta &= 1 + \frac{g\delta_D}{S_l^2}(1-\Gamma)\left(\mathcal{M} - \frac{J}{\Gamma}\right) \\ k_c &= \frac{1}{\delta_D}\left(h_\mathrm{b} + (2+\Gamma)\frac{Ma}{\Gamma} - \frac{2J}{\Gamma}\right. \\ &\qquad \left. +(2Pr-1)\int_0^1 (h_\mathrm{b} - h(\theta))\,\mathrm{d}\theta\right)^{-1} \end{aligned} \tag{2.12}$$

Given the omission of gravity ($g = 0$) in our investigations, the parameter k_g remains zero. Consequently, all large wavelengths are inherently unstable. Additionally,

the parameter k_c, which establishes the cut-off wavenumber for larger values of k as discussed earlier, is contingent upon the Markstein Number $\mathcal{M}$. This Markstein Number is, in turn, a function of the Lewis Number (Le). Notably, for the majority of hydrocarbon fuels, $Le \geq 1$, while instances of $Le < 1$ are infrequent and limited to specific cases such as lean hydrogen and highly rich hydrocarbons. Hence the diffusive influences generally attribute to the stabilizing effects.

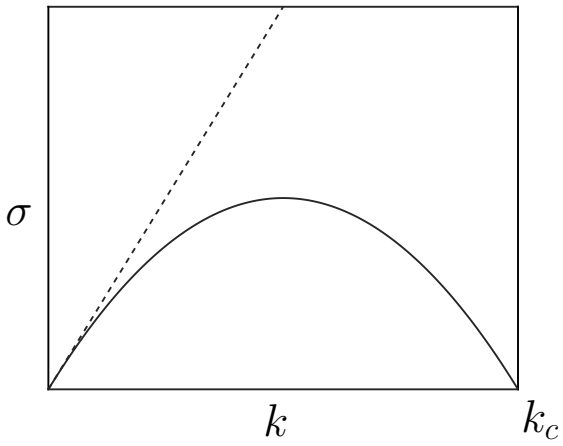

Figure 2.4: Theoretical Darrieus Landau growth rate σ predicted by the original Darrieus Landau Model (dash) and with the correction terms (solid) for different wavenumber k. Disturbances of wavenumber $k > k_c$ are stable.

As for the growth rate σ, it no longer maintains a linear relationship with wavenumbers k. Instead, it varies as a function of $(k - k^2/k_c)$. A comparative illustration of these two growth rates is presented in Figure 2.4. Notably, the plot indicates that while the growth rate σ conforms to linearity in the original DL hypothesis, the incorporation of correction terms manifests a gradual damping of growth at larger wavenumbers. Furthermore, beyond the cut-off wavenumber k_c, the flame front tends to approach a stable planar solution.

In conclusion, the linear modifications applied to the original Darrieus-Landau (DL) hypothesis ($S_d = S_l$) offer a more precise depiction of the DL instability's behavior across various wavenumbers. However, these modifications still do not fully account for all the experimental observations linked to unstable Darrieus-Landau flames. Experimental findings indicate that following a brief phase of exponential growth, due to the non-linear process the front's amplitude reaches saturation. In large domains, this nonlinear evolution of flame fronts leads to the merging and formation of new crests (concave regions) on the flame fronts.

But as our focus lies in studying instabilities within "narrow channels," where these nonlinear effects have minimal impact, we won't delve further into them here. A comprehensive understanding of these nonlinear phenomena can be found in the works of [96, 97].

With an understanding of the characteristics of this hydrodynamic instability, we can now proceed to explore another type of combustion instability known as Thermoacoustic Instabilities. In these instabilities, the Darrieus-Landau instability once again plays a substantial role in amplifying thermoacoustic instabilities.

2.3 Thermoacoustic Instabilities

The thermoacoustic instability primarily[2] arises due to the coupled interactions between the acoustic waves and the unsteady heat release of the flames. And unlike traditional instabilities, these instabilities are influenced, not only by the local flame and flow field properties but also by the broader confinement characteristics intrinsic to the combustion system.

At its essence, this instability is characterized by a feedback loop, where acoustic waves impact flame behavior, and flames reciprocate by generating acoustics. This interplay is further modulated by the confinement attributes specific to the combustion environment. To comprehensively explore this intricate phenomenon, we break down the study into three essential sub-sections, each delving into a critical aspect of the thermoacoustic instability, providing a holistic understanding of its underlying mechanisms.

2.3.1 Flame Response to Acoustic waves

Within the context of this feedback mechanism, the influence of acoustic waves on the flame front has been a subject of intense research since the pioneering experimental work by Mallard and Le Chatelier in 1883 [63]. Over the years, several mechanisms describing the coupling of acoustic fields with flames have been proposed [33, 51, 67, 89].

Among these mechanisms, two have emerged as particularly significant:

- **Pressure Coupling:** This mechanism involves the modification of the internal flame structure due to the modulation of the flame's reaction rate caused by adiabatic temperature fluctuations induced by pressure pertubations – acoustic waves [33]. However, it has been demonstrated by Clavin et al. [20] that the

[2]The influences of entropy fluctuations and coherent flow structures may sometimes be significant.

strength of this coupling is relatively weak and can only account for acoustic instabilities in certain cases.

- **Velocity Coupling:** In contrast, the velocity coupling mechanism, often referred to as "velocity-induced flame response" [67, 89], is significantly stronger. It involves the modulation of the total heat release rate resulting from the modulation of the total flame surface area, driven by accelerations associated with the acoustic velocity field. The density difference between hot burnt gases and cold unburnt gases renders the shape of a curved flame front sensitive to the presence of such an acceleration.

Flame response to Different Acoustic wave Intensities:

The characteristics of the "velocity-induced flame response," which are closely tied to curved flame shapes, can be further elucidated by leveraging the evolution equation of the flame fronts subjected to Darrieus-Landau (DL) instability (eq. (2.10))—a principal factor contributing to amplification of the flame curvature.

Originally proposed by Markstein [67] and refined by Searby and Rochwerger [94], the equation (2.10) can be extended by considering the periodic displacement of the flame front $\phi(x,t)$ by a planar sound wave:

$$A(k)\frac{\partial^2\widehat{\phi}}{\partial t^2} + B(k)\frac{\partial\widehat{\phi}}{\partial t} + \left(C - C_1\cos(\omega_a t)\right)(k)\widehat{\phi} = 0 \tag{2.13}$$

with

$$C_1(k) = \Gamma k\omega_a u_a\left(1 - k\delta_D\left(\mathcal{M} - \frac{J}{\Gamma}\right)\right) \tag{2.14}$$

In this context, ω_a and u_a represent the acoustic frequency and amplitude of the planar sound wave, respectively.

This equation (2.13), now taking the form of a parametric oscillator with damping, can be further reduced to a solvable Mathieu equation [72] through a clever change of variables [94]. Solving this Mathieu equation, typically with the assistance of computational tools like Mathematica, provides valuable insights into the regions of thermoacoustic instability as originally recognized by Markstein [67].

Disregarding gravity, the regions of instability, for a given unique Markstein number $\mathcal{M}$ and acoustic frequency ω_a, depend on both the amplitude of the acoustic wave and the wavenumber of the curved flame front. Figure 2.5 provides an illustration of these typical instability regions:

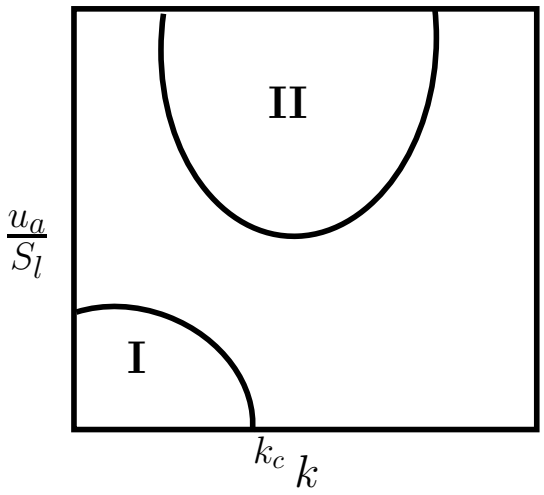

Figure 2.5: Illustration of a typical thermoacoustic instability diagram for a specific Markstein number $\mathcal{M}$ and acoustic frequency ω_a. k denotes the wavenumber of the wrinkled flame front and u_a denotes the amplitude of the acoustic wave. **I** denotes the primary thermoacoustic instability region and **II** denotes the secondary instability region. The rest is the region where the flame is planar due to acoustic stabilization. k_c at zero acoustic amplitude is the cut-off wavenumber after which the flame is stabilized due to diffusion.

- In the absence of acoustic waves ($u_a = 0$), the flame front evolves according to the modified DL hypothesis (eq. (2.10)) with a diffusive-stabilized cut-off wavenumber k_c
- In the limit of small amplitude acoustics ($u_a/S_l \ll 5$), a "primary instability" region is observed. In this region, the DL instability experiences slight damping, and the structures on the flame oscillate at the acoustic frequency.
- For high amplitude acoustics ($u_a/S_l \gg 7$), cells form on the flame front, and these cells oscillate at half the frequency of the excitation. This type of instability is often referred to as "secondary instability" and can be triggered only by pre-existing finite-amplitude acoustic oscillations.
- Finally, between the secondary and primary instability regions, there is a region where the curved DL flames are re-stabilized to a planar flame.

In Chapter 4, we will revisit these instability regions in the context of externally excited acoustic waves and freely propagating flames within a channel. It's worth noting that these instability regions, including the stable region under moderate forcing and the secondary region featuring cellular flames, have also been observed in a forced conical flame by Durox et al. [34] and Baillot et al. [4] respectively.

Flame Response to Different Acoustic Wave Frequencies:

The influence of acoustic wave amplitude on flame fronts is noticeable only at specific frequencies, typically on the order of the flame transit time $\tau_f = D_T/S_l^2$. In other words, these effects become prominent when the time period of acoustic waves τ_a is greater than or of the same order of magnitude as τ_f (i.e., $\tau_a \sim \mathcal{O}(\tau_f)$).

Additionally, in Figure 2.6, we present snapshots of a conical flame front exposed to varying frequencies of acoustic forcing:

- In Figure 2.6a, the flame shape (total heat release rate) experiences significant modulation when subjected to low-frequency acoustic waves, approximately $\tau_a \sim \mathcal{O}(10 \cdot \tau_f)$. This modulation is so pronounced that it leads to the separation of huge pockets of fresh gases by "pinch off."
- Figure 2.6b illustrates the flame shape (total heat release rate) undergoing modulation at moderate frequencies, around $\tau_a \sim \mathcal{O}(\tau_f)$. This modulation can also sometimes lead to the creation of small fresh gas pockets by pinch off. Various instability regions shown in Figure 2.5 can be observed in this range.
- Figure 2.6c shows the flame exposed to high frequencies, with $\tau_a \sim \mathcal{O}(10^{-1} \cdot \tau_f)$. In this range, the flame remains unaffected by acoustic modulations and does not exhibit significant heat release fluctuations.

This flame behavior is akin to a "low-pass filter, " and the study of how the flame responds to various forcing frequencies is typically quantified using a concept known as Flame Transfer Function (FTF). While we won't extensively explore this in our thesis, it is worth noting that this phenomenon is crucial for the coupling and amplification of the thermoacoustic instability.

2.3.2 Combustion Noise

Now that we have examined how flames respond to acoustic waves, let us explore the process by which flames themselves generate acoustic waves. This phenomenon, often referred to as "Combustion Noise," not only contributes to the amplification of thermoacoustic instability but also may lead to noise pollution.

Combustion noise can be primarily traced back to two main sources: "Indirect Noise," which typically arises from the coupling of convective entropy modes and the mean flow velocity, and "Direct Noise," which results from the non-steady process of volumetric expansion within the reactive region. The importance of these sources

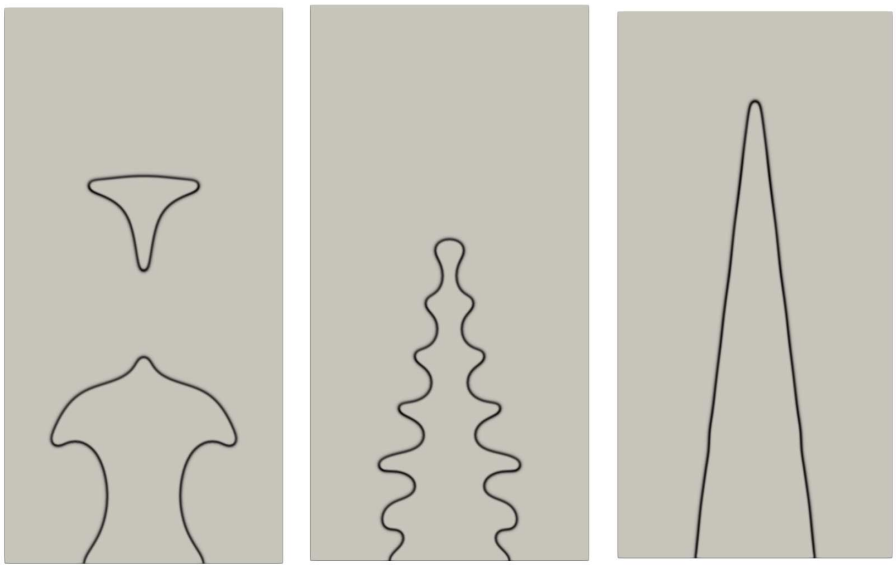

(a) $\tau_a = 14\tau_f$ (b) $\tau_a = 3.59\tau_f$ (c) $\tau_a = 0.37\tau_f$

Figure 2.6: Visualization depicting the response of a conical flame when exposed to acoustic forcing of different frequencies. The flame characteristic time $\tau_f = \frac{D_T}{S_l^2} = 4.73 \times 10^{-5}\,\text{s}$, and the amplitude of the forcing, denoted as u_a, is set at 25% of the injection velocity u_1

depends on the specific context. While the first source is particularly significant in high-performance propulsion systems connected to turbines or nozzles, the second source – direct noise is a result of noise generation directly by the flame region itself. Our work will concentrate solely on this second source.

Combustion Noise Theory:

The generation of acoustic waves by the flame can be intuitively understood by examining mass conservation across premixed flames:

$$\rho_f u_f = \rho_b u_b \tag{2.15}$$

The heat released by the flame induces gas expansion, resulting in a reduction in gas density ($\rho_b < \rho_f$). To ensure mass conservation across the flame, this change in density leads to an increase in velocity or volume flux ($u_b > u_f$). Consequently, any fluctuations in the flame heat release cause corresponding variations in the volume flux, thereby leading to the generation of sound.

This phenomenon can be rigorously derived through linearization of the Navier-Stokes system, as outlined in [13], yielding an inhomogeneous wave equation:

$$\frac{\partial}{\partial x_\alpha}\left({c_0}^2\frac{\partial p_1}{\partial x_\alpha}\right)-\frac{\partial^2 p_1}{\partial t^2}=-\frac{\partial}{\partial t}\left((\gamma-1)\dot{\omega}_{T_1}\right)-\gamma p_0\frac{\partial u_\beta}{\partial x_\alpha}\frac{\partial u_\alpha}{\partial x_\beta}-\frac{\gamma p_0}{W_0}\frac{\partial^2 W'}{\partial t^2} \tag{2.16}$$

In this equation, γ represents the ratio of specific heats, $c_0=\sqrt{\gamma\frac{R}{W}T_0}$ denotes the sound speed, and x_1 quantities denote fluctuations, while quantities x_0 indicate mean values that may vary with spatial coordinates.

For our research focus, which primarily deals with low-speed reacting flows, we can simplify the wave equation, eq.(2.16), further. Specifically, we can neglect the second term on the right-hand side (RHS), which accounts for aerodynamic sound sources in turbulent flows. Additionally, since our thesis work not cover oxy-fuel combustion, we can omit the third term, which relates to sound sources arising from changes in mean molar composition. As a result, only the first term remains, characterizing sound generation (p_1) due to perturbations in heat release rate ($\dot{\omega}_{T_1}$).

Furthermore, for the unconfined flames, at any measurement location $\boldsymbol{r}=\sqrt{x^2+y^2+z^2}$ in the far-field, the radiated pressure fluctuations $p_1(\boldsymbol{r},t)$ due to an unsteady heat release noise source at $\boldsymbol{r_0}$ can be obtained. This is achieved by replacing the non-local sound speed c_0 with a constant sound speed c_s in Equation (2.16) and utilizing Green's function for the 3D wave equation [75].

$$p_1(\boldsymbol{r},t)=\frac{\gamma-1}{4\pi c_s^2}\int_V\frac{1}{|\boldsymbol{r}-\boldsymbol{r_0}|}\frac{\partial}{\partial t}\dot{\omega}_{T_1}\left(\boldsymbol{r}_0,t-\frac{|\boldsymbol{r}-\boldsymbol{r_0}|}{c_s}\right)dV\left(\boldsymbol{r}_0\right) \tag{2.17}$$

This expression for the far-field pressure fluctuation highlights one of the most significant characteristics of noise generation in reactive flows: noise generated by unsteady heat release is inherently monopolar in nature, implying that combustion noise is radiated isotropically.

Lastly, the intensity of the fluctuations of the heat release rate ($\dot{\omega_T}$), and consequently the generated sound, depends on various factors. These include the Lewis number (Le), Zel'dovich number (β), among others. The effects of these parameters on the sound generation will be examined in detail in chapter 5.

2.3.3 Coupling and Amplification of Instability

In the preceding sections, we delved into the impact of acoustic waves on flames and the generation of acoustic waves by flames. Now, we will explore the concepts of the coupling of these two phenomena and the effects of confinement, which may lead to the amplification of thermoacoustic instability.

Under normal operating conditions, combustion noise sources tend to be incoherent, radiating a broad range of frequencies. However, during thermoacoustic instability, often induced by confinement, a feedback loop forms between the noise sources and pressure perturbations. This causes the noise radiation to become more coherent and align with specific frequencies, typically the acoustic eigenmodes of the system. This coherent noise then induces cyclic perturbations in the flow-flame system.

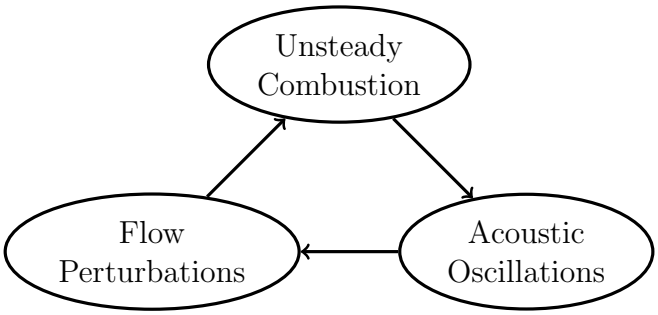

Figure 2.7: Illustration of the feedback process responsible for combustion instability [57]

Figure.2.7 illustrates the mechanism of a self-sustained thermoacoustic instability. It consists of following sequence of events:

1. The unsteady combustion generates acoustic oscillations.
2. These oscillations interact with the boundaries of the confinement and generate flow perturbations, including fluctuations of velocity and other thermodynamic-state variables.
3. These flow perturbations modify the heat release rate, resulting in unsteady combustion, thus closing the loop.

The amplification of the instability of this closed feedback loop depends on changes in the acoustic energy within the system.

The Acoustic Energy (AE) balance within this system can be derived once more using the linearized, non-viscous Navier-Stokes system, as detailed in [83]. It is expressed as:

$$\frac{\partial}{\partial t}\underbrace{\left[\frac{\rho_0 u_{\alpha,1}^2}{2}+\frac{p_1}{2\rho_0 c_0^2}\right]}_{e_1}+\frac{\partial}{\partial x_\alpha}\underbrace{[p_1 u_{\alpha,1}]}_{f_1}=\underbrace{\frac{(\gamma-1)}{\gamma p_0}p_1\dot{\omega}_{T_1}}_{r_1} \tag{2.18}$$

In this equation, e_1 represents the acoustic energy within the system, while f_1 stands for the flux either entering or exiting the system. On the other hand, r_1 signifies the combustion source term. Depending on the correlation between the pressure fluctuations (p_1) and heat release rate fluctuations ($\dot{\omega_{T_1}}$), r_1 can either act as a sink or a source. It is worth noting that to obtain a meaningful result, equation.(2.18) must be integrated over both space and time.

$$\underbrace{\frac{(\gamma-1)}{\gamma p_0}\int_V\int_0^{\tau_{avg}} p_1\dot{\omega_{T_1}}dtdV}_{\mathcal{R}_1} \quad > \quad \underbrace{\int_A\int_0^{\tau_{avg}} p_1 u_{\alpha,1}dtdA}_{\mathcal{F}_1} \tag{2.19}$$

In this context, the variables V and A denote the volume and surface area of the domain, respectively, while τ_{avg} represents the averaging time, typically a multiple of the oscillation periods associated with system eigenmodes. Equation (2.19), often referred to as the "Rayleigh Criterion," illustrates the conditions under which thermoacoustic instability amplifies or diminishes. When $\mathcal{R}1 > 0$, signifying that pressure fluctuations p_1 and heat release rate fluctuations $\dot{\omega_{T_1}}$ are in phase, the term $\mathcal{R}_1$ operates as a source, enhancing the acoustic energy. If this enhancement surpasses the damping effects caused by the flux $\mathcal{F}_1$, local amplification of the instability occurs. Conversely, when $\mathcal{R}_1 < 0$, indicating that p_1 and $\dot{\omega_{T_1}}$ are out of phase, $\mathcal{R}_1$ acts as a sink, depleting the acoustic energy and thereby attenuating the instability. In recent years, a new criterion for assessing the development of thermoacoustic instability, known as "Chu's criterion," has been introduced [77]. This criterion, relies on fluctuating energy (FE) proposed by Chu [17] and considers the impact of entropy fluctuations as well.

2.3.4 Flame propagation in Channel

In this subsection, our aim is to meticulously derive a typical example of system modes, specifically focusing on the eigenmodes associated with flame propagation within an open-closed channel. To achieve this, we will introduce essential concepts from acoustics and pertinent mathematical tools as prerequisites.

Background

We will begin with the linearized, non-viscous version of the Navier-Stokes system in a quiescent flow ($u_0 = 0$), expressed as:

$$\frac{\partial \rho_1}{\partial t} + \rho_0 \frac{\partial u_{\alpha,1}}{\partial x_\alpha} = 0 \tag{2.20}$$

$$\rho_0 \frac{\partial u_{\alpha,1}}{\partial t} + \frac{\partial p_1}{\partial x_\alpha} = 0 \tag{2.21}$$

$$\frac{1}{c_0^2}\frac{\partial p_1}{\partial t} + \rho_0 \frac{\partial u_{\alpha,1}}{\partial x_\alpha} = \frac{\gamma - 1}{c_0^2}\dot{\omega_{T_1}} \tag{2.22}$$

Here, $c_0 = \sqrt{\frac{\gamma p_0}{\rho_0}}$ denotes the speed of wave propagation. Equations (2.20), (2.21), and (2.22) represent the linearized: continuity, momentum conservation, and energy conservation, respectively. Additionally, assumptions of constant molecular weight and heat capacities are made to simplify the analysis.

By performing some straightforward manipulations of Eqs. (2.21) and (2.22), we can obtain the inhomogeneous acoustic wave equation, (similar to eq. (2.16)):

$$\frac{\partial^2 p_1}{\partial t^2} - c_0^2 \frac{\partial^2 p_1}{\partial x_\alpha^2} = \frac{\gamma - 1}{c_0^2}\frac{\partial \dot{\omega_{T_1}}}{\partial t} \tag{2.23}$$

Premixed flames:

In the context of a premixed flame with a flame thickness (δ_T) significantly smaller than the acoustic scales (λ), we can simplify the problem by partitioning it into distinct regions: one comprising fresh gases, another comprising burnt gases, and a thin discontinuity region representing the flame. Across this discontinuity, acoustic waves obey specific jump conditions, and thus enabling us to employ solutions to the homogeneous wave equation.outside this region. By considering plane waves, this solution is expressed as follows:

$$p_1(x,t) = A^+(t - x/c_0) + A^-(t + x/c_0) \tag{2.24}$$

Here, A^+ represents the amplitude of the wave propagating in the positive x direction, while A^- represents the amplitude of the wave propagating in the negative x direction. Additionally, we can also derive the solution in terms of velocity fluctuations u_1, which is expressed as:

$$u_1(x,t) = \frac{1}{\rho_0 c_0}\left(A^+(t - x/c_0) - A^-(t + x/c_0)\right) \tag{2.25}$$

where $\rho_0 c_0$ represents the impedance of the medium for the propagation of acoustic waves, given by $p_1/u_1 = \rho_0 c_0$ for the wave traveling in the positive x direction and $p_1/u_1 = -\rho_0 c_0$, for the wave in the negative x direction.

The jump conditions across the flame can be derived by integrating the linearized momentum equation (eq.(2.21)) and the linearized energy equation (eq.(2.22)) over a volume (V) and taking the limit as Δx approaches zero to account for the discontinuity. The linearized momentum equation yields:

$$[p_1]_f = [p_1]_b \tag{2.26}$$

In this equation, $[p_1]_f$ and $[p_1]_b$ represent the acoustic pressures in the fresh and burnt gases adjacent to the discontinuity, respectively. Equation (2.26) demonstrates that acoustic pressure remains continuous across the compact heat release zone.

Similarly, integrating the linearized energy equation we obtain:

$$S_f[u_1]_f - S_b[u_1]_b = \frac{\gamma - 1}{\rho_f c_f^2}\dot{Q}_1 \tag{2.27}$$

In this context, S_f and S_b represent the cross-sectional areas of the tube/channel before and after the flame, respectively. $[u_1]_f$ and $[u_1]_b$ denote the acoustic velocities in the fresh and burnt gases adjacent to the discontinuity. Additionally, $\dot{Q}_1 = \int_V \dot{\omega_{T_1}}$ represents the total unsteady heat release produced by the flame.

Equation (2.27) reveals that there is a discontinuity in acoustic velocity across the compact heat release zone, illustrating the jump in velocity due to the presence of the flame. Furthermore, it also demonstrates the induced dilation caused by the heat release process.

Crocco's Model:

Lastly, we introduce Crocco's model as a simple Flame Transfer Function (FTF) model to characterize unsteady heat release in terms of velocity fluctuations. This model can be expressed as:

$$\frac{\gamma - 1}{\rho_f c_f^2}\dot{Q}_1 = S_f n u_1(x_f, t - \tau_d) \tag{2.28}$$

In this equation, n represents a non-dimensional constant known as the interaction index (representing the gain), and τ_d denotes the time delay between the total unsteady heat release $\dot{Q}_1$ and the velocity fluctuations u_1 at flame position x_f. Consequently, it is often referred to as the sensitive time-lag model.

Harmonic waves:

To further simplify the analysis, we can decouple the temporal and spatial variations

by considering harmonic waves and utilizing complex analysis:

$$p_1(x,t) = \mathrm{Re}\{p_w(x)e^{i\omega t}\}, \quad u_1(x,t) = \mathrm{Re}\{u_w(x)e^{i\omega t}\} \quad \dot{Q}_1 = Q_1 e^{i\omega t} \tag{2.29}$$

with angular frequency $\omega = kc_0$ and $p_w(x)$ and $u_w(x)$ are the complex functions of space, expressed by:

$$p_w(x) = A^+ e^{-ikx} + A^- e^{ikx} \tag{2.30}$$

$$u_w(x) = \frac{1}{\rho_0 c_0}(A^+ e^{-ikx} - A^- e^{ikx}) \tag{2.31}$$

Eigen modes:

With this brief background of the elementary acoustic equations, let us now derive the Eigen modes of the channel with a flame in it. Figure 2.8 illustrates the flame confined within the open-closed channel. This channel is open to the exhaust of burnt gases at one end ($x = L$), where $p_1 = 0$, and closed at the other end ($x = 0$) with $u = 0$. The red line, perpendicular to the channel axis at $x = x_f$, represents the flame. Notably, the flame thickness (δ_T) is significantly smaller than both the wavelength (λ) and thereby the channel length (L). Consequently, we can treat it as a discontinuity, across which acoustic waves obey jump conditions. Note that alongside to the consideration of plane waves, we consider 1D system to perform this analysis.

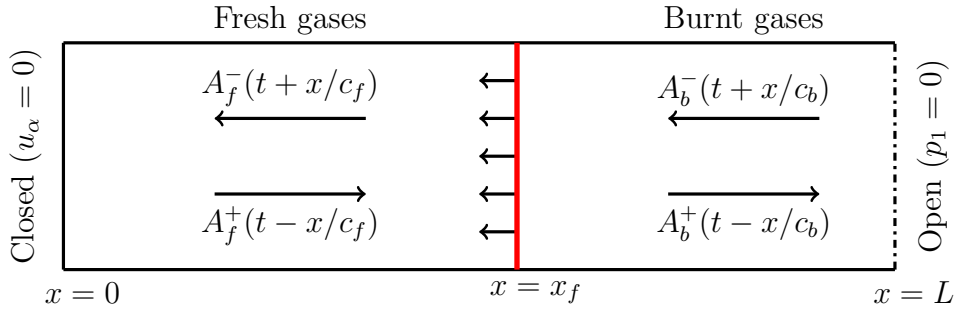

Figure 2.8: Illustration of flame inside an open-closed channel: A_f^- and A_b^- are the left traveling waves, and A_f^+ and A_b^+ are the right traveling waves. Red line at $x = x_f$ denotes the flame which moves from left to right.

Solution to the wave equations in fresh and burnt gases:

In fresh gases:

$$p_1^f(x,t) = A_f^+ e^{-ik_f(x-x_f)+i\omega t} + A_f^- e^{ik_f(x-x_f)+i\omega t} \tag{2.32}$$

$$u_1^f(x,t) = \frac{A_f^+}{\rho_f c_f} e^{-ik_f(x-x_f)+i\omega t} - \frac{A_f^-}{\rho_f c_f} e^{ik_f(x-x_f)+i\omega t} \tag{2.33}$$

In burnt gases:

$$p_1^b(x,t) = A_b^+ e^{-ik_b(x-x_f)+i\omega t} + A_b^- e^{ik_b(x-x_f)+i\omega t} \tag{2.34}$$

$$u_1^b(x,t) = \frac{A_b^+}{\rho_b c_b} e^{-ik_b(x-x_f)+i\omega t} - \frac{A_b^-}{\rho_b c_b} e^{ik_b(x-x_f)+i\omega t} \tag{2.35}$$

Boundary conditions:

At the closed end ($x = 0$) where $u_1^f(x,t) = 0$, we have:

$$\boxed{A_f^+ e^{ik_f x_f} - A_f^- e^{-ik_f x_f} = 0} \tag{2.36}$$

At the open end ($x = L$) where $p_1^b(x,t) = 0$, we get:

$$\boxed{A_b^+ e^{-ik_b(L-x_f)} + A_b^- e^{ik_b(L-x_f)} = 0} \tag{2.37}$$

Jump conditions across the flame ($x = x_f$):

Pressure continuity:

$$\boxed{A_f^+ + A_f^- = A_b^+ + A_b^-} \tag{2.38}$$

Acoustic jump:

$$\zeta[A_b^+ - A_b^-] - [A_f^+ - A_f^-] = \frac{(\gamma-1)}{c_f} Q_1 \tag{2.39}$$

Here, $\zeta = \rho_f c_f / \rho_b c_b$ is the coupling parameter.

Crocco's model:

At flame position $x = x_f$, the velocity fluctuations $u_1^f = \frac{A_f^+ - A_f^-}{\rho_f c_f} e^{i\omega t}$, substituting this in the Crocco's model eq.(2.28), we get:

$$\frac{\gamma-1}{\rho_f c_f^2} Q_1 = n \frac{(A_f^+ - A_f^-)}{\rho_f c_f} e^{i\omega\tau_d} \tag{2.40}$$

Furthermore, the acoustic jump condition can now be written as:

$$\boxed{[A_f^+ - A_f^-][1 + ne^{i\omega\tau_d}] - \zeta[A_b^+ - A_b^-] = 0} \tag{2.41}$$

Using the equations highlighted above, we can rearrange the terms to create a matrix in the form of $[M][A] = 0$:

$$\begin{bmatrix} e^{ik_f x_f} & -e^{-ik_f x_f} & 0 & 0 \\ 0 & 0 & e^{-ik_b(L-x_f)} & e^{ik_b(L-x_f)} \\ 1 & 1 & -1 & -1 \\ [1+ne^{i\omega\tau_d}] & -[1+ne^{i\omega\tau_d}] & -\zeta & \zeta \end{bmatrix} \cdot \begin{bmatrix} A_f^+ \\ A_f^- \\ A_b^+ \\ A_b^- \end{bmatrix} = \begin{bmatrix} 0 \\ 0 \\ 0 \\ 0 \end{bmatrix} \tag{2.42}$$

The dispersion relation can be derived by setting the determinant of the matrix to zero ($\det(M) = 0$). This yields the following equation:

$$\zeta \cos(k_f x_f)\cos(k_b(L-x_f)) - \sin(k_f x_f)\sin(k_b(L-x_f))[1+ne^{i\omega\tau_d}] = 0 \tag{2.43}$$

This expression can be further simplified to:

$$\tan\left(\frac{2\pi f x_f}{c_f}\right)\tan\left(\frac{2\pi f(L-x_f)}{c_b}\right)[1+ne^{i\omega\tau_d}] = \zeta \tag{2.44}$$

The eigen mode frequency (f) of the channel can be determined by solving eq.(2.44) with specific values for the interaction index (n) and time delay (τ_d). However, even in the absence of these parameter values (i.e., assuming $n = 0$, indicating no flame dynamics), we can still discern several essential Eigenmode characteristics of open-closed channels:

- When the channel contains fresh gases only (i.e., with the flame situated at $x_f = L$), eq.(2.44) simplifies to the quarter-wave resonant mode for fresh gases:

$$f_f = \frac{(2m+1)c_f}{4L} \quad (m \geq 0) \tag{2.45}$$

Here, f_f represents the eigenfrequency in this scenario.

- In contrast, in the absence of fresh gases and when the flame resides at $x_f = 0$ (resulting in only burnt gases), we obtain:

$$f_b = \frac{(2m+1)c_b}{4L} \quad (m \geq 0) \tag{2.46}$$

  Since the speed of sound in hot burnt gases ($c_b = \sqrt{\gamma \frac{R}{W} T_b}$) exceeds that in fresh gases, the quarter-wave resonant mode of the chamber experiences an increase by a factor of c_b/c_f.

- For a flame positioned anywhere within the channel, the eigenfrequency (f) lies within the range bounded by f_f and f_b, depending on the position of the flame (x_f). This illustrates the significant influence of the flame placement on the eigenfrequency of the system. Consequently, a propagating flame within such a channel encounters a spectrum of distinct frequencies in contrast to stationary flames.

2.4 Summary

In this chapter, we introduced foundational concepts and mechanisms related to combustion instabilities. We explored the formation and growth of the Darrieus-Landau instability, emphasizing the role of stretch in stabilizing flame fronts at larger wavenumbers. Furthermore, we conducted a comprehensive analysis of thermoacoustic instabilities, examining flame responses to varying acoustic wave conditions, the generation of acoustic waves from unsteady heat release rates, and the coupling mechanism. We also touched on the criteria for the growth of these instabilities. Additionally, we derived the eigenmodes of flames in open-closed channels, highlighting the dependence of the eigenfrequency on the flame's position.

With this foundation, we can now proceed to explain our numerical solver based on the Lattice Boltzmann Method.

Chapter 3

Numerical Combustion with Lattice Boltzmann Method

Contents

3.1 Introduction 43

3.2 Lattice Boltzmann Method 44

3.2.1 Boltzmann Equation 44

3.2.2 Discrete Velocity Boltzmann Equation 46

3.2.3 Lattice Boltzmann Equation 47

3.2.4 Typical Algorithm of Lattice Boltzmann Method 49

3.3 Hybrid Lattice Boltzmann Method for Reactive Flows . . 54

3.3.1 Hybrid Solver 55

3.3.2 Collision Kernels 56

3.3.3 Pressure based LBM 57

3.4 Boundary Conditions 59

3.4.1 NRI-NSCBC 61

3.5 Summary 62

3.1 Introduction

Lattice Boltzmann Methods (LBMs) are numerical algorithms grounded in the Kinetic theory of gases. Stemming from a velocity-discretized rendition of the Boltzmann

equation on a lattice grid, they often contain the essential information required to solve fluid dynamics equations on macroscopic scales[1]. Unlike traditional Navier-Stokes-based strategies that directly tackle macroscopic quantities like density and velocity, LBMs emphasize tracking the distribution of discrete particles. The moments of these distributions then subsequently yield the macroscopic quantities. Such a distinctive methodology has endowed LBM certain algorithmic advantages, making them particularly adept in terms of computational efficiency and favourable dissipation properties.

Due to these advantageous features, there has been a rapid development, and subsequent adoption of the LBM for low-Mach external aerodynamics and aeroacoustics. However, its application in high-Mach flows and combustion had been limited due to the absence of a good compressible realization and stability issues. Recently, significant progress has been made in these domains, thanks to the improvement of stability issues through advanced collision models [23, 48] and the adoption of Double Distribution Functions [45, 86] (DDF) or Hybrid solvers [22, 104] to account for energy and species transport.

In this chapter, we present a concise overview of the fundamental concepts behind the Lattice Boltzmann Method, beginning with an introduction to the continuous Boltzmann equation and the subsequent derivation of the Lattice Boltzmann Method. Following this, we highlight the particular modifications incorporated into our model, including the HRR collision kernel, the equilibrium function, and the hybrid structure for energy and species transport, all of which are essential for simulating reactive flows. Additionally, we provide a brief introduction to the incorporation of boundary conditions into our model.

3.2 Lattice Boltzmann Method

3.2.1 Boltzmann Equation

The Boltzmann equation (BE) provides a kinetic description of a gas that is out of thermodynamic equilibrium. In the absence of external forces, and assuming the gas consists of small hard spherical particles undergoing elastic collisions, the BE can be expressed as follows:

$$\boxed{\frac{\partial f}{\partial t} + \xi_\alpha \frac{\partial f}{\partial x_\alpha} = \Omega(f)} \tag{3.1}$$

[1]Chapmann-Enskog analysis and recently, Taylor analysis have been used to explicitly show this correlation.

Here, $f(\boldsymbol{\xi}, \boldsymbol{x}, t)$ represents the **particle distribution function**, which quantifies the density of particles (mass) with velocity vector $\boldsymbol{\xi}$, located at $\boldsymbol{x}$ at time t, and therefore f has the units $(\text{kg s}^3)/\text{m}^6$.

The left-hand side of equation (3.1) represents the free streaming of particles, akin to the advection of the distribution function f with the velocity $\boldsymbol{\xi}$. On the other hand, the term $\Omega(f)$ on the right-hand side accounts for the effects of particle collisions, resulting in the local redistribution of f. Typically, the collision operator $\Omega(f)$ is expressed using the Bhathagar-Gross-Krook (BGK) collision operator [8]:

$$\Omega^{BGK}(f) = -\frac{1}{\tau}(f - f^{eq}) \tag{3.2}$$

where τ is the characteristic relaxation time that controls the relaxation of f towards its equilibrium. The gas kinetic theory dictates that for a monoatomic gas, the distribution function f will relax through collisions toward a Maxwellian **equilibrium distribution function** f^{eq} [70], given by:

$$f^{eq} = \frac{\rho}{(2\pi RT)^{3/2}} e^{-(||\boldsymbol{\xi}-\boldsymbol{u}||^2)/2RT} \tag{3.3}$$

Furthermore, for mass, momentum, and energy to be conserved through collisions, they must relate to the particle distribution function f as:

$$\rho = \int f d\boldsymbol{\xi} = \int f^{eq} d\boldsymbol{\xi}, \tag{3.4}$$

$$\rho u_\alpha = \int \xi_\alpha f d\boldsymbol{\xi} = \int \xi_\alpha f^{eq} d\boldsymbol{\xi}, \tag{3.5}$$

$$\rho E = \frac{1}{2} \int \xi_\alpha \xi_\alpha f d\boldsymbol{\xi} = \frac{1}{2} \int \xi_\alpha \xi_\alpha f^{eq} d\boldsymbol{\xi}, \tag{3.6}$$

Here, the integrals are computed over the entire velocity space. Note that these moments allow us to compute macroscopic quantities like ρ, $\boldsymbol{u}$ and E. However, it is crucial to emphasize that the expression for total energy density in Equation (3.6) accounts solely for translational energy. As such, it does not provide all the relevant information necessary for understanding polyatomic gases, and will not be considered from now on.

Similarly, by taking moments of the Boltzmann equation (3.1), it is possible to derive macroscopic equations that govern fluid mechanics: Equations (1.2), (1.3), and (1.4). This derivation, detailed in [53], underscores that the mass conservation equation remains invariant and exact, while the formulation of the momentum and energy conservation equations is depend on the stress tensor and heat flux vector, which themselves

depend on the form of f [53].

3.2.2 Discrete Velocity Boltzmann Equation

Now that the Boltzmann equation (BE) has been established as the foundation for deriving fluid dynamics equations at a macroscopic scale, it raises the intriguing possibility of deducing solutions for the Navier-Stokes equations (NSE) from BE solutions. However, the analytical complexity of the BE, which depends on seven variables x, y, z, ξ_x, ξ_y, ξ_z and t, makes it even more difficult to solve analytically than NSE. Alternatively, numerical solutions for the BE could indirectly yield NSE solutions. Remarkably, the numerical scheme for the BE is surprisingly straightforward to implement. This is the idea behind the Lattice Boltzmann Methods (LBMs).

Beyond the conventional temporal and spatial discretization on Cartesian grids, a distinctive characteristic distinguishing the continuous Boltzmann Equation (BE) from its discretized counterpart lies in the discretization of the velocity space over lattice grids. Rather than delving into the mathematical intricacies of this transformation at this point, we will provide a brief overview of the fundamental concept behind it.

Whilst preserving conservation laws it is possible to

1. Simplify and express the distribution functions f and f^{eq} using Hermite polynomial series $\mathcal{H}^{(n)}$.

2. Apply the Gauss-Hermite quadrature rule to compute moment integrals using a limited number of discrete velocities $\boldsymbol{c}_i$ [44, 85, 114].

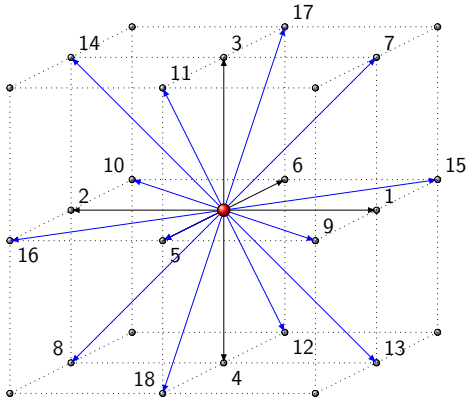

Figure 3.1: Illustration of D3Q19 velocity set.

These discrete velocities belong to velocity sets $\{\boldsymbol{c}_i w_i\}$, comprising q discrete velocities within a d-dimensional lattice, accompanied by their corresponding

weighting coefficients w_i. This arrangement is commonly referred to as a DdQq lattice. It is essential that these velocity sets not only adhere to the conservation of mass and momentum but also maintain the rotational isotropy of the Navier-Stokes equations. However, in practice, due to the adoption of smaller lattices (less velocities), isotropy defects may exist, which can be corrected by introducing additional forcing terms. The specific D3Q19 lattice used in our study is illustrated in Figure 3.1, with its corresponding weighting coefficients w_i and discrete velocities $\boldsymbol{c}_i$ detailed in the accompanying table 3.1.

i	0	1	2	3	4	5	6	7	8	9	10	11	12	13	14	15	16	17	18
w_i	$\frac{1}{3}$	$\frac{1}{18}$	$\frac{1}{18}$	$\frac{1}{18}$	$\frac{1}{18}$	$\frac{1}{18}$	$\frac{1}{18}$	$\frac{1}{36}$	$\frac{1}{36}$	$\frac{1}{36}$	$\frac{1}{36}$	$\frac{1}{36}$	$\frac{1}{36}$	$\frac{1}{36}$	$\frac{1}{36}$	$\frac{1}{36}$	$\frac{1}{36}$	$\frac{1}{36}$	$\frac{1}{36}$
c_{ix}	0	+1	-1	0	0	0	0	+1	-1	+1	-1	0	0	+1	-1	+1	-1	0	0
c_{iy}	0	0	0	+1	-1	0	0	+1	-1	0	0	+1	-1	-1	+1	0	0	+1	-1
c_{iz}	0	0	0	0	0	+1	-1	0	0	+1	-1	+1	-1	0	0	-1	+1	-1	+1

Table 3.1: Discrete velocities $\boldsymbol{c}_i$ and weights w_i of a D3Q19 velocity set.

As a result both f and f^{eq} are simplified and transformed from continuous to discrete in velocity space. Eqs. (3.4) and (3.5) can now be written as:

$$\rho = \sum_{i=1}^{q} f_i = \sum_{i=1}^{q} f_i^{eq}, \tag{3.7}$$

$$\rho u_\alpha = \sum_{i=1}^{q} c_{i\alpha} f_i = \sum_{i=1}^{q} c_{i\alpha} f_i^{eq}, \tag{3.8}$$

where f_i and f_i^{eq} denote the discretized probability density functions, corresponding to their BE counterparts. Consequently, the BE itself undergoes discretization, leading to the need to solve q distinct Boltzmann equations, one for each discrete velocity $c_{i\alpha}$

$$\boxed{\frac{\partial f_i}{\partial t} + c_{i\alpha}\frac{\partial f_i}{\partial x_\alpha} = \Omega_i} \tag{3.9}$$

Equation (3.9) is referred to as the Discrete Velocity Boltzmann Equation (DVBE)

3.2.3 Lattice Boltzmann Equation

The final transformation of the Boltzmann Equation (BE) into the Lattice Boltzmann Equation (LBE) involves the space and time discretization. Unlike finite volume or finite

element methods, where each volume or element can have many possible shapes, such as triangles, quads, tetrahedra, pyramids or hexes, the "classical" Lattice Boltzmann Method (LBM) primarily relies on a structured grid. While there are instances of LBM discretizations on unstructured grids [74, 109], the classical approach employs a regular grid, which tightly couples spatial and temporal discretizations within the LBM framework.

The fundamental assumption of the LBM lies in the notion that populations f_i move with discrete velocities $\boldsymbol{c}_i$ from one lattice site to another. In a single time step Δt, these populations are expected to precisely reach neighboring sites without getting stuck between lattice sites. This precise propagation is ensured under two key conditions: (i) the underlying spatial lattice remains uniform and regular, characterized by a lattice constant Δx, and (ii) the velocity components are integer multiples of $\Delta x/\Delta t$, specifically $c_{i\alpha} = n\Delta x/\Delta t$. Remarkably, this condition is satisfied by all discrete velocity sets [85, 114].

Discretization of space and time

The left-hand side of the Discrete Velocity Boltzmann Equation (DVBE) in equation (3.9), representing particle streaming or advection, takes the form of a linear first-order hyperbolic Partial Differential Equation (PDE). As such, the method of characteristics can be applied to perform an exact integration between time steps t and $t+\Delta t$. However, the right-hand side, corresponding to the collision process, is non-linear. To achieve a certain level of accuracy, space-time integration techniques such as Crank-Nicolson (trapezoidal rule), Runge-Kutta, and explicit forward Euler schemes can be employed.

Using the method of characteristics on the the linear term and a second-order discretization via the trapezoidal rule to approximate the collision term, the following equation is obtained:

$$f_i(t+\Delta t, \boldsymbol{x}) - f_i(t, \boldsymbol{x} - \boldsymbol{c}_i\Delta t) = \Delta t \frac{\Omega_i(t, \boldsymbol{x} - \boldsymbol{c}_i\Delta t) + \Omega_i\left(t+\Delta t, \boldsymbol{x}\right)}{2} \tag{3.10}$$

Equation (3.10) is implicit due to the dependence of $\Omega_i\left(t+\Delta t, \boldsymbol{x}\right)$ on f_i at the time step $t+\Delta t$. However, it can be transformed into an explicit form, as demonstrated in [53]. This transformation involves a change of variables from f_i to $\bar{f}_i$

$$\bar{f}_i = f_i - \frac{\Omega_i \Delta t}{2} \tag{3.11}$$

and results in the equation:

$$\bar{f}_i\left(t+\Delta t, \boldsymbol{x}\right) = \bar{f}_i(t, \boldsymbol{x}-\boldsymbol{c}_i\Delta t) + \Delta t\bar{\Omega}_i(t, \boldsymbol{x}-\boldsymbol{c}_i\Delta t) \tag{3.12}$$

Here, $\bar{\Omega}_i$ represents a slightly redefined collision operator. Notably, all common collision operators can be re-expressed using $\bar{f}_i$ instead of f_i [53]. This redefinition holds significance due to its preservation of conservation properties: $\sum_i \bar{f}_i = \sum_i f_i = \rho$ and $\sum_i \boldsymbol{c}_i\bar{f}_i = \sum_i \boldsymbol{c}_i f_i = \rho\boldsymbol{u}$.

An illustration of a second-order accurate redefined collision operator can be provided through the example of the velocity-discretzed rendition of the BGK collision kernel eq.(3.2). When considering a modified distribution population $\bar{f}$, the BGK collision operator Ω_i^{BGK} can be transformed into $\bar{\Omega}_i^{BGK}$ by:

$$\bar{\Omega}_i^{BGK}(\bar{f}) = -\frac{1}{\bar{\tau}}(\bar{f}_i - f_i^{eq}) \tag{3.13}$$

where, $\bar{\tau}$ is expressed as $\bar{\tau} = \tau + \Delta t/2$, and τ represents the characteristic relaxation time associated with the fluid viscosity:

$$\tau = \frac{\mu}{\rho c_s^2} \tag{3.14}$$

with $c_s = \Delta x/(\sqrt{3}\Delta t)$ signifying the lattice sound speed for standard lattices.

Considering this modified BGK collision operator, the Lattice Boltzmann Equation can be written as:

$$\boxed{\bar{f}_i\left(t+\Delta t, \boldsymbol{x}\right) - \bar{f}_i(t, \boldsymbol{x}-\boldsymbol{c}_i\Delta t) = -\frac{\Delta t}{\bar{\tau}}\left[\bar{f}_i(t, \boldsymbol{x}-\boldsymbol{c}_i\Delta t) - f_i^{eq}(t, \boldsymbol{x}-\boldsymbol{c}_i\Delta t)\right]} \tag{3.15}$$

3.2.4 Typical Algorithm of Lattice Boltzmann Method

At its core, the algorithm revolves around the collision and streaming steps. The Lattice Boltzmann Equation (LBE) with the BGK approximation (Eq. 3.15) can be decomposed into two distinct steps:

- **Collision:**

$$f_i^{col}(t, \boldsymbol{x}) = \bar{f}_i(t, \boldsymbol{x})\left(1 - \frac{\Delta t}{\bar{\tau}}\right) + f_i^{eq}(t, \boldsymbol{x})\frac{\Delta t}{\bar{\tau}} \tag{3.16}$$

  The collision step involves computing the non-linear component responsible for particle collisions and subsequent relaxation toward equilibrium. And as observed

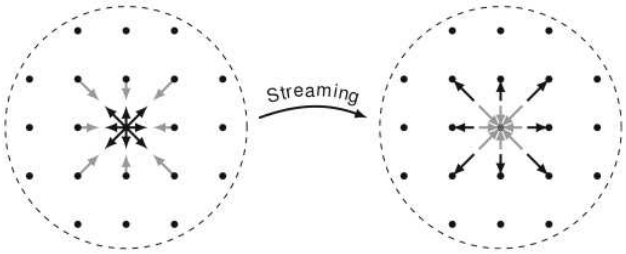

Figure 3.2: Illustration of streaming particles. The left-side figure represents the post-collide distributions f_i^{col} before streaming, and the right-side figure illustrates the pre-collision distributions $\bar{f}_i$ after streaming. This image is sourced from [53].

in the eq.(3.16), the evaluation of this collision term is performed locally within each node, which offers significant advantages for parallelization.

- **Streaming:**

$$\bar{f}_i(t + \Delta t, \boldsymbol{x}) = f_i^{col}\left(t, \boldsymbol{x} - \boldsymbol{c}_i \Delta t\right) \tag{3.17}$$

Conversely, the streaming step, responsible for particle advection, is non-local in nature. However, it is a linear operation, which, from a numerical standpoint, involves only the changing of node indices (fig. 3.2). As a result, advection is exact, leading to low numerical dissipation properties. This is in contrast to conventional methods, such as finite difference or finite volume techniques, which encounter challenges when discretizing equations of fluid mechanics, especially the advection term $(\boldsymbol{u} \cdot \nabla)\boldsymbol{u}$. These conventional methods often require complex iterative numerical schemes and introduce approximation errors.

With the core algorithm of the Lattice Boltzmann Method (LBM) and its associated advantages now comprehensively explained, we can proceed to introduce the complementary components necessary to complete this method. To start, let us introduce some LB-specific variables:

- **Hermite polynomials:** Hermite polynomials play a pivotal role in evaluating the equilibrium distribution function f_i^{eq}, due to their orthogonality with the Gaussian distribution. This particular distribution is representative of the Maxwell-Boltzmann thermal equilibrium, hence facilitates the easy separation of distribution functions into their constitutive moments. They are also used to

define a correction forcing term F_i. The polynomials read:

$$\begin{aligned}
\mathcal{H}_i^{(0)} &= 1, \\
\mathcal{H}_{i\alpha}^{(1)} &= c_{i\alpha}, \\
\mathcal{H}_{i\alpha\beta}^{(2)} &= c_{i\alpha}c_{i\beta} - c_s^2\delta_{\alpha\beta}, \\
\mathcal{H}_{i\alpha\beta\gamma}^{(3)} &= c_{i\alpha}c_{i\beta}c_{i\gamma} - c_s^2\left[c_{i\alpha}\delta_{\beta\gamma} + c_{i\beta}\delta_{\gamma\alpha} + c_{i\gamma}\delta_{\alpha\beta}\right],
\end{aligned} \tag{3.18}$$

Here, α, β and γ are the co-ordinate indices, and $\delta_{\alpha\beta}$ is the Kronecker symbol. It is worth noting that higher-order Hermite polynomials usually do not significantly impact the underlying physics, particularly the preservation of conservation laws, as these particular expansions do not mix the lower order moments of the NS equation with higher order moments related to energy and beyond [53]. Thus, for computational efficiency, higher-order terms are be disregarded.

- **Moments**: For an arbitrary population f, Hermite moments $a^{f,(n)}_{\alpha_1\ldots\alpha_n}$, and the macroscopic moments $\Pi^{f,(n)}_{\alpha_1\ldots\alpha_n}$ can be defined as follows:

$$a^{f,(n)}_{\alpha_1\ldots\alpha_n} = \sum_i^q \mathcal{H}^{(n)}_{i\alpha 1\ldots\alpha_n} f_i \tag{3.19}$$

$$\Pi^{f,(n)}_{\alpha_1\ldots\alpha_n} = \sum_i^q c_{i\alpha_1}\ldots c_{i\alpha_n} f_i \tag{3.20}$$

It's important to acknowledge that due to the finite number of discrete velocities, there inevitably exists a non-zero isotropy defect $D^{(n)}_{\alpha_1\ldots\alpha_n}$ between continuous and discrete moments:

$$D^{f,(n)}_{\alpha_1\ldots\alpha_n} = \int c_{\alpha_1}\ldots c_{\alpha_n} f dc - \Pi^{f,(n)}_{\alpha_1\ldots\alpha_n} \neq 0 \tag{3.21}$$

In lattices involving nearest-neighbors, this isotropy defect emerges starting from the third order ($n = 3$) [53]. These isotropy defects can be mitigated through the incorporation of the correction forcing term F_i.

- **Distribution functions:** All the distribution functions involved in the LBM algorithm are outlined here:

- f^{eq}, the equilibrium distribution function:

$$f_i^{eq} = \omega_i \left\{ \mathcal{H}^{(0)} a^{f^{eq},(0)} + \frac{\mathcal{H}^{(1)}_{i\alpha}}{c_s^2} a_\alpha^{f^{eq},(1)} + \frac{\mathcal{H}^{(2)}_{i\alpha\beta}}{2c_s^4} a_{\alpha\beta}^{f^{eq},(2)} + \frac{\mathcal{H}^{(3)}_{\alpha\alpha\beta\gamma}}{6c_s^6} a_{\alpha\beta\gamma}^{f^{eq},(3)} \right\} \tag{3.22}$$

with the Hermite equilibrium moments generally defined as:

$$\begin{aligned} a^{f^{\mathrm{eq}},(0)} &= \rho \\ a_\alpha^{f^{\mathrm{eq}},(1)} &= \rho u_\alpha \\ a_{\alpha\beta}^{f^{\mathrm{eq}},(2)} &= \rho u_\alpha u_\beta \\ a_{\alpha\beta\gamma}^{f^{\mathrm{eq}},(3)} &= \rho u_\alpha u_\beta u_\gamma \end{aligned} \tag{3.23}$$

- F_i, the forcing term:

$$F_i = \omega_i \left\{ \mathcal{H}^{(0)} a^{F,(0)} + \frac{\mathcal{H}^{(1)}_{i\alpha}}{c_s^2} a_\alpha^{F,(1)} + \frac{\mathcal{H}^{(2)}_{i\alpha\beta}}{2c_s^4} a_{\alpha\beta}^{F,(2)} \right\} \tag{3.24}$$

It is introduced to correct for rotational isotropic defects, the viscous tensor and add external forces such as gravity.

- f^{neq}, the non-equilibrium distribution function :

$$f_i^{neq} = f_i - f_i^{eq} \tag{3.25}$$

It represents the deviation of f_i from f_i^{eq} and is crucial for calculating viscous fluids. The modified non-equilibrium distribution function for a BGK collision kernel is expressed as:

$$\bar{f}_i^{neq} = \bar{f}_i - f_i^{eq} + \frac{\Delta t}{2} F_i \tag{3.26}$$

However, in this study, to obtain a physically accurate viscous stress tensor, the non-equilibrium distribution function for advanced collision Kernels (eg: regularized kernels) are expressed based on the filtered projection of $f_i^{\bar{n}eq}$ onto a Hermite basis:

$$f_i^{\bar{n}eq} = \omega_i \left\{ \frac{\mathcal{H}^{(2)}_{i\alpha\beta}}{2c_s^4} a_{\alpha\beta}^{f^{neq},(2)} + \frac{\mathcal{H}^{(3)}_{i\alpha\beta\gamma}}{6c_s^6} a_{\alpha\beta\gamma}^{f^{neq},(3)} \right\} \tag{3.27}$$

- f_i^{col}, the post-collide distribution function considering the forcing term and the non-equilibrium terms can be expressed as:

$$f_i^{col} = f_i^{eq} + \left(1 - \frac{\Delta t}{\bar{\tau}}\right) \bar{f}_i^{neq} + \frac{\Delta t}{2} F_i \tag{3.28}$$

► $\bar{f}_i$, the post-stream distribution function after streaming, at $(t + \Delta t)$:

$$\bar{f}_i(t + \Delta t, \boldsymbol{x}) = f_i^{col}\left(t, \boldsymbol{x} - \boldsymbol{c}_i \Delta t\right) \tag{3.29}$$

- **Macroscopic Quantities:**

$$\Pi_{\alpha_1 \ldots \alpha_n}^{\bar{f},(n),(t+\Delta t,x)} = \sum_i^q c_{i\alpha_1} \ldots c_{i\alpha_n} \bar{f}_i(t + \Delta t, x) \tag{3.30}$$

for example, in conventional Lattice Boltzmann Method (LBM), the zeroth and first-order moments describe the density and momentum at the next time step:

$$\begin{aligned} \rho(t + \Delta t, \boldsymbol{x}) &= \sum_i^q \bar{f}_i(t + \Delta t, \boldsymbol{x}) \\ \rho u_\alpha(t + \Delta t, \boldsymbol{x}) &= \sum_i^q c_{i\alpha_1} \bar{f}_i(t + \Delta t, \boldsymbol{x}) \end{aligned} \tag{3.31}$$

Overview of the LB algorithm :

The steps involved in a typical LBM algorithm are now summarized in table 3.2.

Step	Description	Input	Output	Equation
1	Equilibrium update	Macroscopic	f_i^{eq}	(3.22)
2	Force update	Macroscopic	F_i	(3.24)
3	Non-equilibrium update	f_i^{eq}, F_i	f_i^{neq}	(3.26) (BGK)
4	Collision	f_i^{eq}, f_i^{neq}, F_i	f_i^{col}	(3.28)
5	Streaming	$f_i^{col}\left(t, \boldsymbol{x} - \boldsymbol{c_i} \Delta t\right)$	$\bar{f}_i(t + \Delta t, \boldsymbol{x})$	(3.29)
6	Macroscopic quantities update	$\bar{f}_i(t + \Delta t, \boldsymbol{x})$	Macroscopic	(3.30)

Table 3.2: Generic structure of an LBM

1. Step 1 involves evaluating equilibrium distribution function from the macroscopic quantities. Additionally, step 1 and 6 establish the connection between macroscopic quantities and the distribution functions.

2. Step 2 involves updating the correction forcing term to address isotropy defects and to incorporate external forces such as gravity, if necessary.

3. Step 3 encompasses the definition of the collision kernel. The computation of f_i^{neq} in this step is closely tied to the chosen collision model, such as BGK [8], multi-relaxation times models [31, 54] , regularized models [48], and others.

4. Step 4 is the collision step.

5. Step 5 is the streaming step.

6. Step 6 involves the update of the macroscopic quantities from the distributions and then back to the step 1 for the next iteration.

3.3 Hybrid Lattice Boltzmann Method for Reactive Flows

In this section, building on the previously discussed Lattice Boltzmann Method (LBM), we introduce the formulation of the **Pressure-based Hybrid Lattice Boltzmann Method**. This thesis focuses on validating and applying this solver to various cases related to thermoacoustic instabilities.

To adapt the conventional LBM (outlined in tab.3.2) for reactive flows, several enhancements are essential. The three primary of which are:

1. **Hybrid Solver:** To solve for total energy (E) and species (Y_k), both of which are essential for reactive flows, we employ an "ad-hoc" finite-difference-like solver. This solver works in tandem with the LB solver that addresses density (ρ) and momentum ($\rho\boldsymbol{u}$).

2. **HRR Collision kernel:** The collision kernels significantly influence stability in the non-isothermal cases. We adopt the Hybrid Recursive Regularized collision kernel (HRR) [48] in our work.

3. **Pressure based LBM:** Introduced by Farag et al. [36] for simulating non-isothermal flows, this solver addresses spurious pressure fluctuations often observed in previous LBM implementations for high-speed non-isothermal flows. Recent research by Tayyab [104] has shown that this LBM solver can effectively handle large density fluctuations, a crucial aspect in simulating reactive flows, and hence will be employed in our work.

The following sub-sections provide detailed insights into each of these additions.

3.3.1 Hybrid Solver

As stated earlier, for multi-species reactive flows, accurately determining the total energy density (ρE), and species mass fractions (ρY_k) are pivotal. While various methods like multi-speed [40, 41] and Double Distribution Functions [45, 86], employ LB techniques for this purpose, they often entail significant simplifications or become costly [24] when addressing the vast array of species involved in chemical reactions. In such cases, a hybrid approach leveraging conventional NS-based methods for transporting ρE and ρY_k becomes more effective.

Guided by this rationale, we employ a hybrid strategy where ρ and $\rho \boldsymbol{u}$ are computed using the LB method, and the evaluations of ρE and ρY_k are performed using a specially-designed "ad-hoc" Finite Difference like solver that is consistent with the LB solver. Delving deeper into the specifics of this Finite Difference like solver:

- The temporal integration is carried out using an explicit first-order Euler scheme.
- The thermal and species diffusion are evaluated by utilizing a conservative second-order centered numerical schemes [103, 106].
- Furthermore, the consistency between the Lattice Boltzmann Method (LBM) and Finite Difference (FD) methods is established by leveraging LBM populations to evaluate convective terms in energy and species transport equations [116].

  In particular, the total energy flux is determined using the pseduo-DDF method [117] as follows:

$$\nabla \cdot (\rho \boldsymbol{u} H) = \frac{1}{\Delta t} \sum_i \left[f_i^H(\boldsymbol{x}, t) - f_i^H(\boldsymbol{x} - \boldsymbol{c_i} \Delta t, t) \right] \tag{3.32}$$

  where,

$$f_i^H(\boldsymbol{x}, t) \equiv H(\boldsymbol{x}, t) f_i(\boldsymbol{x}, t) + f_i^{H,\mathrm{neq}}(\boldsymbol{x}, t). \tag{3.33}$$

  The non-equilibrium counterpart $f_i^{H,\mathrm{neq}}$ is explicitly detailed in [117].

  Similarly, the species flux is resolved using the monotone numerical scheme pro-

posed in [78, 116] specially designed for mass fraction transport,

$$\nabla \cdot (\rho \boldsymbol{u} Y_k) \equiv -\sum_i \Delta m_i \begin{cases} Y_k(\boldsymbol{x}, t) & \text{if } \Delta m_i \leq 0 \\ Y_k(\boldsymbol{x} + \boldsymbol{c_i}\Delta t, t) & \text{otherwise.} \end{cases} \tag{3.34}$$

where $\Delta m_i \equiv f_{\bar{i}}(\boldsymbol{x} + \boldsymbol{c_i}\Delta t) - f_i(\boldsymbol{x})$ and $\bar{i}$ represents the lattice in the opposite direction of i. This numerical scheme constructs the species flux by considering the difference in the probability distribution function (PDF) of the species between neighboring lattices.

3.3.2 Collision Kernels

Before delving into the formulation of the Hybrid Recursive Regularized collision kernel, let us first examine the motivation behind transitioning from a simple BGK collision kernel to the more advanced collision kernels.

According to Chapman-Enskog expansion and Taylor analysis, it is well known that the second moment of the non-equilibrium distribution function$-\Pi_{\alpha\beta}^{f^{neq},(2)}$ corresponds to the stress tensor $\mathcal{T}_{\alpha\beta}$ [37, 53]. Additionally, Farag et al. [37] demonstrated from Taylor analysis that $\Pi_{\alpha_1\ldots\alpha_{n+1}}^{f,(n+1)}$ is always the flux of $\Pi_{\alpha_1\ldots\alpha_n}^{f,(n)}$. Hence, $\Pi_{\alpha\beta}^{f^{neq},(2)}$ has its own evolution equation influenced by higher-order contributions $\Pi_{\alpha\beta\gamma}^{f^{neq},(3)}$ at $(n = 3)$, which are known to contain non-physical contributions due to isotropy defects.

Consequently, when using a simple BGK collision kernel, the presence of these non-physical contributions can lead to inaccuracies in the computation of the stress tensor, causing it to deviate from the physically accurate stress tensor ($\mathcal{T}_{\alpha\beta}$) of the Navier-Stokes equations (NSE). Additionally, among the various moments involved in the evolution equation of $\Pi_{\alpha\beta}^{f^{neq},(2)}$, $\Pi_{\alpha\beta\gamma}^{f^{neq},(3)}$ is the only moment that does not appear in the mass and momentum conservation equations. This unique property makes it a suitable candidate for modeling a physically accurate stress tensor. This insight forms the basis for the development of more advanced collision kernels:

- Regularized kernel [56, 69]: These collision kernels entirely neglect the contribution of $\Pi_{\alpha\beta\gamma}^{f^{neq},(3)}$ during the collision process, effectively filtering out the non-physical contributions.

$$\bar{f}_i^{\text{neq}} = \omega_i \frac{\mathcal{H}_{i\alpha\beta}^{(2)}}{2c_s^4} \Pi_{\alpha\beta}^{\bar{f}^{\text{neq}},(2)} \tag{3.35}$$

- Recursive Regularized kernel (RR) [23]: Instead of discarding $\Pi^{f^{neq},(3)}_{\alpha\beta\gamma}$ entirely, this approach replaces it with an approximation derived from the Chapman-Enskog (CE) expansion.

$$\bar{f}_i^{\text{neq}} = \omega_i \left\{ \frac{\mathcal{H}^{(2)}_{i\alpha\beta}}{2c_s^4} \Pi^{\bar{f}^{\text{neq}},(2)}_{\alpha\beta} + \frac{\mathcal{H}^{(3)}_{i\alpha\beta\gamma}}{6c_s^6} \left(u_\alpha \Pi^{\bar{f}^{\text{neq}},(2)}_{\beta\gamma} + u_\beta \Pi^{\bar{f}^{\text{neq}},(2)}_{\gamma\alpha} + u_\gamma \Pi^{\bar{f}^{\text{neq}},(2)}_{\alpha\beta} \right) \right\} \tag{3.36}$$

- Hybrid Recursive Regularized kernel (HRR) [48]: By introducing a parameter $\sigma_{HRR} \in [0, 1]$, this approach allows for the adjustment of $\Pi^{\bar{f}^{neq},(2)}_{\alpha\beta}$ in (3.36), towards or away from $\mathcal{T}_{\alpha\beta}$ during the non-equilibrium reconstruction process

$$\Pi^{\bar{f}^{\text{neq}},(2)}_{\alpha\beta} = \sigma_{HRR} \sum_{i=1}^{q} c_{i\alpha} c_{i\beta} \left(\bar{f}_i - f_i^{eq} + \frac{\Delta t}{2} F_i \right) - (1 - \sigma_{HRR}) \rho c_s^2 \bar{\tau} \left(\mathcal{T}_{\alpha\beta} \right)_{FD} \tag{3.37}$$

where the first term is the direct projection of $\bar{f}_i^{neq}$ and the last term represents the stress tensor evaluated using a second order Finite-Difference scheme. It was observed that using $\sigma_{HRR} < 1$ introduces hyper-viscosity [48]. Therefore, for our thermo-acoustic simulations, we have opted to set the value of σ_{HRR} to 0.98.

3.3.3 Pressure based LBM

With a grasp of the Hybrid solver and the HRR collision kernel, we can now delve into the pressure-based method, the other crucial component of our Hybrid LBM solver. It is worth emphasizing that the pressure-based technique employed in our LBM [36] elucidated below differs from the conventional Navier-Stokes pressure-based method.

The algorithm of this LBM solver follows a similar approach to the typical LBM solver, as shown in table.3.2.

1. Step 1 of the algorithm involves computing the equilibrium distribution function f_i^{eq} using macroscopic quantities as described in equation (3.22). In this step, the zeroth order of the equilibrium Hermite moment expresses pseudo pressure

$$a^{f^{eq},(0)} = \rho\theta = \frac{p}{c_s^2} = \frac{\rho r T}{c_s^2} \tag{3.38}$$

where θ is linked with temperature and the mass fractions (through r), which are available through the FD like solver in our hybrid method.

$$f_i^{eq} = \omega_i \left\{ \mathcal{H}^{(0)} \rho\theta + \frac{\mathcal{H}^{(1)}_{i\alpha}}{c_s^2} \rho u_\alpha + \frac{\mathcal{H}^{(2)}_{i\alpha\beta}}{2c_s^4} \left[\rho u_\alpha u_\beta\right] + \frac{\mathcal{H}^{(3)}_{i\alpha\beta\gamma}}{6c_s^6} \left[\rho u_\alpha u_\beta u_\gamma\right] \right\} \tag{3.39}$$

It is important to emphasize that this expression, where the zeroth order of the equilibrium function represents pseudo pressure, is distinct from the more conventional LBM where the zeroth order expresses density. This distinction is a key feature of our solver, hence its name, "Pressure Based."

2. Step 2 involves construction of the forcing term F_i to obtain a NS accurate viscous tensor, with the expansion containing only the second order:

$$F_i = \omega_i \left\{ \frac{\mathcal{H}^{(2)}_{i\alpha\beta}}{2c_s^4} a^{F,(2)}_{\alpha\beta} \right\} \tag{3.40}$$

For details regarding the Hermite moments, refer to [37].

3. Step 3 encompasses the computation of the non-equilibrium function using the Hybrid Recursive Regularized (HRR) collision model, as described by equations (3.36) and (3.37).

4. Step 4 involves the computation of the collision term f_i^{col} using equation (3.28).

5. Step 5 is the streaming step expressed by the equation (3.29)

6. Step 6 involves updating the macroscopic variables from the distributions, typically accomplished using equation (3.30) for orders $n = 0, 1, 2$. However, due to the modified zeroth-order moment of the equilibrium distribution function in the pressure-based method, to restore an accurate mass conservation equation, an essential adjustment to the zeroth-order update for obtaining updated density becomes necessary:

$$\rho(t + \Delta t, \boldsymbol{x}) = \rho(t, \boldsymbol{x}) + \left(\Pi^{\bar{f}(t+\Delta t, \boldsymbol{x}),(0)} - \Pi^{\bar{f}(t,\boldsymbol{x}),(0)} \right) \tag{3.41}$$

The updates for the first and second-order macroscopic variables remain unchanged, providing updated $(t + \Delta t)$ momentum density and the stress tensor, respectively.

Finally, incorporating the macroscopic quantities from our hybrid solver: (E, Y_k) and $(\rho, \boldsymbol{u})$, we can proceed with the subsequent iteration, starting with Step 1.

A complete algorithmic picture of our method is given in the figure 3.3. Note that as a part of Tayyab [104] thesis and several scientific articles, this method was already validated on canonical test cases such as: premixed and counter-flow diffusion flames [106], Darrieus-Landau instability in Hele-Shaw cell [105] and turbulent premixed burner (Volvo burner) [103].

3.4 Boundary Conditions

Having established our numerical solver, let us focus on the final aspect for ensuring the well-posedness of the Navier-Stokes (NS) system: defining appropriate Boundary Conditions (BC). In particular, let us look at the BCs that are useful for the investigation of thermoacoustic instabilities.

In the context of Lattice Boltzmann Method (LBM), there are various techniques for implementing boundary conditions, with notable methods including the Bounce-back method and the Wet-node approach. However, in the context of regularized models [48, 56], we have the option to directly apply standard Navier-Stokes boundary conditions (such as Dirichlet, Neumann, and Characteristic BC) on the macroscopic quantities and then reconstruct to the collision distribution function at the boundary nodes. Our solver adopts this approach, and the essential steps involved are as follows:

1. **Computing Macroscopic Values :** Compute the macroscopic variables at the boundary locations using the imposed Navier-Stokes-Fourier boundary conditions.

2. **Calculating Gradients :** Utilize finite difference schemes to estimate the gradients of the macroscopic variables at the boundary nodes for the forcing terms and the viscous tensor.

3. **Reconstructing Distributions :** Reconstruct the distribution function f_i^{col} at the boundary nodes.

In this thesis, we have employed a variety of conventional boundary conditions using this method, including periodic, isothermal and adiabatic walls and also slip and no-slip walls, adiabatic slip (symmetric) and no-slip walls, velocity inlet, and pressure outlet. These BCs are generally based on Dirichlet ($X = X_{imposed}$) and Neumann ($\frac{\partial X}{\partial n} = f(x)$ with $f(x) = 0$) boundary conditions [104]. In case of heat losses, a BC

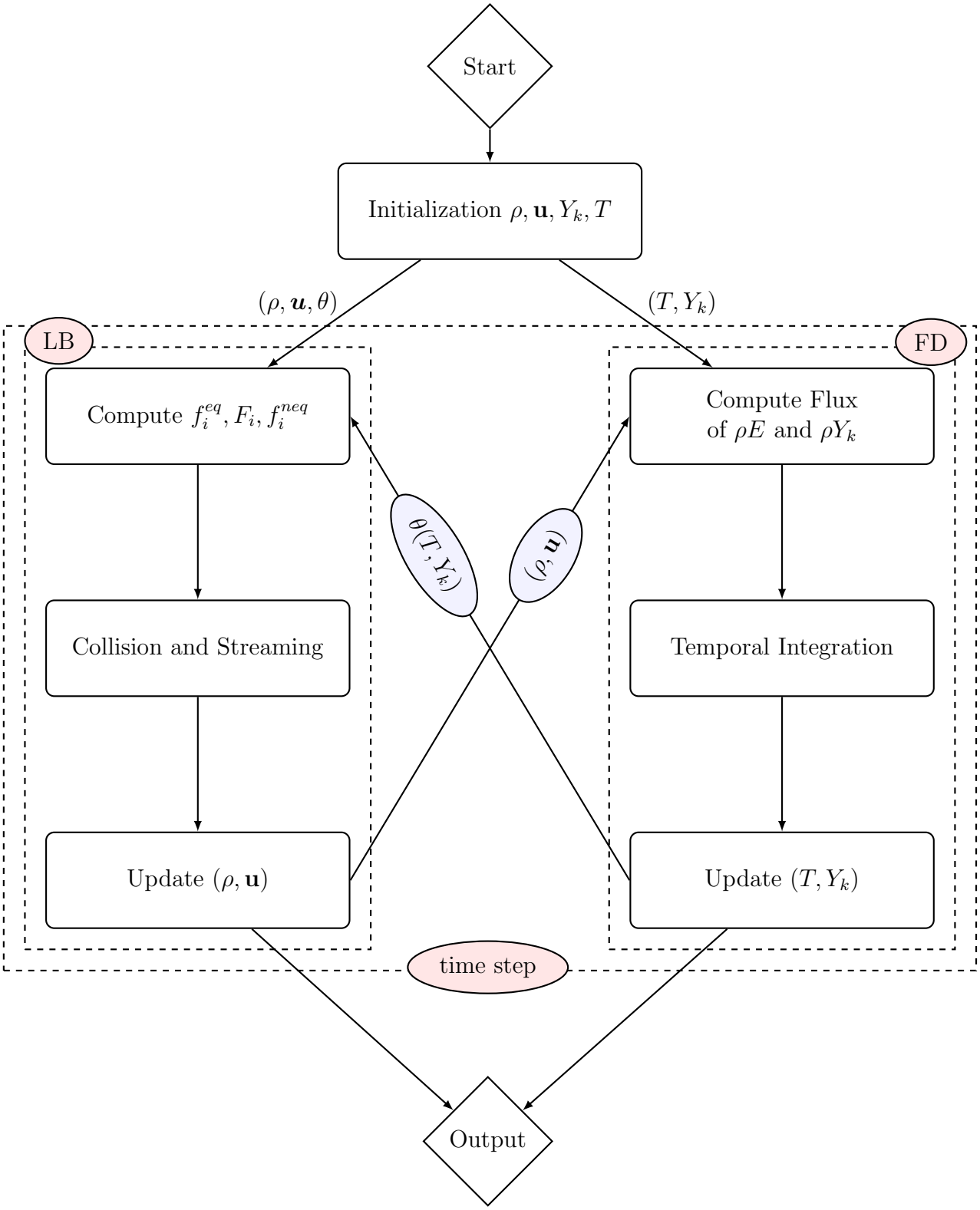

Figure 3.3: Illustration of the Hybrid Lattice Boltzmann algorithm.

based on linearized heat transfer between the fluid and the wall, and wall and the ambient atmosphere was implemented and is provided in section 6.6.

However, for compressible flows, such as those encountered in the study of thermoacoustic instabilities, specialized boundary conditions are essential. These boundary conditions must be capable of simulating diverse acoustic impedance at the inlets and outlets. To meet this requirement, we have adopted the approach outlined by Poinsot and Lele [82], which involves formulating boundary conditions based on the characteristic waves.

Specifically, for the non-reflecting outlet, we have implemented a "subsonic Non-reflecting outflow BC", wherein the pressure is imposed at infinity p_∞ [82]. Concerning the inlet, which requires the ability to introduce acoustic waves while ensuring complete non-reflection, we have followed the more refined iteration of the NSCBC inlet approach introduced by Daviller et al. [27].

Given the importance of this inlet boundary condition in our investigation of thermoacoustic instabilities, we provide a more comprehensive explanation of its specifics in the following section.

3.4.1 NRI-NSCBC

When employing non-reflecting inlet boundary conditions, it is widely acknowledged [84, 108] that a compromise must be sought between the desired unsteady inlet velocities and the non-reflective characteristics of the inlet itself. However, when investigating the influence of acoustic waves on the flame, as in the case of study of parametric instability of flames or the Flame Transfer Function (FTF), the precision of both factors becomes essential. In this regard, the new formulation presented in [27] proves to be highly advantageous. It enables us to achieve the necessary accuracy in reconciling the unsteady target inlet velocities quickly, with the non-reflecting characteristics of the inlet boundary still intact.

It is well established that to enforce a characteristic wave-based BC for a three-dimensional subsonic inlet involving reacting flows, a set of 4+N conditions must be imposed to ensure well-posedness [82]. These conditions, denoted as $\mathcal{L}_2, \mathcal{L}_3, \mathcal{L}_4, \mathcal{L}_5$, and $\mathcal{L}_{5+N}$, are associated with the amplitudes of incoming characteristic waves. Additionally, the outgoing characteristic wave $\mathcal{L}_1$ can be computed from the one-sided derivative within the computation. Utilizing LODI approach [82] and assuming isentropic inlet where the entropy wave $\mathcal{L}_2$ is set to zero (a simplification which can be lifted quite easily), we can achieve a non-reflecting inlet by expressing the ingoing acoustic wave $\mathcal{L}_5$ as:

$$\mathcal{L}_5 = \rho c \left(-2\frac{\partial u^t}{\partial t} + 2K\left(u - u^t\right) \right) \tag{3.42}$$

The two transverse waves can then be written as:

$$\mathcal{L}_3 = -\frac{\partial v^t}{\partial t} + 2K\left(v - v^t\right) \quad \text{and} \quad \mathcal{L}_4 = -\frac{\partial w^t}{\partial t} + 2K\left(w - w^t\right) \tag{3.43}$$

Here, u^t, v^t, and w^t represent the target velocities that are imposed. The term $K\left(u_\alpha - {u_\alpha}^t\right)$ is known as the "relaxation" term, added to the Navier-Stokes Characteristic Boundary Conditions (NSCBC) to prevent the drift of mean velocities. It effectively guides the instantaneous velocity u_α towards u_α^t with a relaxation time $1/K$. The proper scaling of the relaxation coefficient can be achieved through the non-dimensional parameter $\sigma_k = KL/c$, where L represents the characteristic length of the domain and c denotes the sound speed.

Daviller et al. [27], based on [84, 108], introduce a further refinement. In addition to expressing the normal target velocity u^t as a combination of the target mean velocity $\bar{u}$ and the target unsteady velocity u_a^t (acoustical velocity in our context), they introduce an additional term u_- to account for the velocity fluctuations induced at the inlet due to the outgoing wave $u - c$. This term u_- can be computed locally at each point along the inlet patch by integrating the amplitude of the outgoing acoustic wave $\mathcal{L}_1$ over time as:

$$u_- = \frac{1}{2\rho c}\int_0^t \mathcal{L}_1 dt \tag{3.44}$$

In practice, to ensure the accuracy of simulations, it is crucial to apply a high-pass filter to the above equation. In the end, the modified expression for $\mathcal{L}_5$ becomes:

$$\frac{\mathcal{L}_5}{\rho c} = -2\frac{\partial u_a^t}{\partial t} + 2K\left[u - \left(\bar{u} + u_a^t + u_-\right)\right] \tag{3.45}$$

This formulation enables us to precisely impose acoustic waves u_a^t, while maintaining non-reflecting characteristics and preventing velocity drift.

3.5 Summary

In this chapter, we introduced the fundamentals of the Lattice Boltzmann Method (LBM). We began by exploring the Boltzmann Equation and subsequently derived LBM from it. We also provided an overview of the D3Q19 lattice, which plays a central role in our work. Additionally, we presented the standard LBM algorithm, emphasizing

the significance of the streaming and collision steps in making LBM computationally efficient.

Furthermore, we delved into the specific enhancements required for simulating reactive flows using LBM. This included the introduction of our Hybrid solver, which integrates Finite Difference (FD)-like methods for energy and species transport. We discussed the Hybrid Regularized Recursive Collision model [48] and Pressure-based equilibrium functions [36] as crucial components for achieving stable results in simulations of compressible reactive flows.

To complete the picture, we provided insights into the incorporation of boundary conditions into our model. Notably, owing to its significance in our investigation of flame-acoustic interactions, we also provided a comprehensive explanation of the Non-Reflecting Inlet - Navier Stokes Characteristic Boundary Condition (NRI-NSCBC) [27].

Chapter 4

LBM for Premixed Laminar Flame Instabilities

Contents

4.1 Introduction 64

4.2 Preliminary numerical definitions 66

4.3 Darrieus-Landau Instability 66

4.3.1 Impact of Boundary Conditions on the Cut-off Wavelength . 67

4.3.2 Symmetric and non-symmetric flames in a channel 69

4.4 Acoustically forced flames 72

4.4.1 Parametric instability of freely propagating flames 72

4.5 Self-excited flames in narrow channels 75

4.5.1 Eigenmode analysis 76

4.5.2 Parametric studies on the gain of instability 78

4.5.3 Flame dynamics in long-narrow channels 82

4.6 Conclusion 88

4.1 Introduction

Since its inception, the Lattice Boltzmann Method (LBM) [16] has found extensive applications in the field of isothermal external aerodynamics and aeroacoustics [95]. The success of this method is primarily attributed to the "Stream and Collide" algorithm,

which operates on a Cartesian grid and only requires interactions with nearest neighbors. This architecture provides LBM with excellent dissipation characteristics [64], all while maintaining a relatively low computational burden [60]. In line with this, the compressible Hybrid LB method [36], specifically tailored for reactive flows [105, 106], has demonstrated its cost-effective capabilities. Notably, validating this method on a combustion DNS benchmark, highlighted its computational efficiency, indicating that the CPU cost of a compressible reactive flow simulation rivals that of classical Navier-Stokes solvers employing low-Mach number approximation [10].

Given the well-established success of LB methods in aeroacoustics [14, 52], and their emerging potential in combustion [10], it becomes pertinent to investigate their capacity to address thermoacoustic instabilities. This exploration serves as the cornerstone of this chapter.

Our primary focus lies in simulating the complex behavior of flames propagating inside a tube (2D channels in our study) [50, 65, 81, 93]. In the absence of acoustics, flames propagating in these channels exhibit only the hydrodynamic Darrieus-Landau (DL) instability [88, 105]. However, introducing acoustics adds layers of complexity: "a bidirectional feedback loop where the flame generates and influences acoustics, and the resultant acoustics, in turn, affect the flame, possibly instigating thermoacoustic instabilities" – is developed. This interplay, with its spectrum of involved acoustics and implicitly dependent flame dynamics, presents a formidable challenge for the numerical solvers.

Given this context, this chapter aims to evaluate the capability of the Lattice Boltzmann Method in accurately simulating flame-acoustic interactions. Our systematic approach consists of three main objectives:

- Validate the ability of the LB method to accurately simulate the flame response to external acoustic excitation.
- Validate the correspondence between the generated thermoacoustic instability and the intrinsic eigenmodes of the channel.
- Cross-validate our findings with existing literature and numerical simulations.

Beyond these primary goals, we will also explore the impact of variations in boundary conditions, flame shapes, and channel dimensions on channel-bound thermoacoustic instabilities to further enrich our understanding of this complex phenomenon.

4.2 Preliminary numerical definitions

In this section, we will introduce new definitions and quantities used in this chapter for the sake of clarity and comprehensibility.

Following Eq. (1.29), the consumption speed (S_c) of a flame propagating within a channel along the x direction can be expressed as:

$$S_c = -\frac{1}{\rho_f Y_F^f D} \int_0^W \int_0^H \dot{\omega}_F \, dydz \tag{4.1}$$

In the equation above, $D = n_y \times n_z \times \Delta x^2$ is the cross-section area of the channel. The terms W and H correspond to the width and height of the domain in the y and z coordinates, respectively. And throughout this chapter, we normalize the consumption speed S_c with S_l, and the dimensions of the channel are consistently normalized using the diffusive flame thickness, δ_D, described by Eq.(1.30).

Furthermore, the position x_f of the propagating flame in two-dimensional channels examined in this research is determined by integrating the normalized temperature, $\theta(T)$, across the channel volume V:

$$x_f = \frac{1}{V} \int \theta(T) dV. \tag{4.2}$$

The orientation is set such that $x_f = 0$ when the tube is permeated with fresh gas and $x_f = 1$ when it is filled with burnt gas.

Lastly, all simulations within this chapter employ a spatial discretization of $\Delta x \approx \delta_T/13$, around 13 points per thermal flame thickness, δ_T. Past studies have demonstrated that this is adequate for precise flame resolution when utilizing a single-step chemistry [105, 106]. The time-step (Δt) adheres to a maximum Courant–Friedrichs–Lewy number (CFL) of 0.6.

4.3 Darrieus-Landau Instability

As outlined in section 2.2.1, flames, whether planar or perturbed, that exceed the DL cut-off wavelength λ_c ($\frac{2\pi}{k_c}$) are vulnerable to Darrieus-Landau (DL) instability [26, 55]. While many theoretical analyses on these cut-off numbers have been performed under the assumption of a periodic domain [19, 68], in this section, we focus on understanding the impact of boundary constraints on the DL cut-off wavelengths. We also aim to

explore the different behaviors that arise during propagation within these bounded channels.

We commence our analysis by considering a freely propagating flame confined within a channel of width W and length L. To efficiently identify the cut-off wavelength (λ_c), we subject the flame to an inherent perturbation with a wavelength $\lambda = W$. In specific numerical terms, this perturbed flame configuration is achieved by utilizing the solution of a fully developed 1D flame, denoted as X_{1D}, where X includes variables such as T, ρ, and Y_k. To adapt this 1D solution to our 2D framework, we specify these variables in 2D domain as $X(x, y, t = 0) = X_{1D}(y - f(x))$. Here, $f(x)$ represents the intended geometric perturbation, which in our study takes the form of a sinusoidal wave [104, 106]. Additionally, to avoid any external influence, non-reflecting boundary conditions are applied on both ends of the channel. The comprehensive details regarding the thermo-chemical parameters used for this section are given in appendix (Tab A.1)

4.3.1 Impact of Boundary Conditions on the Cut-off Wavelength

The influence of boundary constraints on the cut-off wavelength (λ_c) is explored by enforcing various boundary conditions along the width W. Specifically, the following boundary conditions are investigated:

- **Periodic conditions:** Figure. 4.1 demonstrates the growth or decay of the initial perturbation depending on its wavelength (i.e., the domain width). When the wavelength (λ) of the perturbation is less than or equal to $40\delta_D$, the disturbance rapidly diminishes, resulting in a planar flame. However, when λ equals $43\delta_D$, the amplitude of the perturbation grows significantly due to instability. This observation suggests that the DL cut-off wavelength (λ_c) for the periodic boundary condition falls within the range of $40 - 43\delta_D$.

$$\boxed{40\delta_D < \lambda_c \leq 43\delta_D}$$

- **Slip adiabatic walls (or symmetry boundary condition):** Similar investigations are conducted regarding flame propagation within the slip adiabatic walls. Figure. 4.2 illustrates the results, depicting:

$$\boxed{22.5\delta_D < \lambda_c \leq 25\delta_D}$$

Furthermore, by comparing the λ_c values obtained under periodic and slip boundary conditions, it can be deduced that the cut-off wavelength is "approximately" halved when using slip boundary conditions. This result is rather intuitive: an adiabatic slip wall is equivalent to a symmetry condition, so the pattern observed with periodic conditions can be reproduced with half the width and then mirrored to obtain the periodic case.

- **Non-slip adiabatic walls:** Next, we explore the influence of non-slip adiabatic walls. As illustrated by the fig. 4.3, the cut-off wavelength lies between:

$$\boxed{17.5\delta_D < \lambda_c \leq 19\delta_D}$$

An interesting observation is that even when $W = 17.5\delta_D$, which falls below the cut-off wavelength, the flame exhibits a deviation from a strictly planar shape. This deviation is primarily attributed to the imposition of a no-slip condition ($\boldsymbol{u} = 0$) at the walls. This condition significantly alters the flow field, leading to the establishment of a Poiseuille velocity profile. Consequently, the flame front does not remain perfectly planar, even when $W < \lambda_c$. Consequently, the consumption speed S_c slightly surpasses that of a planar flame (S_l). This observation hints at a potential explanation for why the cut-off wavelength is lower when non-slip adiabatic walls are employed in comparison to slip-walls.

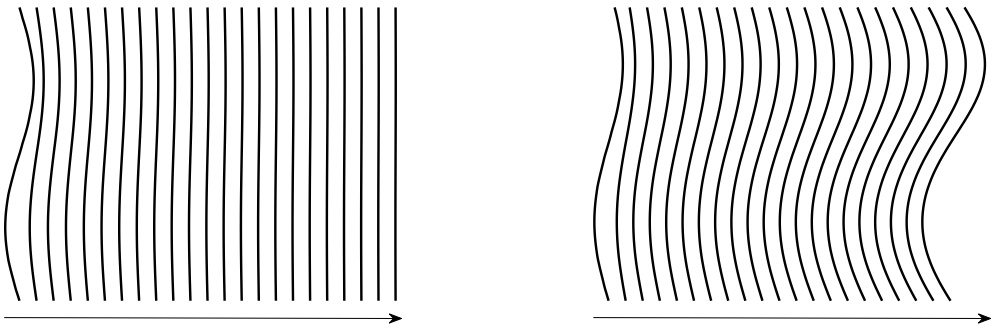

(a) $\lambda = 40\,\delta_D < \lambda_c$ (b) $\lambda = 43\,\delta_D \geq \lambda_c$

Figure 4.1: Growth/decay of DL instability in periodic domain. (Flame propagates from left to right): **(*a*)** Instability decay at below cut-off wavelength. **(*b*)** Instability growth above cut-off wavelength

Lastly, fig. 4.4, depicts the normalized flame consumption speed (S_c) for slip and non-slip, adiabatic walls. It is evident that for $W < \lambda_c$, the consumption speed is

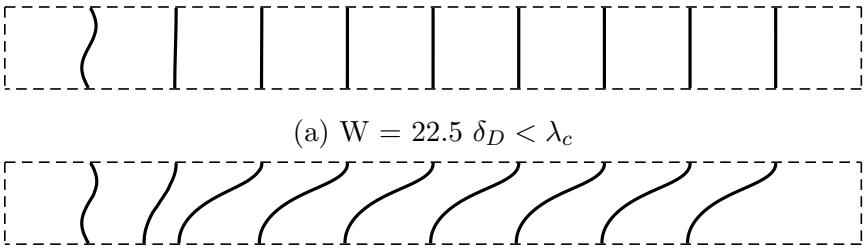

(a) W = 22.5 $\delta_D < \lambda_c$

(b) W = 25 $\delta_D \geq \lambda_c$

Figure 4.2: Growth/Decay of DL instability in between slip walls. Flame shapes are depicted by the iso-contours of temperature (1500K) (propagating left to right) **(*a*)** Instability decay below cut-off wavelength. **(*b*)** Instability growth above cut-off wavelength.

approximately equal to the laminar flame speed (S_l) in the case of slip walls, and slightly higher but still in proximity to S_l in the case of non-slip walls. However, once the Darrieus-Landau instability sets in at $W \geq \lambda_c$, the flame consumption speed (equivalent to the flame surface area) increases notably. The increase is particularly significant in the non-slip walls.

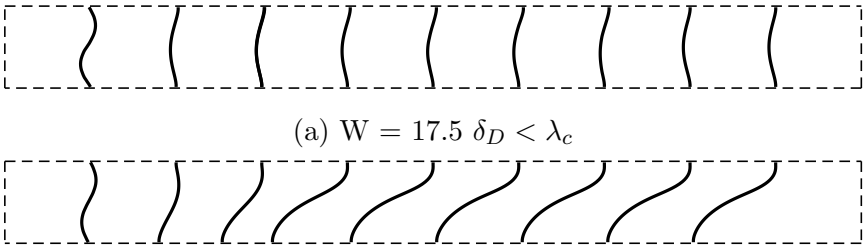

(a) W = 17.5 $\delta_D < \lambda_c$

(b) W = 19 $\delta_D \geq \lambda_c$

Figure 4.3: Growth/Decay of DL instability in between non-slip walls. Flame shapes are depicted by the iso-contours of temperature (1500K) (propagating left to right) **(*a*)** Instability decay below cut-off wavelength. **(*b*)** Instability growth above cut-off wavelength.

4.3.2 Symmetric and non-symmetric flames in a channel

In the previous section, we observed that both in slip and non-slip channels, once the width of the channel exceeds the Darrieus-Landau cut-off wavelength (λ_c), the initially perturbed sinusoidal flame undergoes a significant transformation in curvature. This transition is direct, leading the flame from a sinusoidal to a "non-symmetric" shape. However, if the flame is initially configured as planar, it first evolves into a "symmetric" state with a hump pointing towards the burnt gases. After a certain propagation time, it

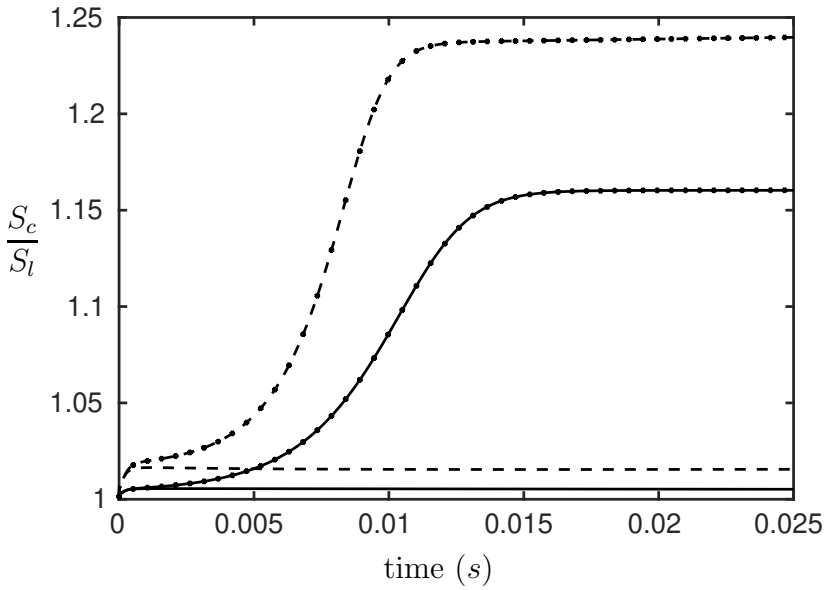

Figure 4.4: Normalized flame consumption speed S_c in slip (solid) and non-slip (dash) walls. A marker on the line denotes $W \geq \lambda_c$.

subsequently shifts to the non-symmetric flame shape. This phenomenon aligns with the findings reported in [29], which suggests that in narrow channels, flames propagating within them can exhibit two feasible solutions: symmetric and non-symmetric flame shapes. Nevertheless, after a certain propagation time, the flame consistently adopts the more stable non-symmetric solution.

Figure. 4.5 depicts these two flame solutions. It can be observed that the "planar-symmetric-non-symmetric flame" (**A**) ultimately possesses the same consumption speed (flame surface area and curvature) as the "sinusoidal-non-symmetric flame" (**B**). Although the flame ultimately selects the non-symmetric solution, the distinction between the two due to the initialization is crucial for numerical studies, as the response of acoustics to both symmetric and non-symmetric flames is entirely different [50].

The above investigations regarding the transitioning flame shapes (solutions) were conducted within the non-slip adiabatic walls, along with the utilization of acoustically non-reflecting boundaries at the ends of the channel. Remarkably, it was observed that, regardless of whether non-reflecting or reflecting boundaries were employed, the transition from a symmetric to a non-symmetric flame consistently occurred at the same flame propagation distance for channels of the same width. This phenomenon is further illustrated in fig. 4.11, where even in the presence of thermoacoustic effects due to the reflecting boundaries, the transition still occurs at the same time.

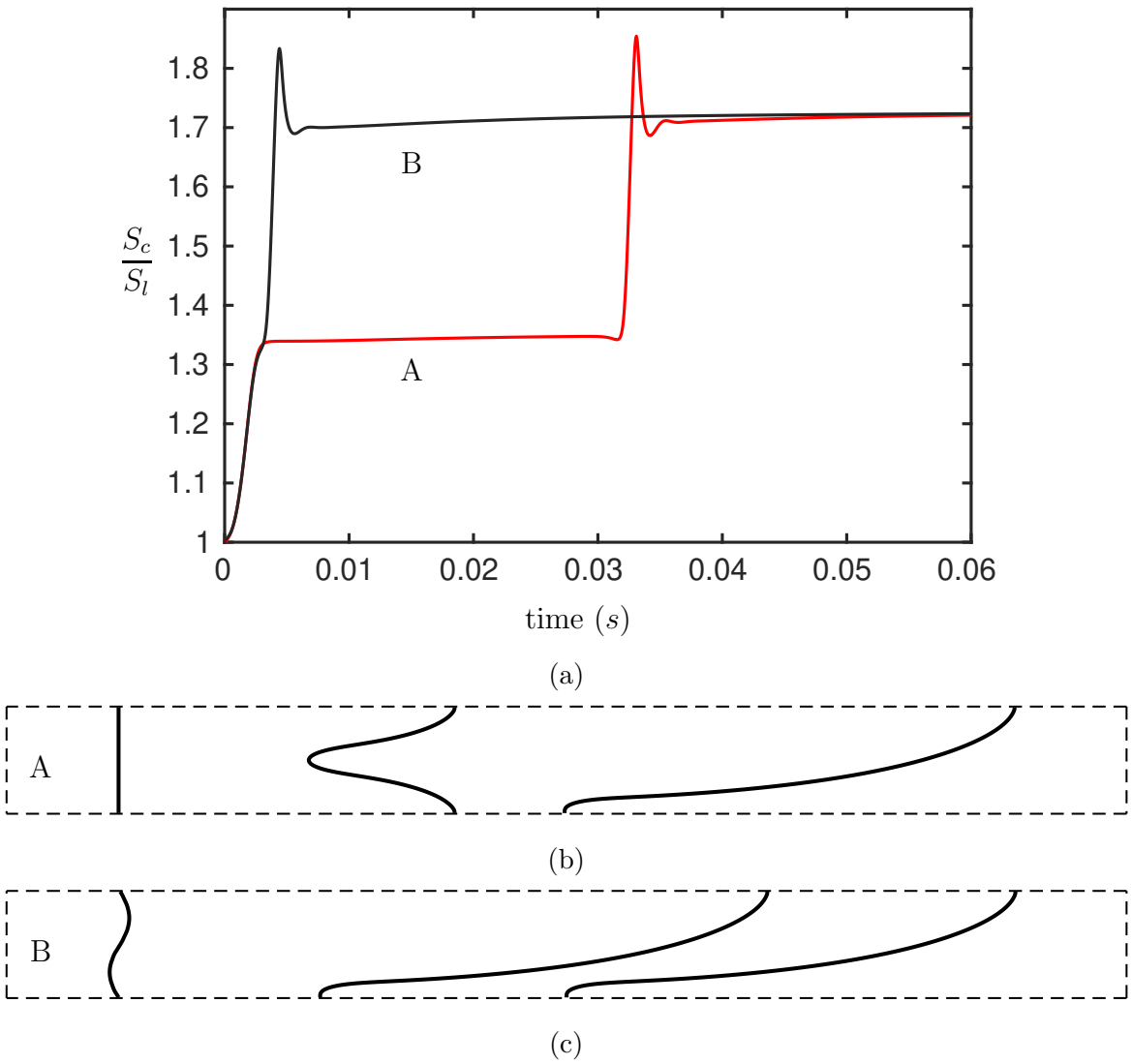

Figure 4.5: Illustration of flame shape transition in a channel of length ($L = 1200\,\delta_D$) and width ($W = 40\,\delta_D$) from initially planar (**A**) and initially perturbed (**B**) configurations: ***(a)*** Flame consumption speed for (**A**) in red and (**B**) in black.
(b) Flame shape transition from planar to symmetric and then non-symmetric (**A**).
(c) Flame shape transition from perturbed to non-symmetric directly (**B**).

After examining the influence of different boundary conditions on the Darrieus-Landau cut-off wavelength and providing a preliminary demonstration of the capability of LBM to capture the Darrieus-Landau instability in freely propagating flames (for detailed demonstration, refer to [105]), we now turn our attention to the primary objective: highlighting the ability of LBM to accurately model the interaction between acoustic waves and flame dynamics and ultimately resolve a thermoacoustic instability.

4.4 Acoustically forced flames

Before addressing the complete problem of self-excited thermoacoustic instability issues, it is crucial to first validate the capability of the Lattice Boltzmann Method in accurately capturing the response of the flame to externally imposed acoustic waves. This validation process entails injecting acoustic waves onto a DL instability-prone flame ($\lambda \geq \lambda_c$). And as elucidated in Section 2.3.1, the flame exhibits various responses, including primary instability, planar flames, and secondary instability, depending on the intensity of the acoustic waves [30, 94].

4.4.1 Parametric instability of freely propagating flames

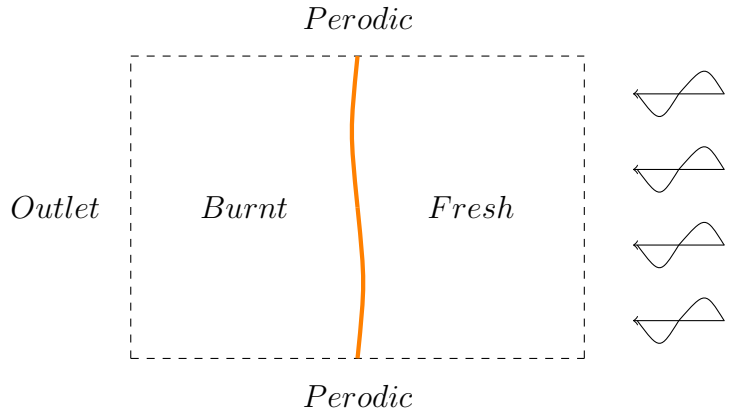

Figure 4.6: Sketch of the periodic domain used in the study of externally excited flames.

We commence this analysis by considering a stationary, single wave-perturbed flame within a 2D periodic domain ($\lambda = W > \lambda_c$), the schematics are provided in the figure 4.6. Unlike the previously discussed freely propagating flame configurations, this flame remains fixed at the center of the domain. To minimize undesirable reflections within the domain, we apply non-reflecting outlet conditions towards the exit of burnt gases. And we introduce acoustic waves using the NRI-NSCBC boundary formulation

at the inlet (section 3.4.1). These imposed planar harmonic acoustic waves possess wavelengths significantly greater than the thermal flame thickness (δ_T), and the imposed velocity fluctuation is represented as $u_a^t = A_0 \sin(2\pi f t)$, where A_0 denotes the fluctuation amplitude, and f corresponds to the frequency of the sinusoidal fluctuation. The simulation parameters utilized for this analysis are detailed in the appendix (A.2).

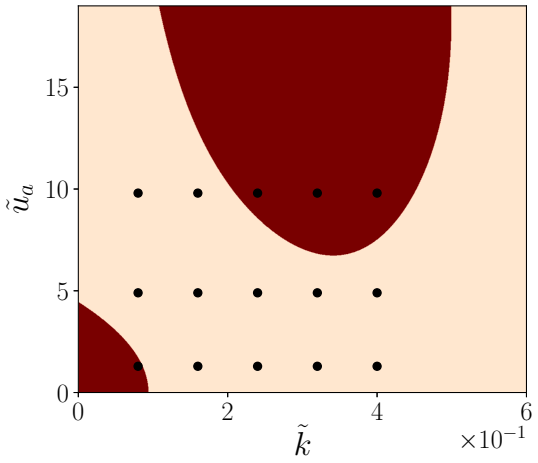

Figure 4.7: Stability diagram for parametrically excited flames showing distinct regions based on the reduced acoustic amplitude $\tilde{u_a}$ and reduced wavenumber $\tilde{k}$.

Figure 4.7 resemblances the idealized thermoacoustic stability diagram portrayed in Figure 2.5. This diagram identifies distinct regions based on the reduced acoustic amplitude $\tilde{u_a}$ and reduced wavenumber $\tilde{k}$. The lower red region pertains to primary (**I**) instability, while the upper red region corresponds to secondary (**II**) instability. The boundaries of these regions are dictated by the parameters of the chosen chemistry (Tab A.2) and the imposed frequency of the acoustic wave. The value of the black dots along the y-axis signify the intensities of acoustic velocity fluctuations chosen within each region; they serve as a validation metric for assessing the accuracy of LBM in representing the flame response to externally induced acoustic waves. The values along the x-axis correspond to multiples of the initially perturbed wavenumber $\tilde{k} = 2\pi\delta_D/\lambda$. Furthermore, the reduced acoustic amplitude is given by $\tilde{u_a} = u_{rms}/S_l$, where u_{rms} is the root mean square (rms) of the acoustic axial velocity measured at the flame position.

Figure. 4.8 illustrates the evolution of the flame front in an externally excited acoustic field, with iso-contours of the progress variable based on temperature ($\theta(T) = 0.6$) chosen to depict the flame front. The flame fronts are plotted at every period of the externally excited acoustic wave, evolving from left to right.

As previously mentioned, for a chosen wavenumber $\tilde{k} < \tilde{k_c}$ (here $\tilde{k} = 0.08$), the amplitude of the perturbation on the flame front grows in the absence of acoustics

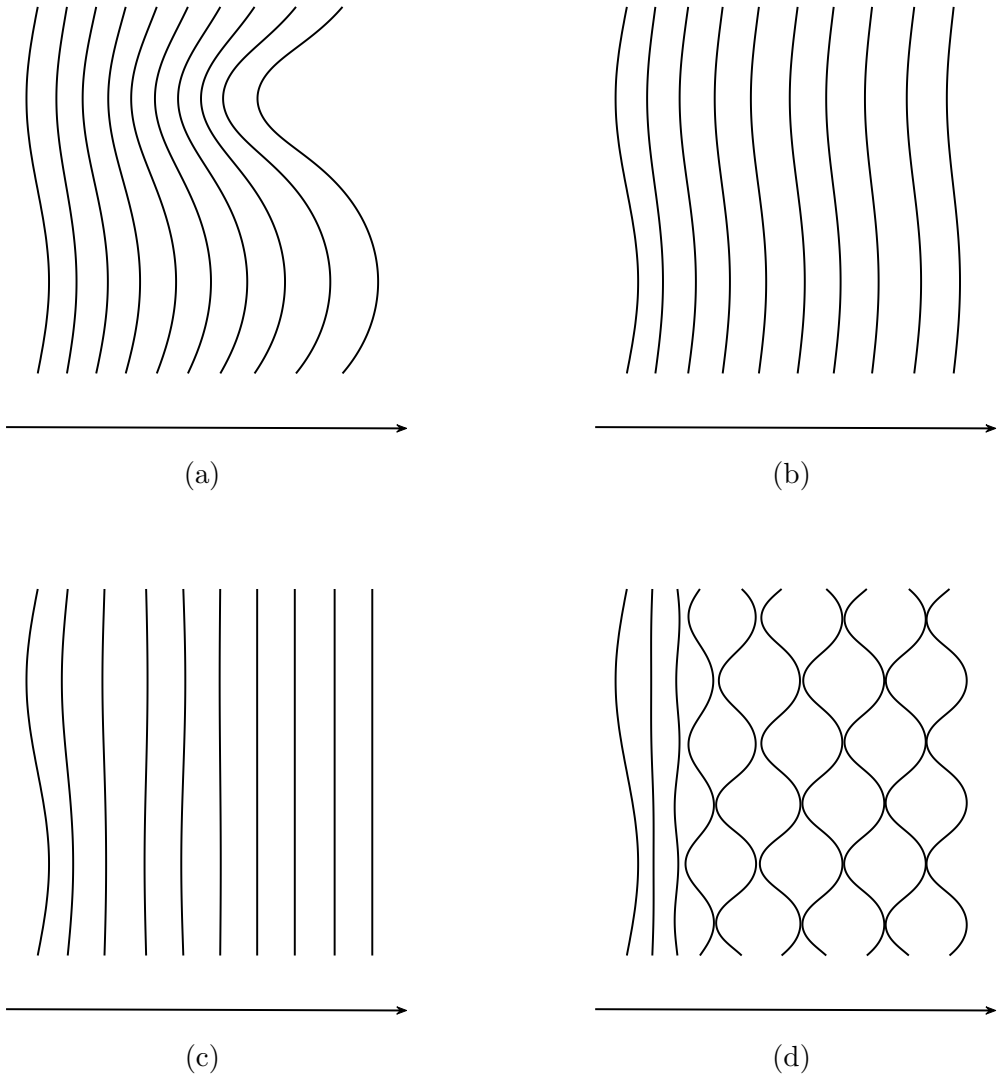

Figure 4.8: Iso-contours of the progress variable $\theta(T) = 0.6$ are plotted from left to right at every period of the externally excited acoustic wave (10^{-3} s) in different regions of Fig. 4.7. ***(a)*** Shows the growth of DL instability without any acoustics. ***(b)*** Depicts the reduction of DL instability amplitude by low-amplitude acoustic forcing ($\tilde{u_a} = 1.36$). ***(c)*** Illustrates a stable planar flame obtained by moderate amplitude acoustic forcing ($\tilde{u_a} = 5.15$). ***(d)*** Shows parametric instability due to high amplitude acoustic forcing ($\tilde{u_a} = 10.23$).

due to the DL instability (see Fig. 4.8a). However, the exact same initially perturbed flame front in the presence of imposed acoustics behaves differently. In practice, it was observed that the flame always chooses the an unstable wavenumber from the stability diagram:

- Imposing low-amplitude acoustics ($\tilde{u_a} = 1.36$) reduces the amplitude of DL growth compared to the case without acoustics, as shown in Fig. 4.8b.
- When applying a moderate acoustic amplitude ($\tilde{u_a} = 5.15$), the flame becomes and remains planar after some time, as depicted by Fig.4.8c, because all corresponding wavenumbers are in the stable region (Fig.4.7).
- Increasing the reduced amplitude further ($\tilde{u_a} = 10.23$) causes the wavenumber of the flame front to switch to an unstable harmonic (in this case, the third one), as evidenced by Fig. 4.8d. Here, iso-contours of temperature plotted at each acoustic period illustrate a fundamental characteristic of parametric instabilities: formation of cellular structures that change sign at every acoustic period.

This analysis clearly demonstrates the capability of LBM to accurately capture the flame response to varying intensities of the acoustic wave. Although not exhaustive, the qualitative response of a conical flame to different frequencies of the imposed acoustic waves was also depicted in Figure 2.6. These two results provide comprehensive validation of ability of LBM to correctly simulate acoustic $\rightarrow$ flame interaction.

4.5 Self-excited flames in narrow channels

After validating the canonical response of the flame front to external acoustic perturbations, we proceed with the investigation of self-excited thermoacoustic instabilities. These instabilities occur when the acoustics are directly triggered by the flame itself, sometimes leading to severe instabilities in combustion chambers [92].

In the subsequent analysis, we focus on thermoacoustic instabilities within a narrow channel, as illustrated in figure. 4.9. The flame is initialized with a 1D laminar flame profile positioned at $x_f = 0.1$, and the right side of the domain is filled with fresh gases to facilitate free flame propagation. The geometrical perturbation $f(x)$ and the top-bottom walls are chosen based on the specific objectives of the test case and will be explicitly stated. At the outlet boundary, atmospheric pressure is imposed, allowing only for the exit of burnt gases, while a non-slip adiabatic wall is employed on the right

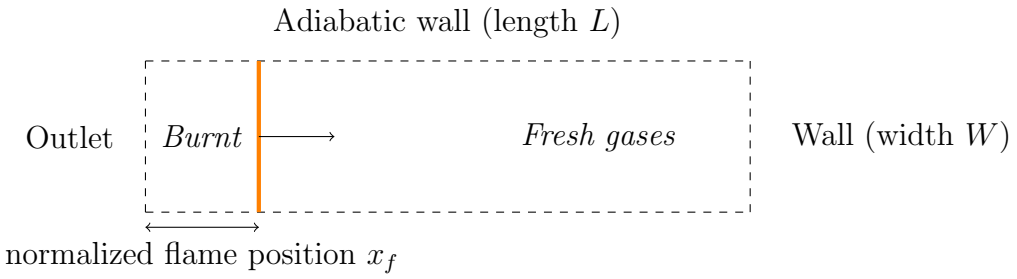

Figure 4.9: A sketch of the narrow channel under consideration.

end. These boundary conditions confine the acoustics within the domain, potentially leading to the growth of instabilities.

The thermo-chemical parameters used throughout the rest of this chapter are provided in detail in the appendix (Tab A.1 and A.3). However it is worth mentioning that a Flame Thickening Model ([21]) with a factor 4.7 was employed to increase the flame thickness while preserving the flame speed.

In the following sub-sections, we will perform a number of numerical simulations to successively: (i) Confirm the correspondence of the self-excited instability with the natural eigenfrequency of the channel. (ii) Provide insights on the nature of thermoacoustic instability based on the channel dimensions and flame shapes. (iii) Strive to achieve the phenomenon of self-stabilization of DL instability in the longer channels.

4.5.1 Eigenmode analysis

The analytical formula for determining the natural eigenmode frequency (f) of the channel in the presence of a thin flame ($\delta_T \ll L$) was derived in Eq.(2.44). By neglecting the effects of heat release and assuming the flame as a thin discontinuity that separates fresh and burnt conditions ($n = 0$), we can simplify Eq.(2.44) and obtain the eigenmodes of the channel easily. These analytical results can then be compared with the period/frequency of the thermoacoustic instability obtained through the Lattice Boltzmann Method to confirm its capability in correctly establishing the correspondence between the thermoacoustic instability and the changing of eigenmodes of the channel.

To perform this analysis, we will replicate the configuration presented in Figure 4.5, specifically, case B. However, in this analysis, we will employ a fixed pressure outlet set to $p = 1$ atm coupled with a solid wall at the opposite end to confine the acoustics within the channel.

Figure 4.10a illustrates the evolution of the consumption speed and pressure at

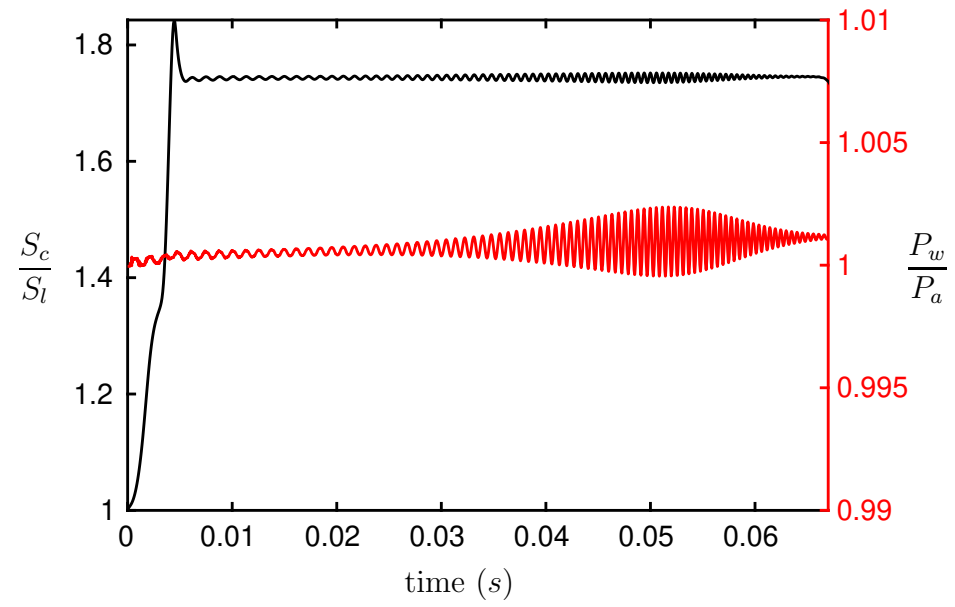

(a)

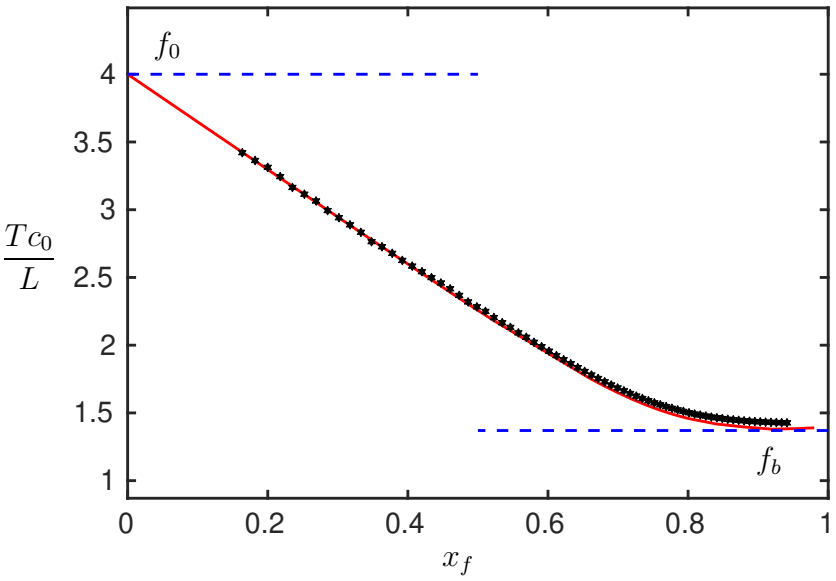

(b)

Figure 4.10: Thermoacoustics within a channel characterized by a length of $L = 1200\,\delta_T$ and width of $W = 40\,\delta_T$: ***(a)*** Illustrates the flame consumption speed, denoted by S_c/S_l (in black), and the pressure at the closed end, represented by P_w/P_a (in red). ***(b)*** Shows the correspondence between the period of oscillations (T) for a flame propagating from $x_f = 0$ to $x_f = 1$ (in black) and the eigenmodes of the channel determined using Eq. (2.44) (in red). Additionally, the top and bottom dashed blue lines represent the quarter-wave values for fresh (f_0) and burnt (f_b) conditions, respectively.

the closed end. The mean consumption speed history shows that the flame becomes non-symmetric immediately, consistent with case B in Figure 4.5. Subsequently, both the consumption speed and pressure at the wall exhibit oscillations, with the most significant oscillations occurring in the second half of the channel.

The period of oscillations of both the pressure fluctuation and the consumption speed, as well as the eigenmodes of the channel described by equation (2.44), can be compared at different flame positions, x_f. Figure 4.10b illustrates this comparison, with the numerical period obtained through the LBM method shown as black dots and the analytical formula depicted as a solid red line. This comparison reveals a remarkable similarity between the two. And as expected, the period decreases from the quarter-wave value observed with fresh gases to the value obtained when using burnt gases, as the channel gases become fully burnt ($x_f = 1$).

4.5.2 Parametric studies on the gain of instability

Having verified that the observed instability in the previous section corresponds to the anticipated quarter-wave eigenmode of the channel, we now shift our focus towards studying the influence of channel dimensions (length (L) and width (W)) and the flame shapes (symmetric and non-symmetric).

Flame shape and channel length: Studies by Jiménez et al. [50] revealed a significant influence of both flame shape and eigenfrequency (channel length) on the amplification of instabilities within the channel. Based on those insights, our initial objective is to replicate the results to validate the consistency and reliability of our LB numerical method. Subsequently, we expand the investigation to explore the impact of channel width on the amplification of thermoacoustic instabilities.

They [50] found that symmetric flames exhibit higher levels of instability at higher frequencies, while non-symmetric flames are more responsive to lower frequencies. Given that the excitation frequency corresponds to the quarter-wave mode, this effect can readily be studied by varying the channel length.

Figure. 4.11 reports consumption speed histories in four configurations:

1. Short channel ($L = 800\delta_D$): planar-symmetric-non-symmetric flame (case A of Fig. 4.11a)
2. Short channel ($L = 800\delta_D$): perturbed-non-symmetric flame (case B of Fig. 4.11a)
3. Long channel ($L = 2400\delta_D$): planar-symmetric-non-symmetric flame (case A of Fig. 4.11b)

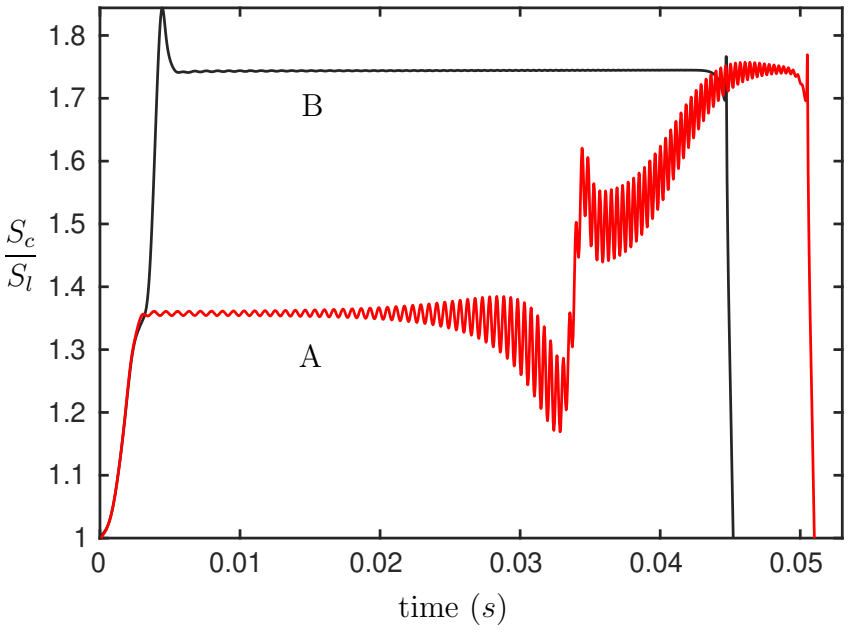

(a)

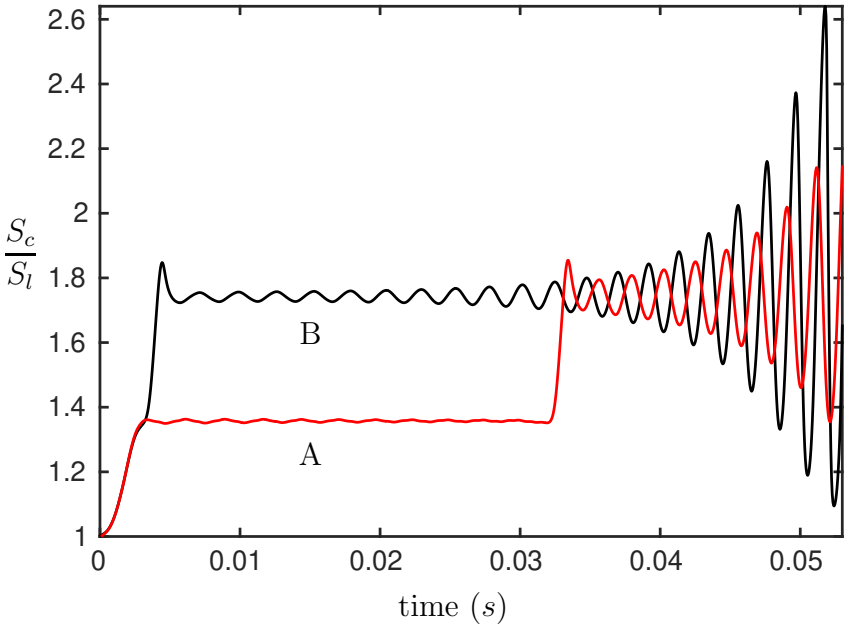

(b)

Figure 4.11: Flame consumption speed depicting the response of instabilities in case of initially planar (**A**) and initially perturbed (**B**) flames, in a channel of width $W = 40\delta_D$: ***(a)*** Greater amplitude instabilities seen on symmetric flame (**A**) for shorter length channel ($L = 800\delta_D$); ***(b)*** Greater amplitude instabilities seen on non-symmetric flame (**B**) for longer length channel. ($L = 2400\delta_D$)

4. Long channel ($L = 2400\delta_D$): perturbed-non-symmetric flame (case B of Fig. 4.11b)

In the shorter channel, as depicted in Figure 4.11a, it becomes evident that the symmetric flame (curve A) exhibits a higher susceptibility to thermo-acoustic instability, whereas the non-symmetric flame shows very limited response in such a short channel. However, when the eigenfrequency is divided by 3 for a channel that is three times longer, as shown in Figure 4.11b, the dynamics shift dramatically. In this scenario, the non-symmetric flame (B) becomes highly unstable, while the symmetric flame (A) merely displays damped oscillations. It's worth noting that as case A transitions from a symmetric to a non-symmetric flame, the instability emerges. In essence, non-symmetric flames display more pronounced responses at lower frequencies, while symmetric flames exhibit greater amplitude oscillations in higher-frequency regimes.

Having established the consistency of our findings with prior studies, we now take the opportunity to perform a direct comparison between the results obtained using our ProLB solver, which employs the Lattice Boltzmann Method, and those presented in the study by Jiménez et al. [50], where a conventional Navier-Stokes solver was used. For this comparison, we adopt their chemistry and governing equations, employing a single progress variable equation and assuming a constant molecular weight for this specific simulation.

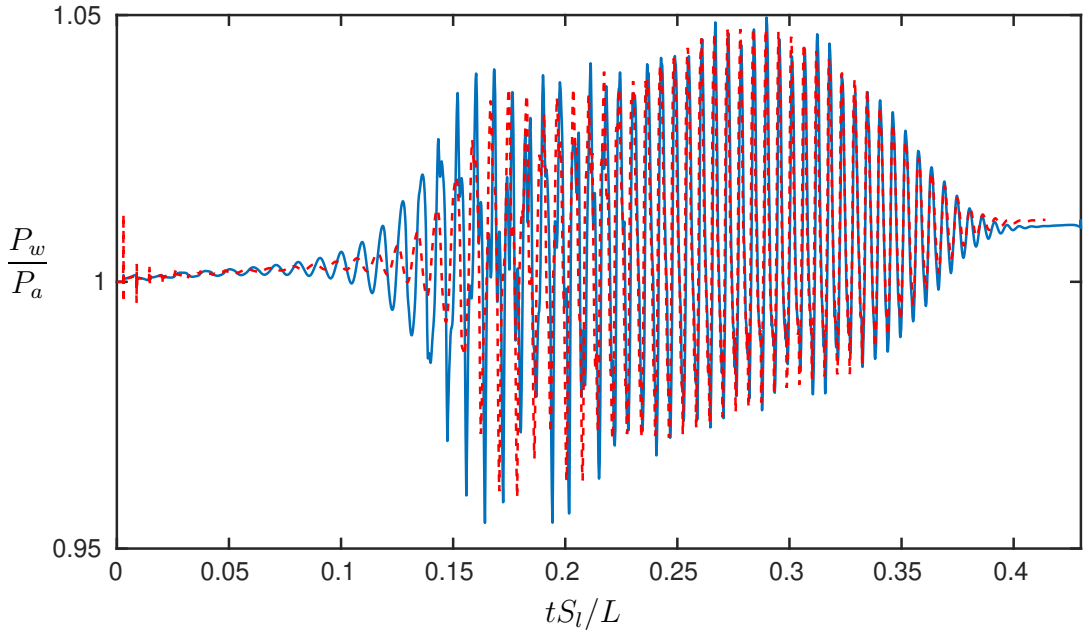

Figure 4.12: Pressure at the closed end wall of a channel of L = 2400 δ_D and width W = 40 δ_D: Blue - ProLB ; Red (dashed) - [50]

Figure 4.12 presents the pressure fluctuations at the closed wall, as obtained from

both the ProLB solver (in blue) and the NTMIX solver utilized by Jiménez et al. [50] (in red). By analyzing and comparing these results, we aim to ascertain the level of agreement between our ProLB solver and the established NTMIX solver.

Examining the results, we see that the initial stages (up to $tS_l/L \approx 0.2$) differ, this is most likely due to a different initialization (despite our best efforts). Nonetheless, once the flame is well into the tube, an excellent agreement is obtained, both in terms of frequency and amplitude. This alignment in the later stages underscores the reliability of our ProLB solver in capturing the thermoacoustic phenomena, consistent with the conventional NS solvers.

Influence of channel width: To the best of the authors' knowledge, the literature does not currently include an investigation into the dependence of instability gain on channel width. Such parametric studies are often considered costly in terms of computational resources. However, the present LB framework offers a significant advantage in this regard, as it significantly reduces the computational cost.

In this investigation, we focus on a channel of fixed length, $L = 1200\,\delta_D$, and exclusively consider non-symmetric flames akin to those depicted in case B of Figure 4.5. The objective of this study is to assess the influence of varying channel width on flame instability. We initiate our analysis with a narrow channel width of $W = 17.5\,\delta_D$, which is slightly below the DL cut-off wavelength (λ_c), as illustrated in Figure 4.3. Subsequently, by incrementally widening the channel to $W = 40\,\delta_D$, we observe a non-monotonic relationship between flame instability and channel width.

To provide further insights, Fig. 4.13 presents the consumption speed histories for four different channel widths: $W = (17.5,\ 20,\ 30, \& 40)\,\delta_D$, corresponding to cases A to D, respectively. This visualization allows us to examine the variation in flame instability across different channel widths.

For channel widths (W) below the cutoff value (case A), DL instability does not occur, and the flame remains nearly planar, resembling the scenario presented in Figure 4.3a, with a normalized consumption speed approximating unity.

As expected, the mean values for consumption speed increases with the channel width (case A to D) because the flame has more space to wrinkle and develop a large area compared to the channel cross-section.

However, for a channel width exceeding twice the cutoff value (case D), the observed gain in mean consumption speed is minimal in contrast to intermediate widths (cases B and C). Interestingly, for these intermediate widths, a noticeable drop in mean consumption speed is discernible before it returns back to its appropriate mean con-

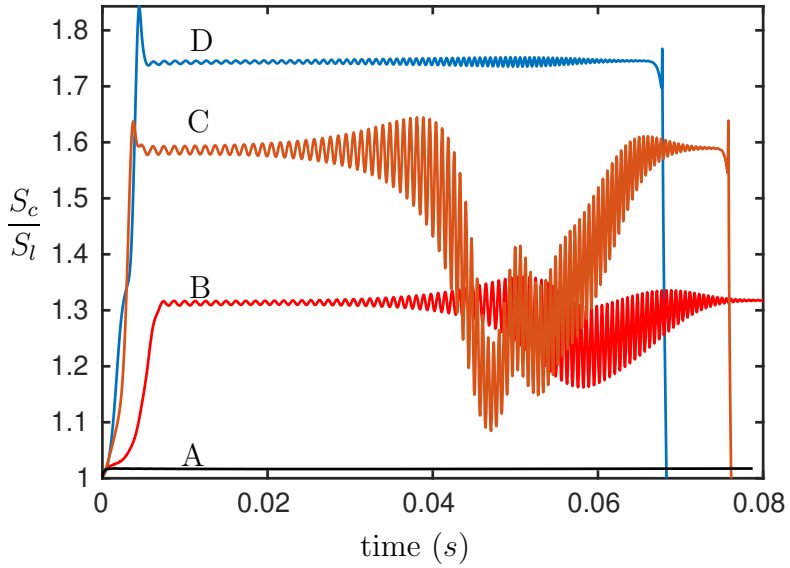

Figure 4.13: Flame consumption speed in a channel of length $L = 1200\,\delta_D$ and different widths: (**A**): W = 17.5 δ_D; (**B**): W = 20 δ_D; (**C**) W = 30 δ_D; (**D**) W = 40 δ_D

sumption speed. This phenomenon appears to be an effort at flame stabilization induced by intense thermoacoustic excitation, a phenomenon which we will explore further in the subsequent subsection.

4.5.3 Flame dynamics in long-narrow channels

In the final section of this chapter, motivated by the experimental work conducted by Searby [93], we undertake investigations to explore the possibility of achieving parametrically stabilized flat and cellular flames within long but narrow channels. Adopting a similar approach employed in the computation of figure. 4.11b, we initiate the study with an initially perturbed flame front within a channel of width $W = 40\,\delta_D$ and length $2400\,\delta_D$. In fact, figure. 4.11b is a zoom of the same case in the early stages.

Figure 4.14a illustrates the temporal evolution of the consumption speed within this channel under non-slip boundary conditions. Four regions (Z1 to Z4) are identified in the plot, for which successive flame contours are reported in Figure. 4.15. Additionally, figure 4.14b presents the normalized pressure at the closed end of the channel. By examining these plots in conjunction with the iso-contours of temperature (which represent the flame shape), the dynamic behavior of the flames in these regions can be easily analyzed:

- **Zone Z1 (Fig. 4.15a):** The flame shape exhibits a non-symmetric pattern,

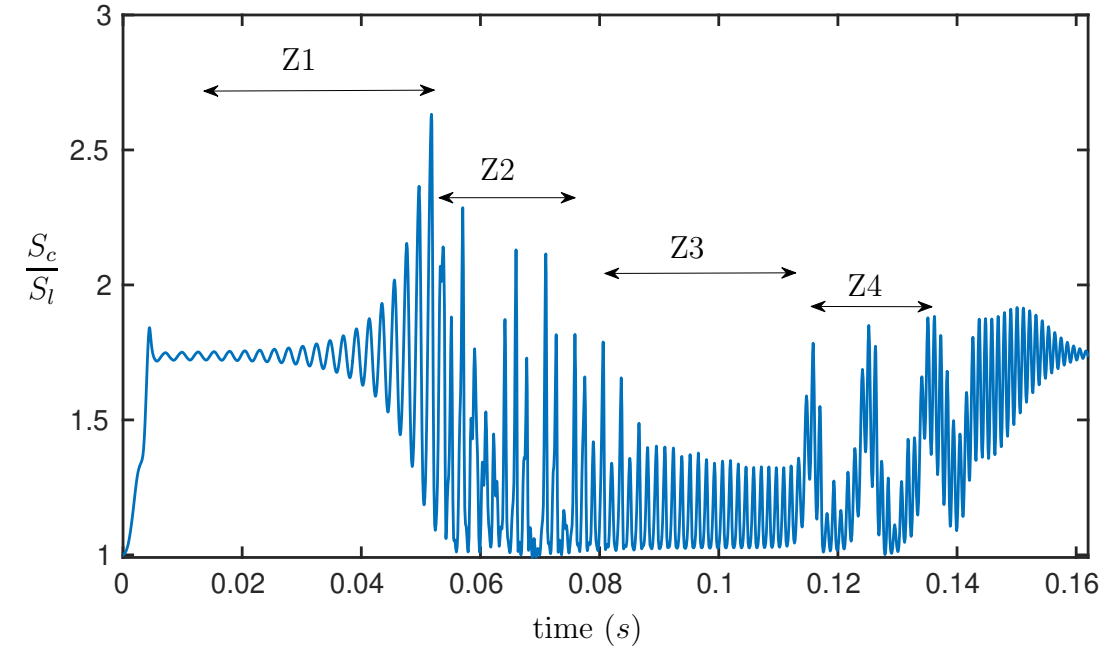

(a)

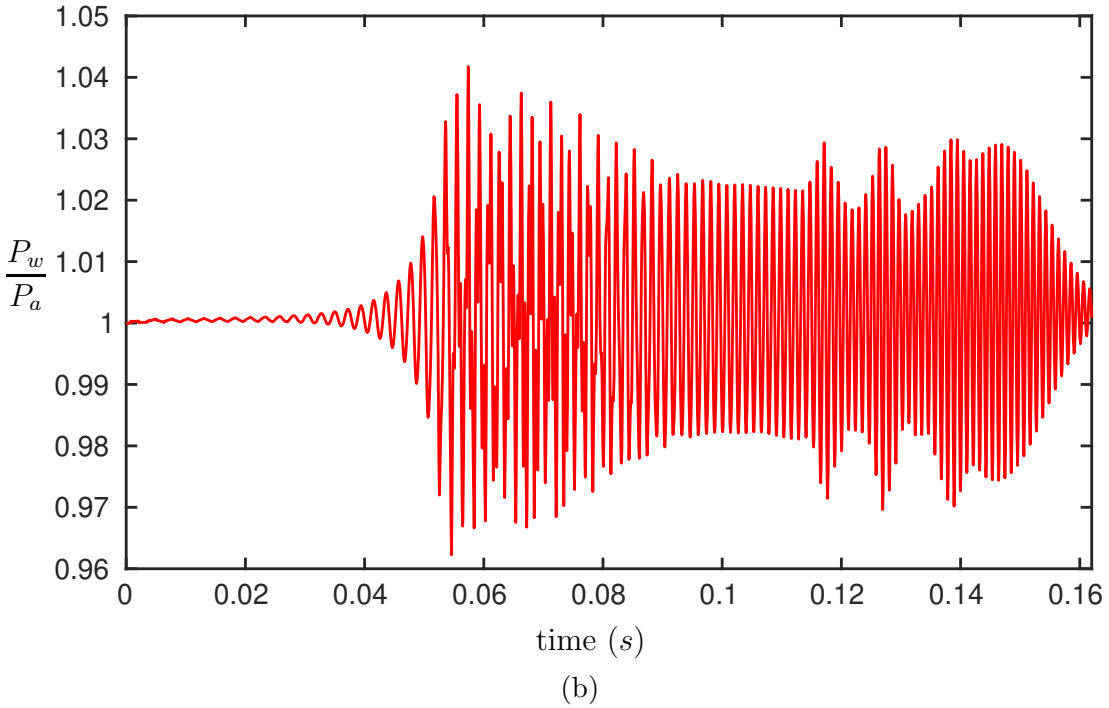

(b)

Figure 4.14: Thermoacoustics inside a non-slip channel of length L = 2400 δ_D and width W = 40 δ_D: ***(a)*** Depicts the normalized flame consumption speed and the different flame regimes observed; ***(b)*** Shows the normalized pressure at the closed end.

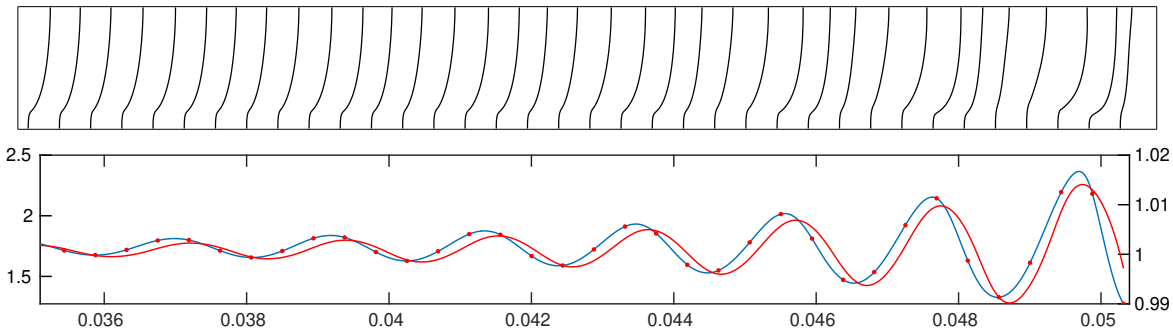

(a) Z1

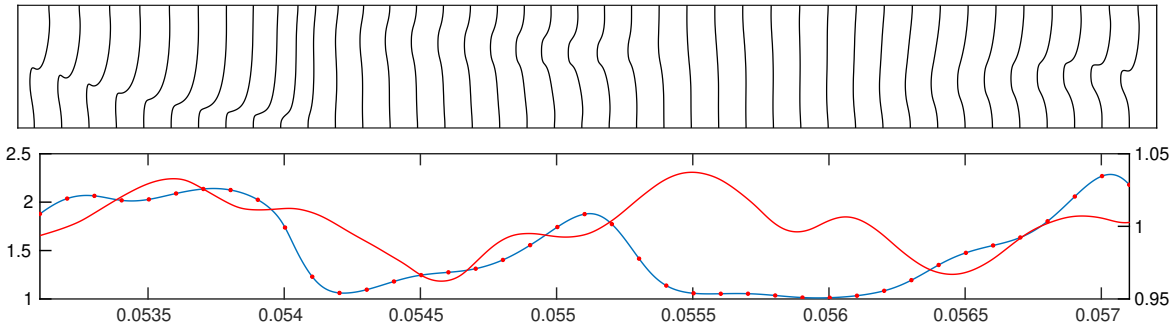

(b) Z2

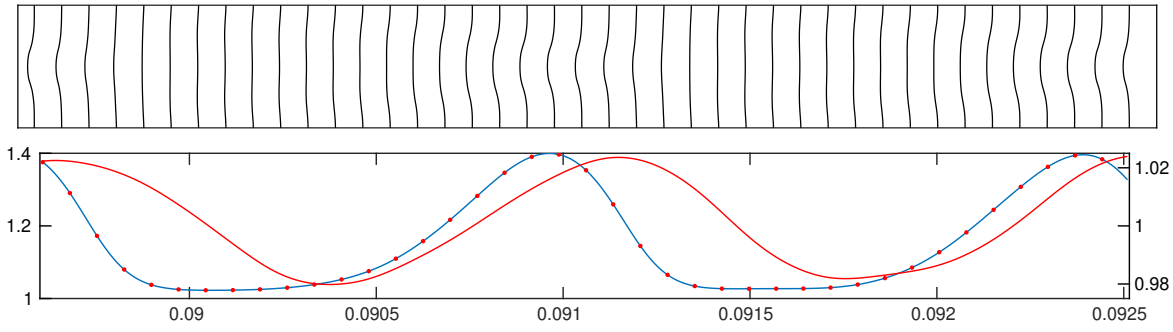

(c) Z3

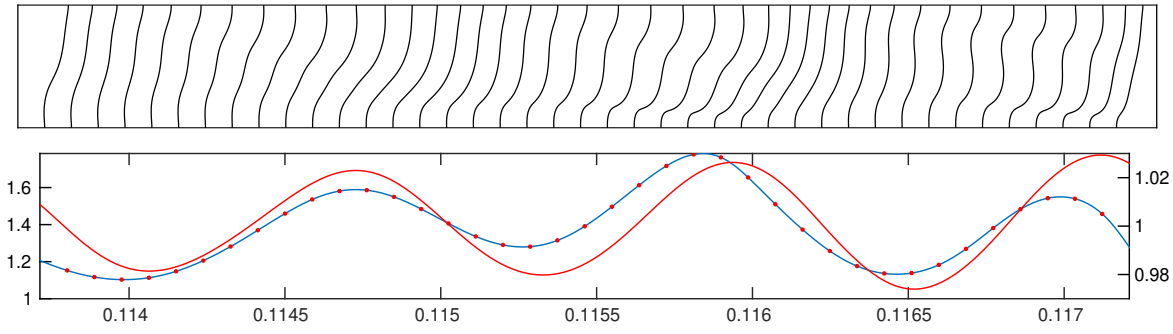

(d) Z4

Figure 4.15: Visualization of flame dynamics in response to instability in a non-slip channel. Temperature iso-contours depict different instability regions from Figure 4.14. Plots show consumption speed evolution (blue - left axis) and normalized pressure fluctuation at the closed wall (red - right axis). Red markers indicate the plotted time.

characteristic of the DL instability. Acoustic pressure and flame consumption speed amplify each other due to Rayleigh Criterion.

- **Zone Z2 (Fig. 4.15b):** The flame shape inverts at each acoustic period, indicating the presence of "parametric/secondary instability." However, certain factors cast doubt on this classification, such as the absence of multiple cells, low acoustic pressure amplitude, and early appearance in the channel.

- **Zone Z3 (Fig. 4.15c):** The acoustic pressure and consumption speed are reduced. The flame exhibits a symmetric shape (resulting in a smaller consumption speed). It oscillates at the acoustic period indicating the presence of the "primary instability."

- **Zone Z4 (Fig. 4.15d):** This corresponds to a region before the complete transition of the flame shape to a non-symmetric solution. Here, the formation of small cells can be observed, but the flame still seems to oscillates at the acoustic period.

Having failed to observe a parametrically re-stabilized flat flame in narrow non-slip channels, we now explore the possibility of achieving this by considering slip boundary conditions. Figure. 4.16 once again reports the temporal evolution consumption speed and normalized pressure at the wall. This time, only two zones, Z1 and Z2, are identified.

Zone Z1 in Fig. 4.16 exhibits similarities to the case with non-slip boundary conditions, where a non-symmetric flame shape (DL instability) leads to the coupling between acoustic pressure and flame consumption speed. This coupling results in their amplification, leading to the growth of the instability.

In contrast, the behavior observed in Zone Z2 of Fig. 4.16 is distinct. Here, a clear drop in the consumption speed towards the laminar flame speed is evident. Upon closer examination of the flame shapes in Fig. 4.17b, parametrically re-stabilized flat flames are observed.

Furthermore, during this regime (Zone Z2), it is observed that the consumption speed and acoustic pressure appear to be out of phase. However, upon closer examination of the pressure signal, we identify a three-quarters wave mode, as illustrated by the figure 4.18, and hence the Rayleigh criterion can still be satisfied. Additionally, as noted by Searby [93], this particular regime may correspond to the phenomenon previously identified as "vibrating flat flames" by Kaskan [51]. The growth of pressure

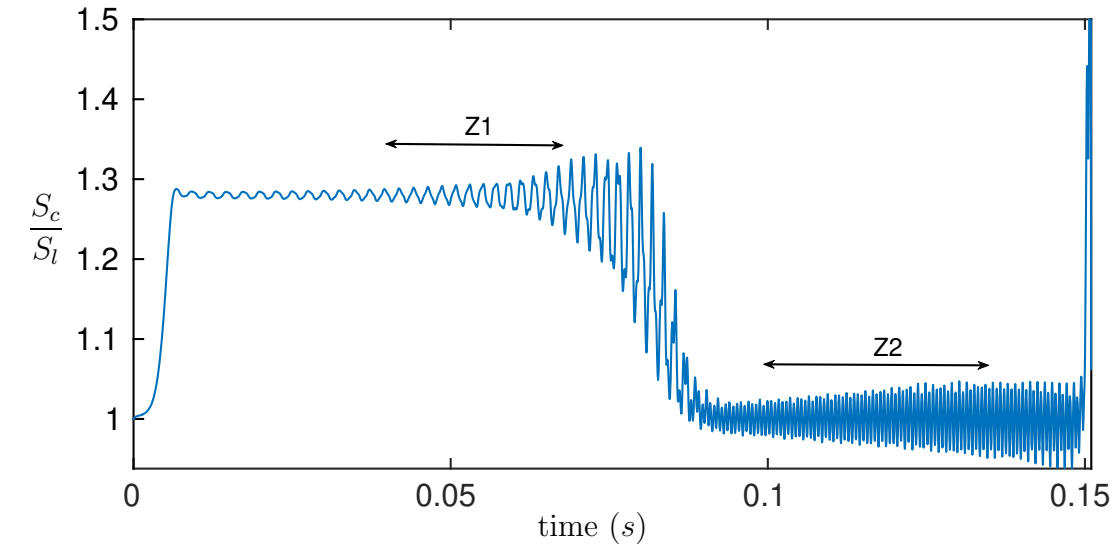

(a)

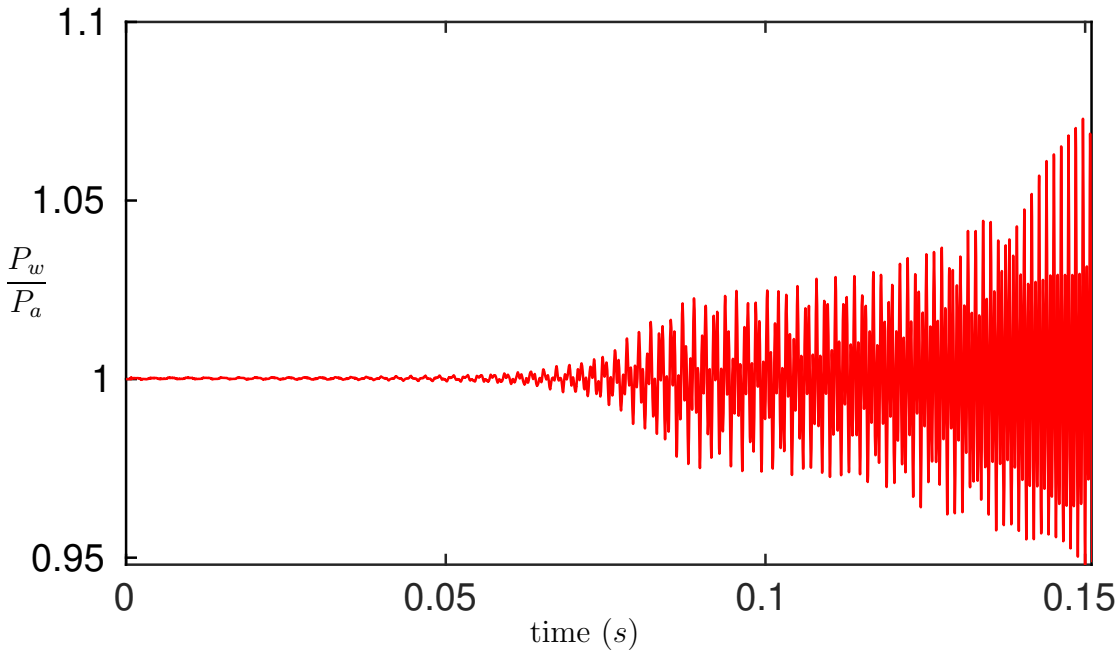

(b)

Figure 4.16: Thermoacoustics inside a slip channel of length L = 2400 δ_D and width W = 40 δ_D: **(*a*)** Depicts the normalized flame consumption speed and the different flame regimes observed; **(*b*)** Shows the normalized pressure at the closed end.

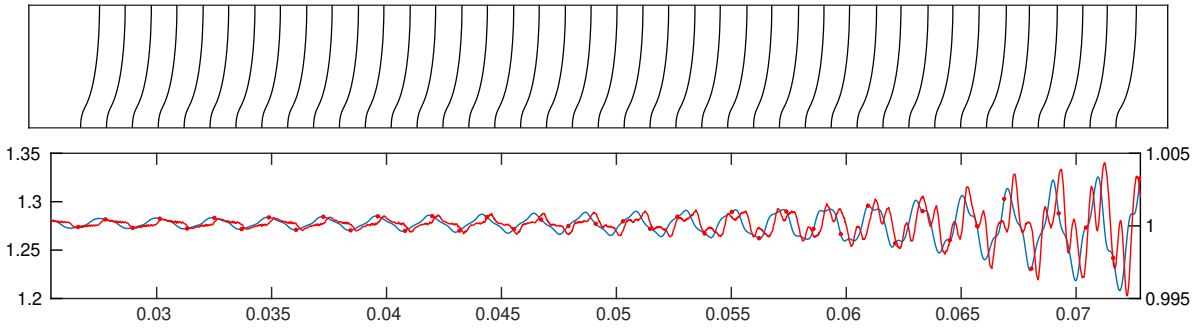

(a) Z1

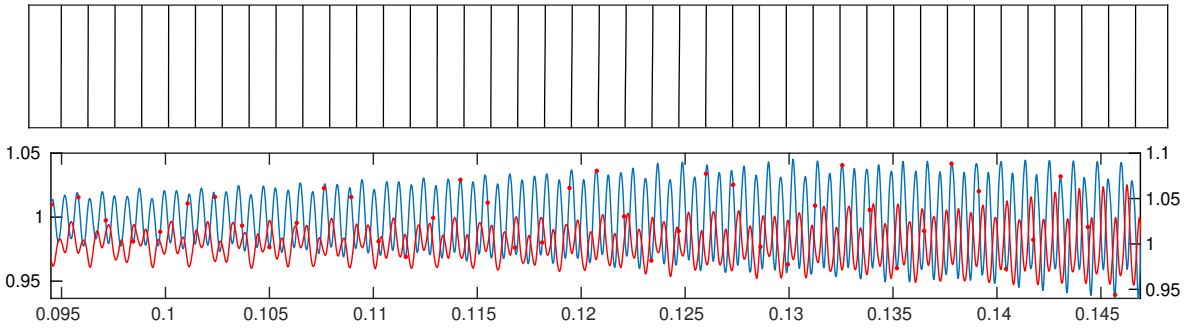

(b) Z2

Figure 4.17: Visualization of flame dynamics in response to instability in a slip channel. Temperature iso-contours depict different instability regions from Figure 4.16. Plots show consumption speed evolution (blue - left axis) and normalized pressure fluctuation at the closed wall (red - right axis). Red markers indicate the plotted time.

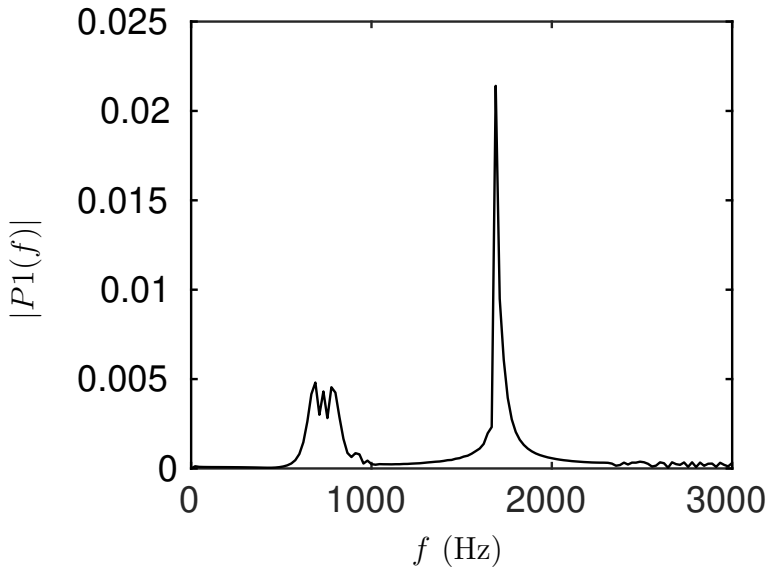

Figure 4.18: FFT Analysis of the Pressure Curve (Fig. 4.18) highlighting the presence of Three-Quarter Wave Mode in Zone Z2 of the Slip Channel.

fluctuations during this regime may be possibly be attributed to the adiabatic pressure coupling mechanism.

Finally, a comparison between Zone Z3 in Fig. 4.14 and Zone Z2 in Fig. 4.16, where only the boundary conditions are modified, raises the intriguing question of whether parametrically flat flames can exist in such narrow channels with non-slip boundary conditions.

4.6 Conclusion

In this chapter, we have systematically demonstrated the effectiveness of the Lattice Boltzmann Method (LBM) in accurately simulating thermoacoustic instabilities. Our exploration began with a canonical case of flame response to external acoustic perturbations, where we successfully identified primary instability, secondary instability, and re-stabilized flat flame regimes based on varying acoustic wave intensities. This alignment with previous findings [65, 94], confirmed the capability of LBM in capturing the accurate response of the flame to acoustics.

Expanding our investigation to flame propagation within closed 2D channels, we successfully established a clear connection between the developing thermoacoustic instability and the intrinsic eigenmodes of the channel. Furthermore, in our exploration of the impact of flame shapes and channel lengths on thermoacoustic instability, we verified the consistency of our observations with the previous studies [50]. Additionally, we reinforced the validity of our findings by directly comparing our results with those obtained from a conventional Navier-Stokes-based solver.

To enhance our understanding of channel-bound flame instabilities, we also conducted simulations varying the channel width. Surprisingly, we discovered that the relationship between channel width and flame instability amplification is not as straightforward as anticipated; wider channels do not always lead to increased instability. Our numerical investigations also underscored the pivotal role of boundary conditions, which not only impact the Darrieus-Landau cut-off wavelength but also exert strong influence on flame dynamics under acoustic fields.

In summary, the work presented in this chapter convincingly demonstrates the proficiency of Lattice Boltzmann Methods in tackling thermoacoustic instabilities. This highlights the potential of employing LB methods as reliable tools for predicting combustion instabilities in complex scenarios.

Chapter 5

Sound Generation due to Combustion

Contents

5.1 Introduction 89

5.2 LBM for Acoustic wave transport 90

5.2.1 Planar Standing Wave 91

5.2.2 Planar pulse propagation 93

5.2.3 2D Acoustic Pulse 96

5.3 Sound generation and propagation 98

5.3.1 Acoustically excited premixed flames 98

5.3.2 Setups to study sound generation during flame annihilation . 102

5.3.3 Effect of Lewis Number 106

5.4 Sound generation by Hydrogen flames 108

5.4.1 Effect of Chemistry 109

5.4.2 Parametric study of sound generation by hydrogen flames . . 111

5.4.3 Pressure peaks in Planar flame Annihilation 113

5.5 Conclusion 119

5.1 Introduction

Combustion-generated sound, originating directly from the flame or indirectly from flow inhomogeneities downstream of the flame, plays a pivotal role in the operational stability of combustion systems. These acoustic phenomena not only contribute to

the initiation and growth of thermoacoustic instabilities, a significant challenge in the design and operation of combustion systems, but also raise environmental concerns due to their contribution to noise pollution [13, 32]. In light of evolving environmental standards and the push for cleaner and quieter fuels, the acoustic characteristics of hydrogen fuels represent a knowledge gap that this chapter aims to address.

A cornerstone of this research is the utilization of the Lattice Boltzmann Method (LBM), renowned for its low dissipation properties in modeling acoustic transport [11, 64] and its architecture, which lends itself to highly parallelizable high-fidelity simulations [103, 117]. These features are deemed to hold significant advantages in the study of combustion-generated sound and its subsequent propagation to the far field. The potential of LBM in enhancing our understanding of combustion-generated sound is considerable. However, despite its promise, most of the touted acoustic capabilities of LBM is predicated on the conventional athermal LBM-BGK model in the existing literature.

Within this context, our first objective is to demonstrate the dissipative and isotropic capabilities of our thermal hybrid LBM solver. Following this, we will investigate the phenomenon of sound generation due to flame annihilation, employing a simple chemistry model. This analysis will help in understanding the fundamental mechanisms of sound generation in combustion processes. Finally, leveraging the capabilities of the solver and the results from the simple chemistry model, along with insights from existing literature [13, 49, 100, 107], we will explore the complexities of sound generation due to hydrogen flames.

5.2 LBM for Acoustic wave transport

In this section, we assess the acoustic performance of our Hybrid LBM-HRR model, focusing on three key aspects: dissipation, dispersion, and isotropy of our computations. To evaluate these, we have selected three canonical configurations:

- Evolution of a standing acoustic wave.
- Evolution of a propagating acoustic wave.
- Evolution of a 2D acoustic pulse.

1D acoustic wave equation

Considering viscosity and heat diffusion, the conventional homogeneous acoustic wave equation can be derived from the linearized Navier-Stokes (NS) system to obtain a

lossy-wave equation:

$$\frac{\partial^2 P_1}{\partial t^2} = \left(c_0^2 + \left[\frac{4}{3}\nu + \frac{\gamma - 1}{Pr}\nu + \nu_B\right]\frac{\partial}{\partial t}\right)\frac{\partial^2 P_1}{\partial x^2} \tag{5.1}$$

In our solver, we explicitly set the bulk viscosity (ν_B) to zero and the kinematic viscosity (ν) to $1.5 \times 10^{-2}\,\mathrm{m}^2/\mathrm{s}$. Additionally, we assign specific values to the Prandtl number (Pr) and the ratio of specific heats (γ), which are 0.6 and 1.4, respectively. These particular parameter values were selected to align with the findings of Bres et al. [11], who assessed a "classical isothermal LBM-BGK" model.

Unlike our HRR model where we can explicitly set ν_B to zero, they determined that the bulk viscosity in the classical isothermal LBM-BGK model is conventionally $\frac{2}{3}\nu$. Consequently, our model, with added heat diffusion consideration, imposing these specific parameter values yields the same effective viscosity of 2ν as in [11]. This consistency allows for a straightforward comparison between the isothermal LBM-BGK model and our Hybrid Pressure-based HRR model for interested readers.

Furthermore, for a plane wave given by $P_1 = \hat{A}\exp\left[i(\hat{k}x - \hat{\omega}t)\right]$, solutions of equation (5.1) satisfy the dispersion relation:

$$\left(c_0^2 - 2i\hat{\omega}\nu\right)\hat{k}^2 = \hat{\omega}^2. \tag{5.2}$$

Here, $\hat{A}$, $\hat{k}$, and $\hat{\omega}$ are considered as complex values. Solutions to this dispersion relation can be applied either to perform a temporal analysis on a standing wave by solving for $\hat{\omega}$ or or to conduct a spatial analysis for a traveling wave by solving for $\hat{k}$.

5.2.1 Planar Standing Wave

To investigate phase speed variation (dispersion) and temporal dissipation due to our numerical scheme, we consider a standing plane acoustic wave within a domain equal to the wavelength (λ) of the wave. This allows us to perform a temporal analysis by using a fixed number of points per wavelength, denoted as $N_{ppw} = \lambda/\Delta x$.

For this configuration (setup 1), we assume a periodic domain without external flow. The grid size Δx is constant, and the computational domain size is (λ, Δx, Δx). The initial conditions are:

$$P_1(x, y, z, 0) = A\sin\left(\frac{2\pi x}{\lambda}\right), \qquad \rho_1 = \frac{P_1}{c_0^2}, \quad u_1 = v_1 = w_1 = 0, \tag{5.3}$$

where $A = 10^{-3}p_0$ is chosen to ensure linearity, and the simulation time is set to 50 periods, which is adequate enough to capture dispersion and dissipation effects. The

form of the acoustic pressure at time t as expressed by Bres et al. [11] is considered here:

$$P_1(x, y, z, t) = A \exp\left[-\left(\alpha_T + \alpha_T^{num}\right) t\right] \sin\left[k\left(x - \left(c_T + c_T^{num}\right) t\right)\right] \tag{5.4}$$

Here, α_T^{num} and c_T^{num} represent the variation in phase speed (dispersion) and temporal dissipation rate due to the numerical scheme, respectively. Physical/theoretical values are calculated by solving for the complex angular frequency $\hat{\omega}$ in the dispersion relation eq. (5.2):

$$\hat{\omega} = -ik^2\nu \pm kc_o\sqrt{1 - (k\nu/c_0)^2} \tag{5.5}$$

yeilding $c_T = \mathrm{Re}(\hat{\omega})/k$ and $\alpha_T = -\mathrm{Im}(\hat{\omega})$ as :

$$c_T = c_o\sqrt{1 - \left(\frac{k\nu}{c_0}\right)^2} \qquad \alpha_T = k^2\nu \tag{5.6}$$

Given these theoretical values, we can extract the numerical coefficients from the time signal (Fig. 5.1).

Numerical Analysis

Figure 5.1 depicts the time signal at an acoustic pressure antinode for a standing wave with a frequency of $f = 10$kHz at various mesh resolutions. We observe that the numerical dissipation rate α_T^{num} is negligible even at lower resolutions (e.g., $N_{ppw} = 8$), while numerical dispersion decreases with higher resolutions. These trends are consistent with findings by Bres et al. [11] and Marié et al. [64]. Furthermore, Tab 5.1 provides details on the relative numerical errors for dispersion and dissipation at different mesh resolutions.

N_{ppw}	4	8	12	24
$\frac{\alpha_T^{num}}{\alpha_T}$	0.09	0.013	-0.001	-0.003
$\frac{c_T^{num}}{c_T}$	-0.081	-0.020	-0.009	-0.0024

Table 5.1: Relative dispersion and dissipation numerical error for different points per wavelength.

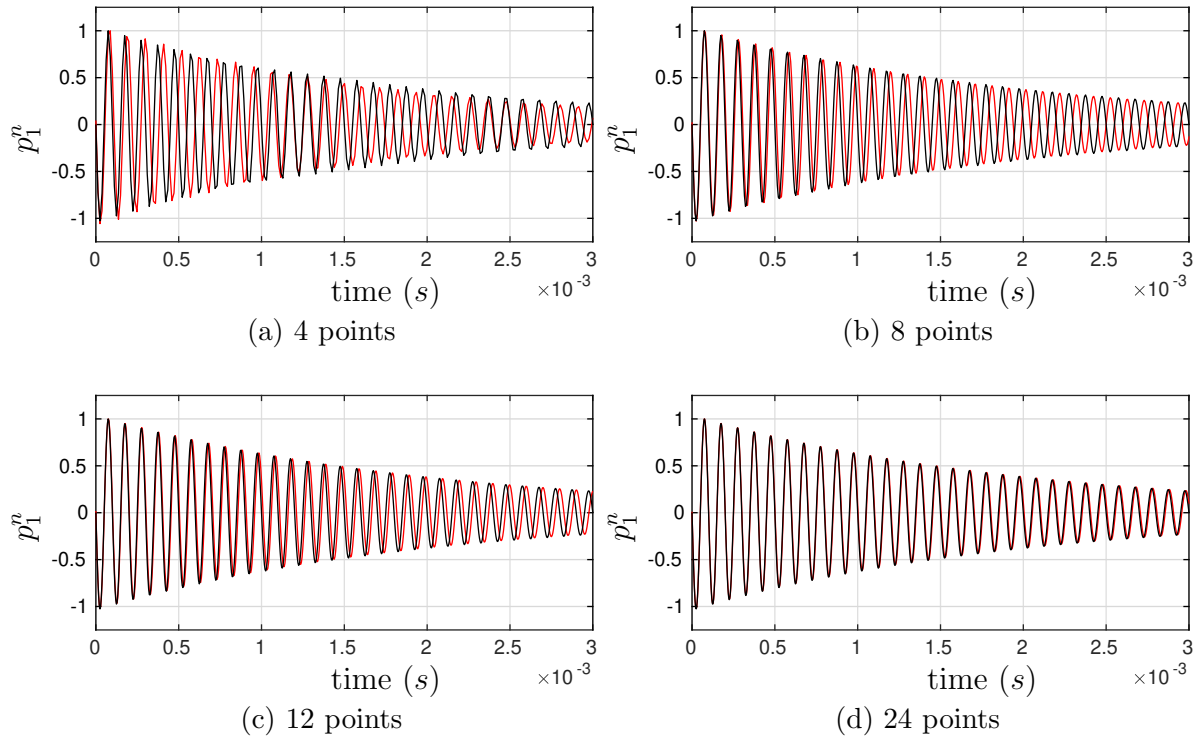

(a) 4 points (b) 8 points

(c) 12 points (d) 24 points

Figure 5.1: Normalized acoustic pressure-time history at a pressure antinode for setup 1 for different mesh resolution (Δx). Black –theory, Red – ProLB

5.2.2 Planar pulse propagation

Similar to the temporal analysis of a standing wave, we perform spatial analysis by considering a traveling wave. We focus on a propagating Gaussian pulse signal rather than monochromatic acoustic waves. This approach, which involves the superposition of various frequency components (ω values), is more representative of practical scenarios and it also provides a comprehensive view of dissipation across different frequencies in a single simulation.

For this configuration (setup 2), we initialize a planar pulse with a Gaussian shape at the origin:

$$P_1(x, y, z, 0) = A \exp\left(-\ln(2)\frac{x^2}{\sigma^2}\right), \qquad \rho_1 = \frac{P_1}{c_0^2}, \quad u_1 = \frac{P_1}{\rho_0 c_0}, \quad v_1 = w_1 = 0 \tag{5.7}$$

Here, $\sigma = 0.01\,\mathrm{m}$ represents the initial width of the pulse, and $A = 10^{-3} p_0$. The grid size Δx remains constant and uniform across the computational domain, which has dimensions of $(300\sigma, \Delta x, \Delta x)$. The boundary conditions are periodic in all three directions.

We transform the pulse signal in the time domain fig 5.2a into a linear combination of acoustic waves with different frequencies in Fourier space. The spatial dependence of the Fourier coefficient of pressure, $\hat{P}_1(x,\omega)$, follows the relation:

$$\hat{P}_1(x,\omega) = \hat{P}_1(0,\omega)\exp\left[-\left(\alpha_S + \alpha_S^{num}\right)x\right]\exp\left[i\omega\frac{x}{c_S + c_s^{num}}\right] \tag{5.8}$$

Here, c_S^{num} and α_S^{num} are the numerical variations in phase speed and spatial dissipation rate, respectively. We calculate the expected values of c_S and α_S by solving for the complex wavenumber $\hat{k}$ in the dispersion relation (eq. (5.2)):

$$\hat{k} = \pm\omega/\sqrt{c_0^2 - i\omega 2\nu} \tag{5.9}$$

For a plane wave traveling in the $+x$-direction, the phase speed $c_S = \frac{\omega}{\mathrm{Re}(\hat{k})}$ and spatial dissipation rate $\alpha_S = \mathrm{Im}(\hat{k})$ can be expressed as follows [11]:

$$c_S = \sqrt{2}c_0\sqrt{\frac{1+(\omega\tau_S)^2}{\sqrt{1+(\omega\tau_S)^2}+1}}, \qquad \alpha_S = \frac{\omega}{\sqrt{2}c_0}\sqrt{\frac{\sqrt{1+(\omega\tau_S)^2}-1}{1+(\omega\tau_S)^2}} \tag{5.10}$$

Here, $\tau_S = \frac{2\nu}{c_0^2}$. Additionally, the loss in intensity level with the distance of propagation can be estimated by the spatial absorptive loss a_S, expressed in Neper per meter (Np/m), which is equivalent to 8.686dB/m, with the Neper (Np) being a dimensionless unit.

Numerical Analysis

Figure 5.2a presents the time-history of the acoustic pressure for the planar Gaussian pulse (setup 2) with a resolution of $\Delta x = 0.001$ m. The time signal is displayed at the reference position and after a distance of 0.5 m. Figures 5.2b illustrate the relative numerical deviations in dissipation rates (α_S^{num}) in Np/m. Consistent with the findings of Bres et al. [11], these results show minimal numerical errors.

Moreover, the intensity loss attributed to numerical dissipation remains low, even at relatively coarse resolutions (e.g., $\Delta x = 0.004$ m). To illustrate, the loss of intensity of a propagating plane wave, per meter of propagation, due to numerical dissipation can be computed as $8.686\,\alpha_S^{num}$. For instance, a plane wave with a frequency of 10kHz on a mesh with $\Delta x = 0.004$ m (approximately 8 points per wavelength) would undergo an intensity loss of around 1.9 dB per meter of propagation in our solver.

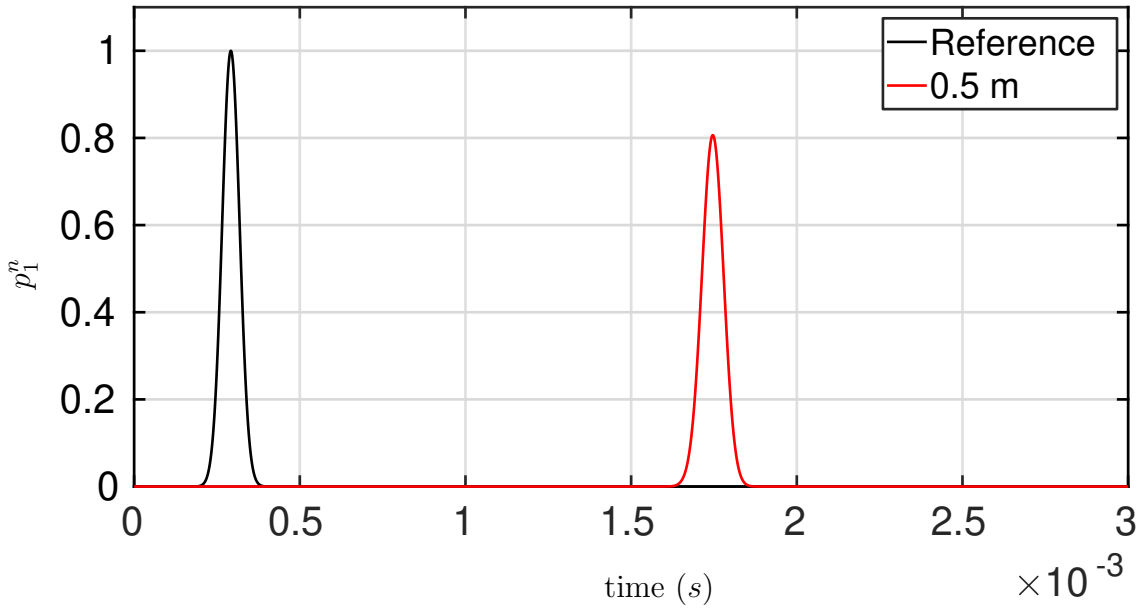

(a) Acoustic pressure-time history for setup 2: Black – signal at reference probe; Red– signal at 0.5 m.

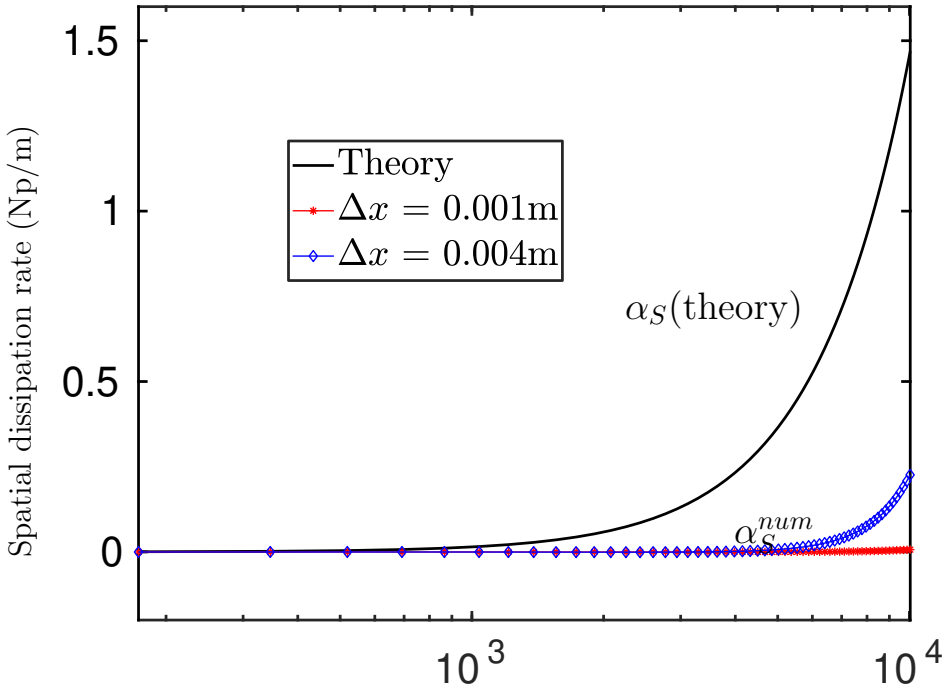

(b) Dissipation

Figure 5.2: Illustration of theoretical (α_S) and numerical dissipation (α_S^{num}) as function of frequency (f) and mesh resolution (Δx) for setup 2.

5.2.3 2D Acoustic Pulse

In this section, we conclude our analysis of the acoustic transport properties of our solver by focusing on the propagation of a two-dimensional acoustic pulse. We emphasize particularly on the amplitude decay in a non-viscous, two-dimensional medium and the isotropic performance of our solver.

For this configuration (setup 3), we initiate a Gaussian pulse at the center of a periodic computational domain, sized $(100\sigma, 100\sigma, \Delta x)$, with the conditions defined as:

$$P_1(x, y, z, 0) = A \exp\left(-\ln(2)\frac{x^2 + y^2}{\sigma^2}\right), \qquad \rho_1 = \frac{P_1}{c_0^2}, \quad u_1 = v_1 = w_1 = 0 \tag{5.11}$$

Here, $\sigma = 0.01\,\text{m}$ represents the initial width of the pulse, and the amplitude A is set to $A = 10^{-2} p_0$. The grid resolution, $\Delta x = 0.001\,\text{m}$, remains constant and uniform across the computational domain. Differing from the previous two setups, we introduce zero viscosity in this simulation to facilitate the observation of the well-documented amplitude decay behavior of an acoustic wave in relation to the distance propagated. Specifically, in a two-dimensional medium, this decay is mathematically expressed as $\frac{1}{\sqrt{(r)}}$, a relationship derived from the dispersion of energy over the circumference of an expanding circle as the wave propagates.

Numerical Analysis

Figure 5.3a illustrates the propagation of the acoustic pulse at a selected time t. Figure 5.3b presents the normalized pressure-time history, recorded at sensors placed every $25\Delta x$ over the positive x axis. The log-log plot of the peak amplitudes against the distance, as shown in Figure 5.3b, confirms that the decay rate of amplitude with respect to distance aligns precisely with the anticipated $\frac{1}{\sqrt{(r)}}$ value.

Additionally, figure 5.3d depicts the acoustic pressure-time history at a radius of $r = 0.6\,\text{m}$, measured at various angular positions as illustrated in Figure 5.3c. The overlay of these profiles demonstrates the isotropy of our solver. This isotropic response not only validates the accuracy of our simulation setup but also underscores its capability to replicate the realistic behavior of acoustic waves in a two-dimensional medium.



(a) Visualization of the 2D Acoustic Pulse

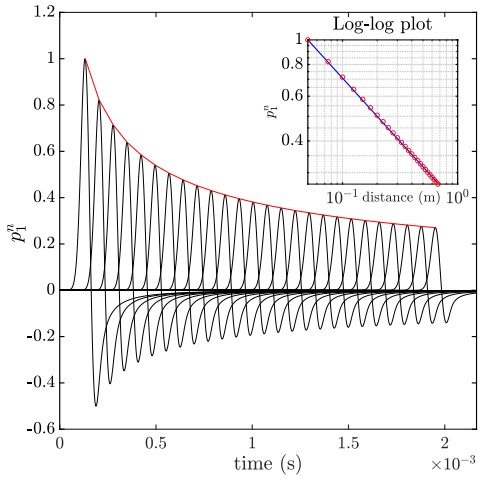

(b) Amplitude decay

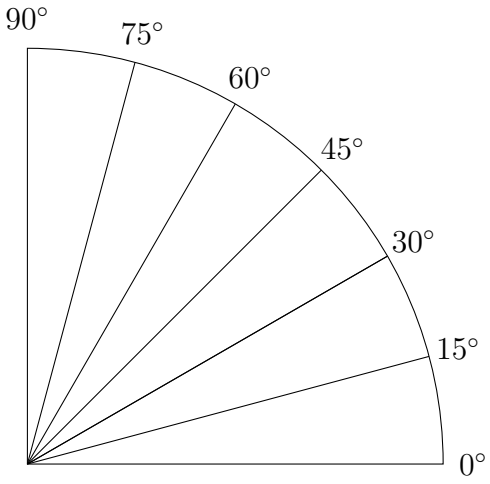

(c) Diagram of different angles chosen for isotropy testing

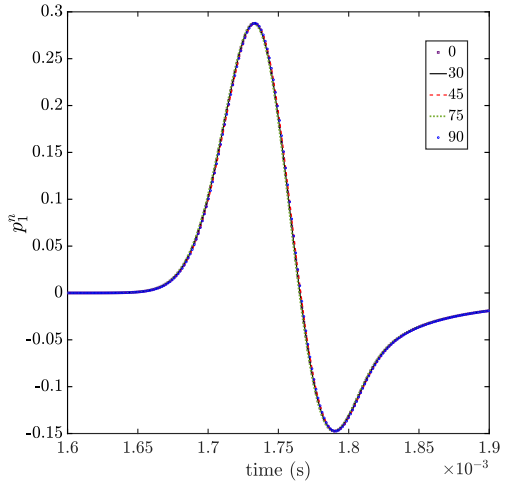

(d) Pressure-time histories at $r = 0.6\,\mathrm{m}$ along different angular positions

Figure 5.3: Comprehensive Analysis of Two-Dimensional Acoustic Wave Propagation illustrating various aspects of the simulation, including the wave propagation, amplitude decay, and isotropy testing.

5.3 Sound generation and propagation

Now that we have established the nature of our hybrid LBM solver for acoustic transport, let us explore the generation and propagation of sound resulting from combustion, commonly known as Combustion Noise. To gain insight into the process of 'Direct sound' generation during combustion, we examine a two-dimensional laminar premixed flame that is acoustically excited within an open domain, as studied by Talei et al. [102].

5.3.1 Acoustically excited premixed flames

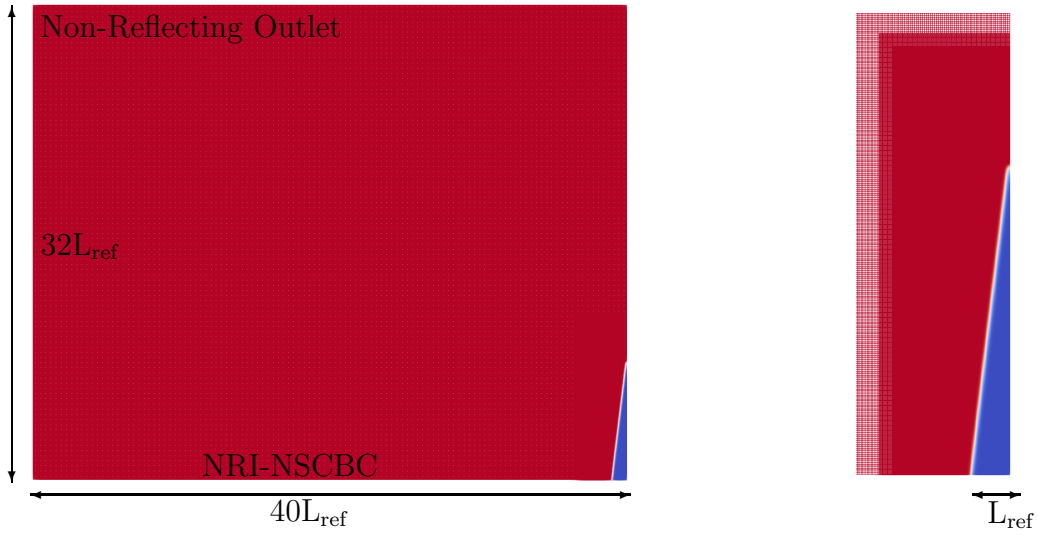

(a) One-sided computational domain (b) Zoom

Figure 5.4: Schematics of computational domain: **(a)** One sided computational domain in terms of reference length $L_{ref} = 10\delta_T$. **(b)** Zoom on the premixed flame illustrating the mesh refinements.

Setup

The schematics of the computational domain focusing on a half-domain with a reference length of $L_{ref} = 10\delta_T$ is depicted in Fig. 5.4a, . In this configuration, We implement a mesh refinement strategy involving three levels, with both Δx and Δt doubling at each grid level (Fig. 5.4b), and the finest mesh resolution is approximately $\Delta x \approx \delta_T/10$. Additionally, to replicate the conditions studied by Talei et al. [102], we employ a single-step chemistry model F $\longrightarrow$ P (Appendix B), characterized by a unity Lewis number $Le = 1$. We utilize the NRI-NSCBC boundary formulation to establish a stable 2D

conical flame by imposing an inlet velocity $u_{in} = 8S_l$, constrained within the interval $(-L_{ref}, L_{ref})$, and set to zero otherwise.

Once this stable flame is established, we introduce acoustic fluctuations at the inlet boundary. These fluctuations take the form of $u_a^t = 0.25\, u_{in}\, \sin(2\pi f T)$. As mentioned in Section 2.3.1, to induce significant variations in flame surface area and heat release rate fluctuations ($\dot{\omega_{T_1}}$), we apply low-frequency modulation, setting the Strouhal number at $St = 0.025$, defined by:

$$St = \frac{f L_{ref}}{c_f} \tag{5.12}$$

Analysis

In Figure 5.5, We present the dilatation field ($\nabla \cdot \boldsymbol{u}$) – often used in aeroacoustics, during one period of acoustic excitation. Notably, the images reveals two significant sound generation events:

1. Flame annihilation – complete isolated burning of a pocket of fresh gases. (***c*** in Fig. 5.5).

2. Pinch-off – separation of a pocket of fresh gases (***f*** in Fig. 5.5).

Figure 5.6a displays the pressure fluctuations recorded by sensors positioned at $2L_{ref}$ intervals from the center of flame annihilation (Fig. 5.5***c***). To extract more precise insights into the amplitudes of pressure variation during both pinch-off and flame annihilation events, we applied a digital filtering technique to eliminate the continuous component induced by external excitation (noticeable by the pronounced frequency in Fig. 5.6b). This process resulted in a significantly cleaner curve (Fig. 5.6c). The refined pressure fluctuations reveal:

- Greater amplitude of pressure variation or sound generation during the pinch-off event compared to the flame annihilation event.

- Decay of the generated sound as we move away from the combustion region.

- Sound waves traveling at the local sound speed, determined by measuring the time delay between the signals.

Finally, the figure 5.7 presents HRR fluctuations ($\dot{\omega_{T_1}}$) and filtered pressure fluctuations ($\tilde{P}_1$) at a distance of $2L_{ref}$ from the center of flame annihilation, highlighting the evident correlation between HRR fluctuations (flame surface area variations) and the sound generation.

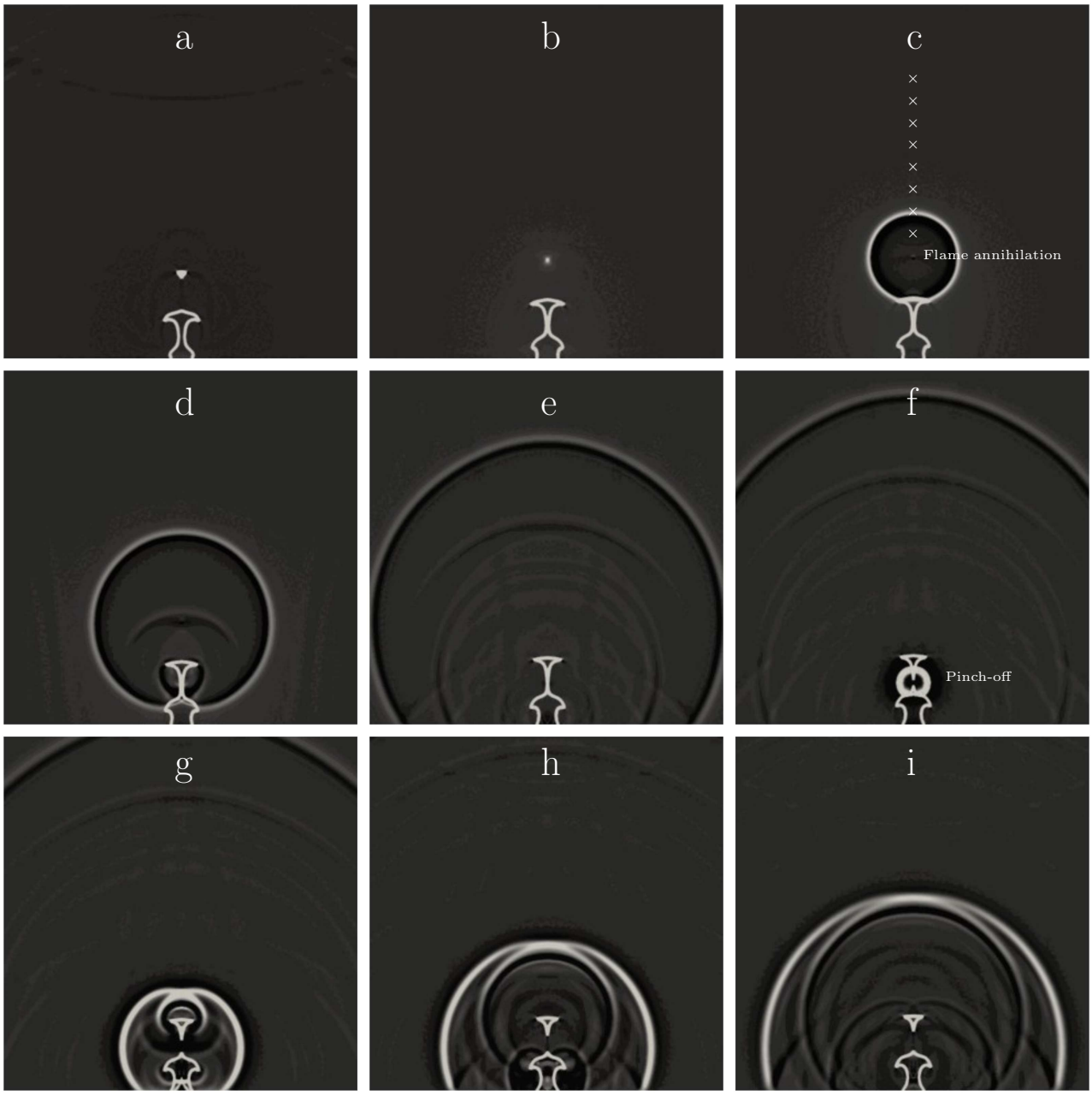

Figure 5.5: Illustration of sound generation and propagation due to "Pinch-off" and "Flame Annihilation" events depicted by dilatation field. Image ***c*** illustrates sound generated during the solo burning of pocket of fresh gases – "Flame Annihilation/ island burnout". Image ***f*** depicts the sound generation during "pinch off". The pressure sensors, illustrated by (×) in the image ***c*** are placed at every $2L_{ref}$ interval from the center of flame annihilation.

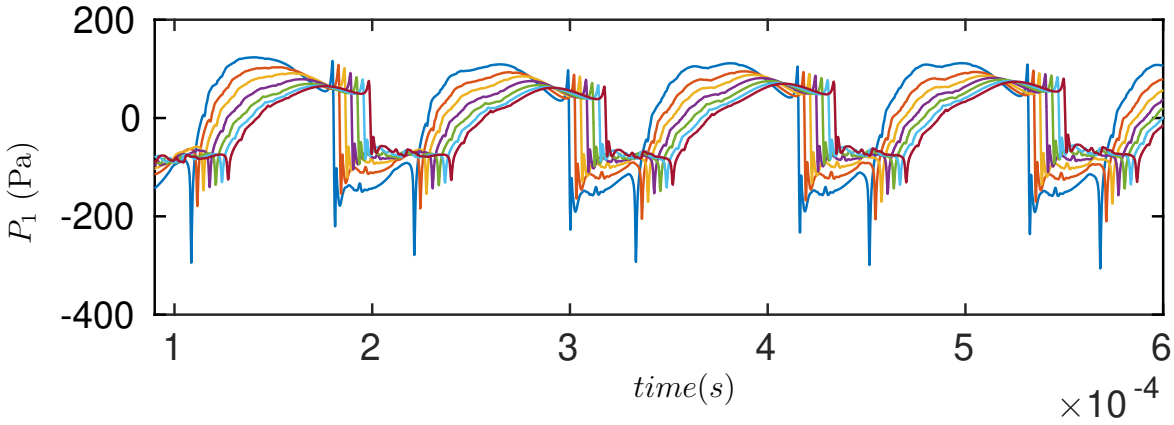

(a) Pressure fluctuations.

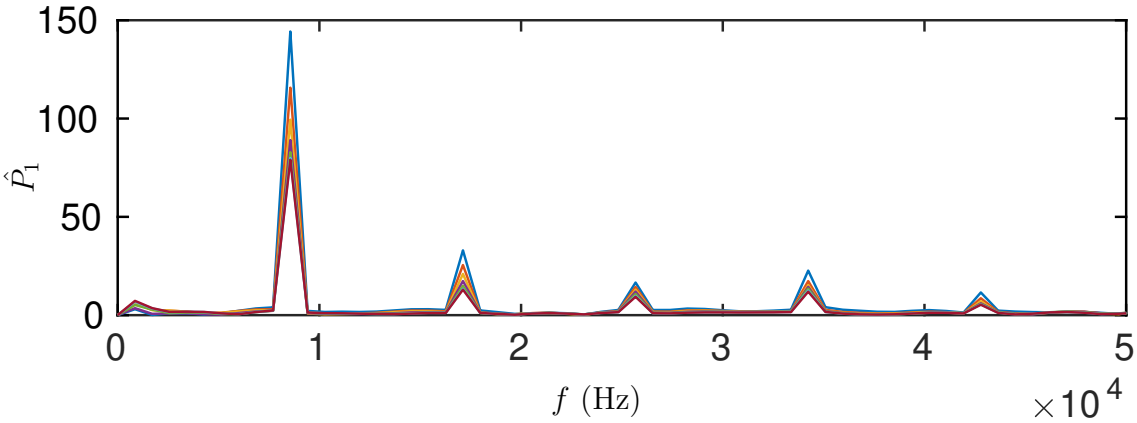

(b) Fourier signal of the pressure fluctuations highlighting the imposed acoustic frequency.

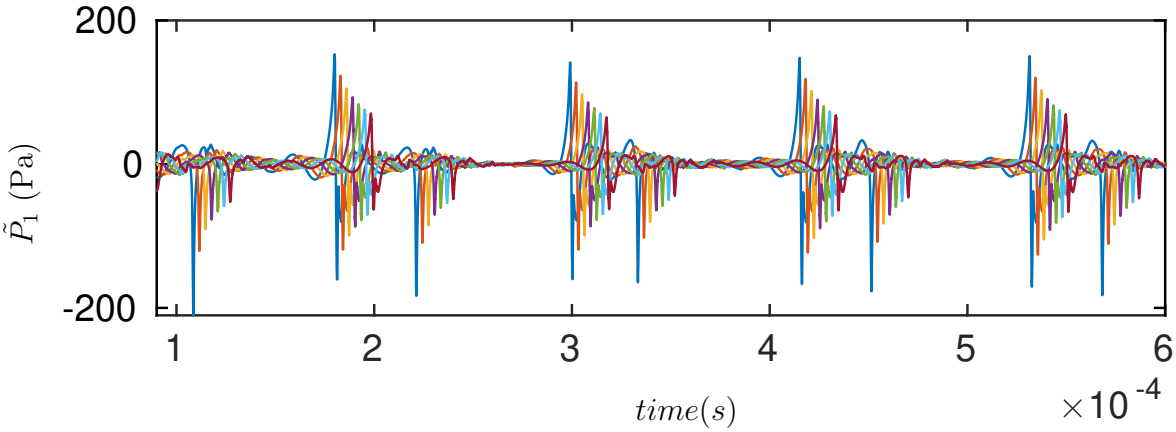

(c) Filtered pressure fluctuations signal.

Figure 5.6: Raw and filtered pressure fluctuation signals recorded at $2L_{ref}$ intervals from the center of flame annihilation (fig .5.5c), depicting pressure variations (sound generation) during flame annihilation and pinch-off events.

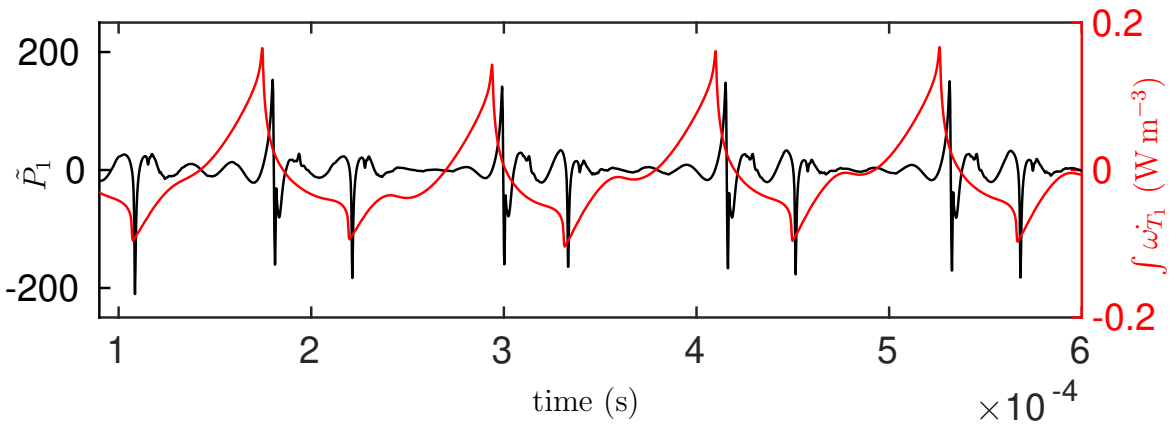

Figure 5.7: Correlation between HRR fluctuations and the Sound generation. — Pressure fluctuations at $2L_{ref}$ from the center of flame annihilation; — total heat release rate fluctuations.

5.3.2 Setups to study sound generation during flame annihilation

Talei et al. [101] demonstrated that the amplitude of generated sound depends on various factors, including Le and S_l. Conducting extensive acoustically excited flame simulations to assess the dependence of these parameters on sound generation is neither feasible nor justified. Consequently, they recommended the use of simpler setups, such as 2D circular flame implosion or even more cost-effective 1D planar flames' annihilation, to investigate sound generation phenomena during flame annihilation. Additionally, based on the insights from Baillot and Bourehla [3], who showed that once the pocket flame (pinched-off fresh gases) becomes rounded, the frequencies and amplitudes of forcing have no influence on its temporal evolution, making it suitable for an isolated study, enabling us to adopt a similar approach.

Setup

The configuration setups for 1D planar flame annihilation and circular flame implosion are depicted in Figure 5.8. In the 1D planar flame annihilation simulations, we initialize fully developed 1D flames at a distance of 10 δ_T from the center of annihilation on both sides. For the imploding circular flames, a circular flame is initially positioned 15 δ_T away from the center of annihilation. These flames consume fresh gases and converge towards the central point, where they collide/implode, resulting in their complete annihilation at $x = 0$.

Sensors are positioned at three distinct locations to monitor the evolution of temper-

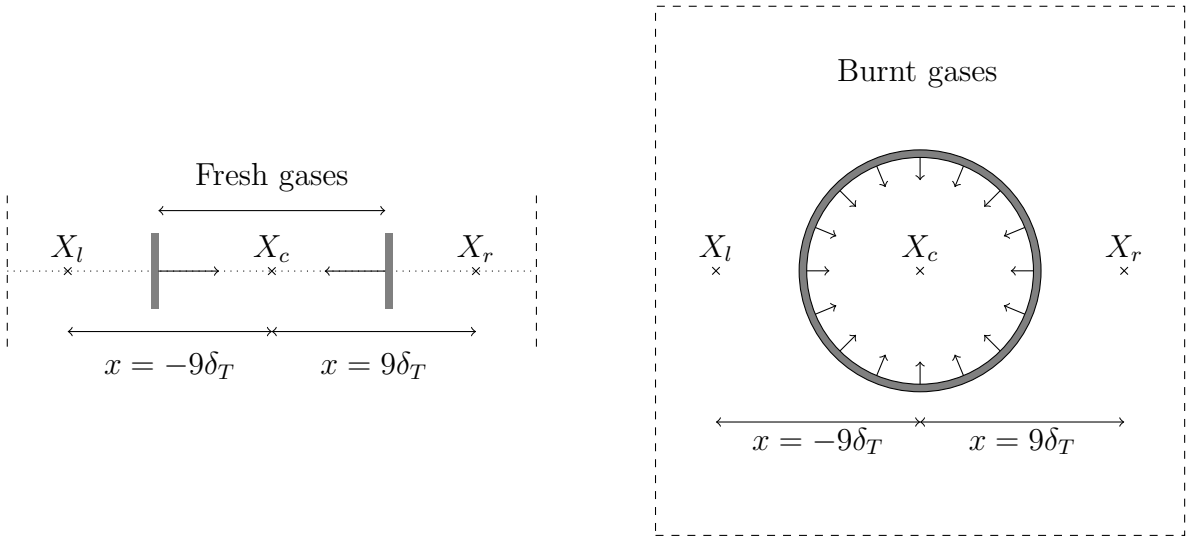

(a) 1D planar flame annihillation (b) Circular flame implosion

Figure 5.8: Configuration of 1D planar and circular flame annihilation.

ature, pressure, and species concentrations. These locations, denoted as X_c at $x = 0$, represent the central annihilation point, while X_r and X_l, situated at $x = \pm 9\delta_T$ distances from the center, respectively, provide additional information such as decay in amplitude of the signals.

NSCBC boundary conditions [82] are employed at the outlets. For the planar annihilation configuration, completely non-reflecting outlets were utilized. On the other hand, in the case of imploding circular flames, a pressure (P_0) is imposed at infinity to ensure consistency with previous results from Talei et al. [101]. It is worth noting that in the case of planar annihilation configuration, the magnitude of pressure variation remained consistent whether completely non-reflecting outlets or imposed P_0 at infinity was used.

Analysis: 1D Planar flames' annihilation

Figure 5.9 illustrates the temporal evolution of pressure fluctuations and the total heat release rate during the annihilation of planar flames for F $\longrightarrow$ P chemistry at $Le = 1$. The following observations, consistent with the findings in [101], can be made:

- Pressure fluctuations during the extinction event initially rise to a peak pressure and then swiftly decline to reach a steady-state value.
- The total heat release rate (HRR) exhibits a similar trend, indicating that the flame consumption speed increases (flames accelerate) just before the collision of

the two flames.

- Pressure fluctuations at the center X_c and X_r have nearly identical amplitude variations, highlighting that the amplitude decay in 1D is solely attributable to viscosity effects.

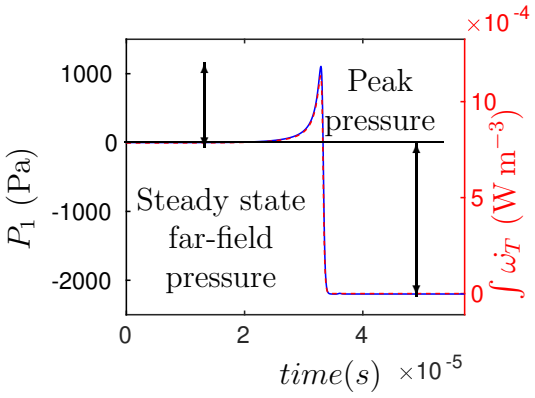

(a) Pressure fluctuation in the center (X_c) and the total heat release rate

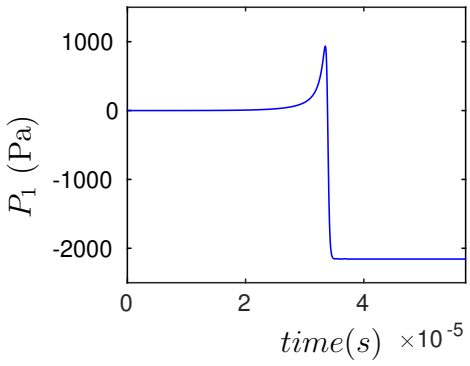

(b) Pressure fluctuation at X_r at $x = 9\delta_T$ from the center

Figure 5.9: Evolution of pressure fluctuations (blue) and the total heat release rate (red) for F $\longrightarrow$ P chemistry at $Le = 1$ for planar flame annihilation.

In line with the idea that pressure fluctuations (sound generation) are solely driven by variations in heat release rate, Talei et al. [100] derived a simplified analytical expression to predict the 'steady-state far-field pressure' as follows:

$$P_f = -\rho_f c_b \left(1 - \frac{T_f}{T_b}\right) S_l \tag{5.13}$$

Remarkably, this expression provides accurate approximation of the simulated 'steady-state far-field pressure' even when considering diverse and complex chemistry scenarios. Consequently, in an effort to streamline our results and facilitate comparisons with the analytical expression, we will normalize the pressure fluctuations P_1 by P_f moving forward.

Furthermore, to enable a consistent comparison of flame acceleration, we will depict the temporal evolution during annihilation starting from when the flame is at a distance of 2 δ_T from the center. We introduce a time normalization factor $\tau = \frac{t}{t_{\text{ref}}}$, where the characteristic time $t_{\text{ref}} = \frac{\delta_T}{S_l}$ represents the time it takes for the laminar flame to traverse a distance of δ_T. This normalization enables us to align the temporal evolution of flames in various scenarios for meaningful comparisons.

Analysis: Circular flame implosion

Figure 5.10 illustrates the temporal evolution of pressure fluctuations and the total heat release rate during the implosion of circular flames for F $\longrightarrow$ P chemistry at $Le = 1$. The following observations can be made:

- The pressure fluctuations and heat release rate fluctuations in circular flames resemble the pressure fluctuations observed in acoustically excited flames (Fig. 5.6c).
- In contrast to the planar flame configuration (Fig. 5.9a), the total heat release rate (HRR) gradually decreases due to the reduction in flame surface area as the flame converges. This decrease in flame surface area likely contributes to the smaller amplitude pressure variations in circular flames, with the trend continuing to even smaller variations in spherical flames as observed in [101].
- Pressure fluctuations at X_r have significantly decreased from their initial values at X_c, primarily due to the decay of amplitudes associated with the monopolar sound sources observed in two-dimensional simulations (Fig. 5.3b).

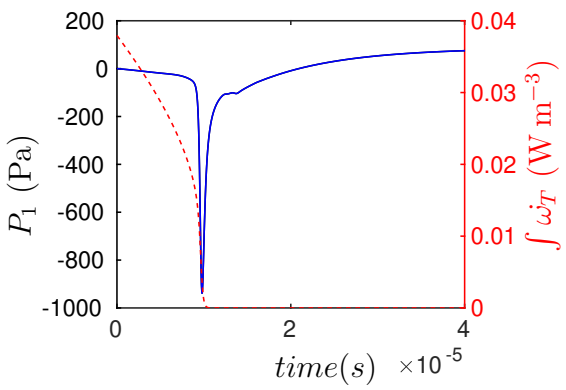

(a) Pressure fluctuation in the center (X_c) and the total heat release rate

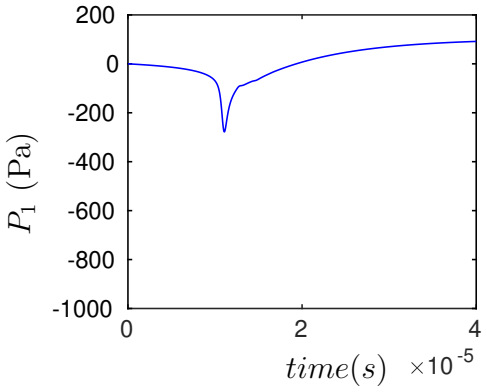

(b) Pressure fluctuation at X_r at $x = 9\delta_T$ from the center

Figure 5.10: Evolution of pressure fluctuations (blue) and the total heat release rate (red) for F $\longrightarrow$ P chemistry at $Le = 1$ for circular flame implosion.

Finally, unlike the planar flame configuration, the expression to approximate the pressure variation for circular flame implosion is more complex [100], and involves significant assumptions and requires numerical integration. Consequently, performing consistent comparisons with simulations is not feasible at this juncture. Therefore,

for circular flame implosion, we directly provide the amplitude of pressure variation in pascals without any normalization. Nevertheless, the time normalization remains consistent with the planar flames for a meaningful comparison.

5.3.3 Effect of Lewis Number

Before investigating the sound generation by hydrogen flames, it is crucial to examine and introduce the impact of Lewis numbers on sound generation in a generalized case. In this section, we investigate the influence of Lewis numbers using the F $\longrightarrow$ P model, akin to the research conducted by Talei et al. [102]

Figure 5.11a presents the temporal evolution of the pressure in the center (X_c) for Lewis numbers $Le = 0.5, 1.0, 2.0$ for planar flames' annihilation. Consistent with the findings of Talei et al. [102], we observe that when $Le \ll 1$, the generated pressure wave smoothly relaxes towards the far-field pressure, and notably, no peaks in pressure fluctuations are observed.

However, when $Le \geq 1$, we observe a notable increase in the pressure fluctuation initially, characterized by a prominent peak that increases with Le, followed by a rapid drop towards the steady-state far-field pressure.

The generation of high amplitude pressure peaks in cases where $Le \geq 1$ has been attributed to the preheating of fresh gases caused by the thicker thermal diffusion layer compared to the mass diffusion layer. This preheating phenomenon results in enhanced reactivity. On the other hand, when $Le < 1$, the absence of pressure peaks can be attributed to a thicker mass diffusion layer, which depletes the reactants before the arrival of the maximum reaction rate. It was also seen that the maximum heat release rate decreases during the final stages of this interaction. Consequently, the reduced reactivity in this scenario mitigates the occurrence of significant pressure fluctuations.

Figure 5.11b further illustrates this phenomenon by depicting the evolution of progress variable of temperature $\theta(T)$ (dashed) and the reactant $\theta(Y_f)$ (solid) at X_c. It can be clearly seen that:

- In cases where $Le > 1$, the temperature profiles lead the reactant profiles, whereas in cases where $Le < 1$, the reactant profiles lead the temperature profiles. This behavior is consistent with the differences in the thickness of the thermal and mass diffusion layers.

- The interaction between the two flames begins earlier when $Le \neq 1$, indicating an earlier onset of flame annihilation.

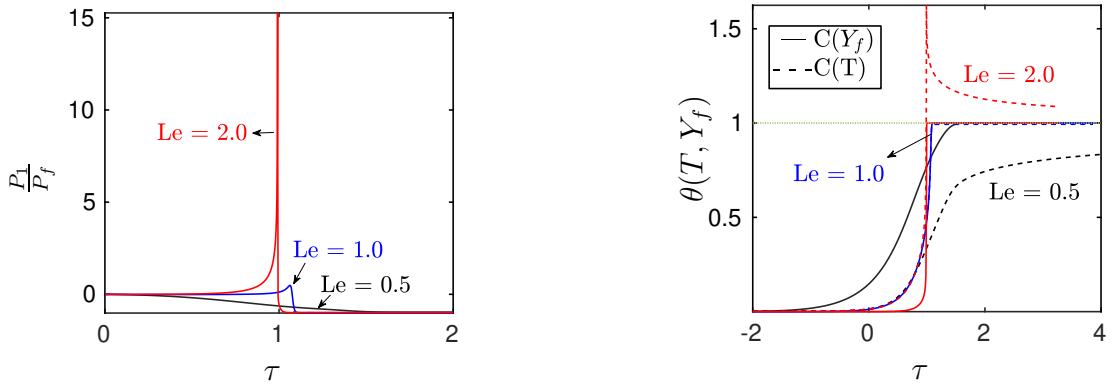

(a) Normalized pressure fluctuations

(b) Progress variables

Figure 5.11: Effects of Lewis number: Evolution in the center (X_c) during the planar flame annihilation for different Lewis numbers

- For cases where $Le > 1$, the burnt temperature at the end of annihilation exceeds the adiabatic temperature. Conversely, for cases where $Le < 1$, the burnt temperatures are lower than the adiabatic temperature.
- In cases where prominent pressure fluctuation is generated, it can be observed that the complete annihilation of the flame occurs much earlier, indicating an increase in the flame propagation speed.

Figure 5.12 illustrates the influence of Lewis numbers on circular flame annihilation. As observed, when $Le \ll 1$, no distinct peak is generated, whereas for $Le \geq 1$, sharp peaks emerge. It is noteworthy that, due to their substantial amplitude of pressure variation, the plot for $Le = 2.0$ is presented on the right axis in figure 5.12a for clarity. It is essential to acknowledge that such large pressure variations, reaching 1×10^4 Pa, are likely achievable only with simplified chemistry models like the one employed in our study and may not accurately represent physical behavior.

Additional insights from Talei et al. [101]

In addition to the influential factors like Lewis numbers and geometry, Talei et al. [101] conducted a comprehensive parametric study on sound generation using a simplified chemistry model. Some of the key insights from their work include:

- For the planar annihilation, they observed that flame thickness has a negligible impact on steady-state far-field pressure. However, in cases of axisymmetric (cir-

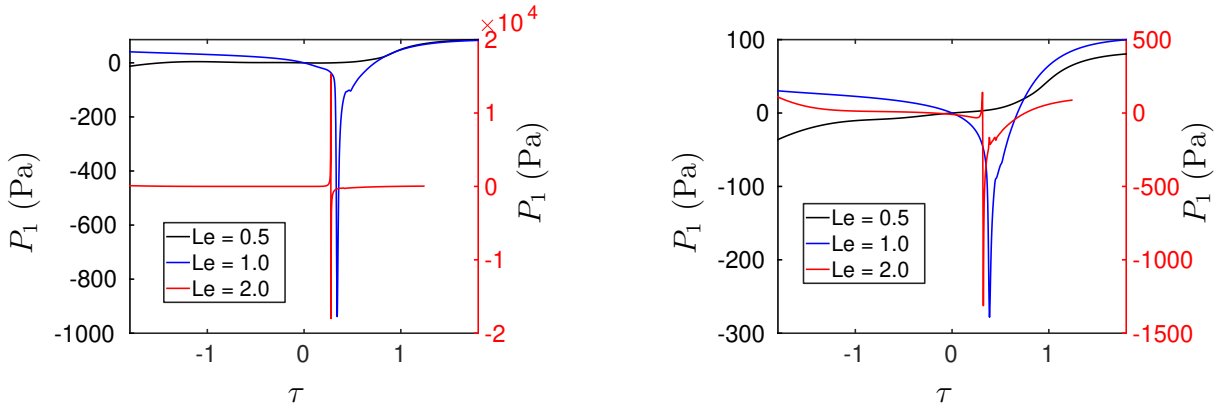

(a) Pressure fluctuations at X_c

(b) Pressure fluctuations at X_r

Figure 5.12: Effects of Lewis number: Evolution in the center (X_c) and at X_r during circular flame implosion for different Lewis numbers.

cular in our context) and spherical flames, far-field pressure was found to depend on flame thickness.

- Through extensive parametric studies involving variations in laminar flame speed (S_l), thermal expansion ratio (T_b/T_f), Zel'dovich number (β), and flame thickness (δ_T), they proposed a scaling relationship of the form for the steady state far-field pressure in 1D and the amplitude of pressure peaks in 2D and 3D:

$$\frac{p_1}{\rho_f c_f^2} \sim -\left(\frac{S_l}{c_f}\right)^{1+\frac{n}{2}} \left(\frac{\delta_T}{x}\right)^{\frac{n}{2}} \left(1-\frac{T_f}{T_b}\right) \left(\frac{T_b}{T_f}\right)^{\frac{2-n}{4}} g\left(\frac{T_b}{T_f}, \beta, Le, x, t, n\right) \tag{5.14}$$

Here, x represents the position of the pressure sensor, and the value of n varies (0, 1, or 2) depending on whether it's a planar flame annihilation, circular flame, or spherical flame implosion. The function g encapsulates the influences of Lewis number, Zel'dovich number, and position x.

5.4 Sound generation by Hydrogen flames

In this section, we aim to build upon the insights obtained from our previous section and previous studies [100, 101]. We will strive to investigate and potentially classify sound generation caused by hydrogen flames.

5.4.1 Effect of Chemistry

Before delving into the magnitude of sound generation by hydrogen flames, it is crucial to analyze the effect of employing simple chemistry models. We follow the methodology proposed by Jiménez et al. [49], who conducted a comparison of sound generation by planar flames using both a simple chemistry model (1S-H_2-Air) and a full chemistry model:

- 1S- H_2-Air model

  In this model, adopted from [49], a single-step irreversible reaction of Hydrogen oxidation is considered.

  $$H_2 + \tfrac{1}{2}\, O_2 \longrightarrow H_2O$$

  Unlike the F $\longrightarrow$ P model, we leave the formation enthalpies and heat capacities unchanged and calculate them using NASA polynomials. Mixture-averaged diffusion coefficients for each species, computed using CANTERA [43], are used in the transport equations. We ensure that the burnt temperature (T_b) and laminar flame speed (S_l) correspond to the detailed chemistry simulations.

  The molar reaction rate for this simple chemistry is given by the Arrhenius law as:

  $$\dot{\omega} = A[H_2][O_2]\, \exp(-T_a/T),$$

  where [] represents the species molar concentration, and T_a is the activation temperature. More details about this one-step chemistry can be found in [49].

- Detailed H_2-Air chemistry

  Despite being referred to as a detailed mechanism, it is actually a 12-step skeletal mechanism [9]. However, it has been shown to accurately reproduce the extinction phenomenon and performs well under elevated pressures. This chemical mechanism consists of 9 species with mixture-averaged diffusion coefficients estimated using the CANTERA library [43]. Reaction parameters for each elementary reaction follow [113].

Jiménez et al. [49] primarily focused on the planar case and made an interesting discovery regarding the influence of chemistry models. They found that when $Le > 1$, the steady-state far-field pressure remained relatively consistent between different

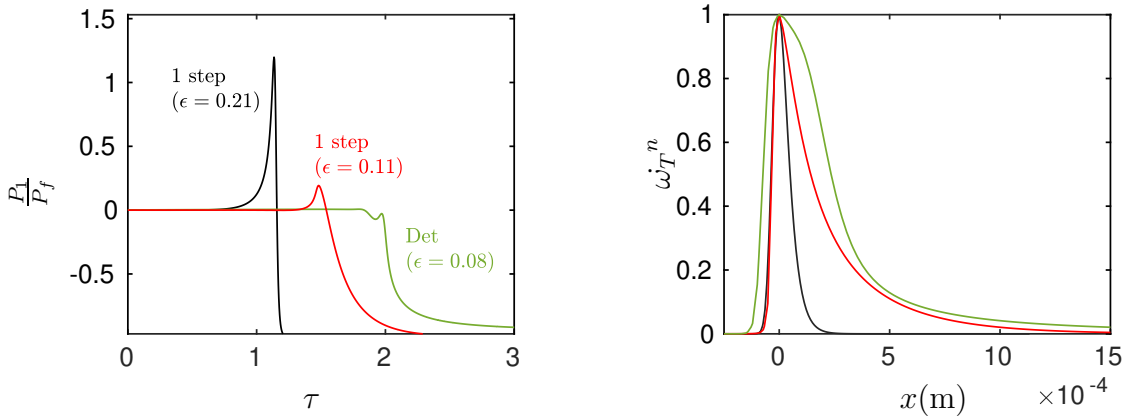

(a) Normalized pressure fluctuations (b) Normalized HRR profiles

Figure 5.13: Effect of chemistry: ***(a)*** Evolution of pressure during planar flame annihilation for unmodified 1S-H_2-Air (black), modified 1S-H_2-Air (red) and detailed (green) chemistry at equivalence ratio $\phi = 3.0$. ***(b)*** Normalized HRR profiles illustrating the differences of flame thickness between these chemistry models.

chemistry models. However, a notable disparity appeared in the peak pressure. To investigate this further, we specifically examine the case at $\phi = 3.0$ where $Le \gg 1$.

In Figure 5.13, we illustrate the pressure fluctuations in the center and the normalized heat release rate profiles for both the simple and detailed chemistry models at $\phi = 3.0$. The significant spike in peak pressure observed in the simple chemistry model, consistent with the findings of Jiménez et al. [49], Talei et al. [101] was observed to primarily arise from the inherent nature of customizing simple chemistry models. These models typically involve matching only the laminar flame speed and adiabatic burnt temperatures to the full chemistry, while the thermal flame thickness δ_T is often not precisely fitted – illustrated by the HRR profiles shown in Figure 5.13b.

Our observations indicate that, in the planar case, the absolute value of the thermal flame thickness δ_T has no significant effect on the peak pressure. Instead, the crucial factor influencing the amplitude of this peak is the ratio between the diffusive flame thickness δ_D and the thermal flame thickness δ_T, denoted as ϵ which when modified, can lead to similar pressure peak values (as indicated by the red curve).

In contrast, when analyzing circular flame implosion, as depicted in Figure 5.14, we find that the unmodified simple chemistry model still significantly over-predicts the pressure peak amplitude. However, in this geometry, it is essential to note that both the absolute value of the thermal flame thickness and the distance of propagation x play vital roles (5.14), further highlighting the potential for misleading results when utilizing simple chemistry when studying sound generation phenomenon.

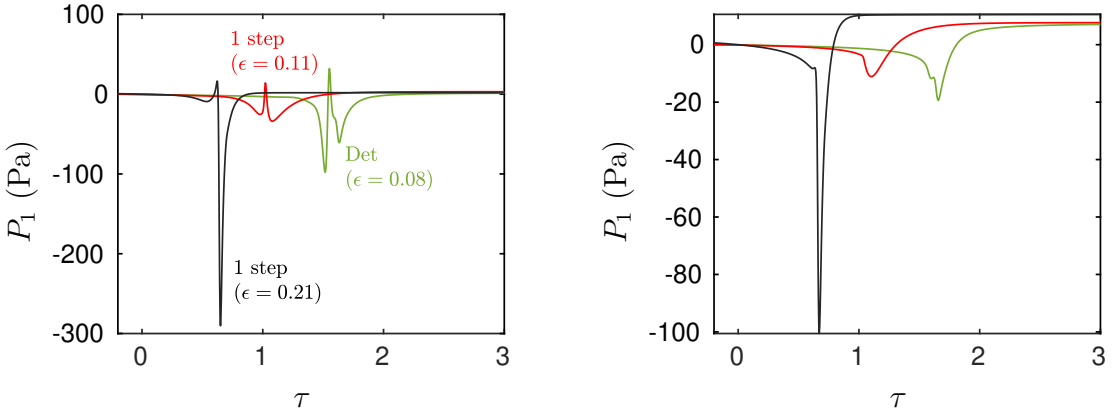

(a) Pressure fluctuations at X_c

(b) Pressure fluctuations at X_r

Figure 5.14: Effect of chemistry: Evolution of pressure during circular flame annihilation for unmodified 1S-H_2-Air (black), modified 1S-H_2-Air (red) and detailed (green) chemistry at equivalence ratio $\phi = 3.0$.

5.4.2 Parametric study of sound generation by hydrogen flames

Having established that the effects of chemistry are primarly associated with the deviation of ϵ, in this section, we explore the influence of the Lewis number (Le) and ratio of diffusive to thermal flame thickness (ϵ) on the amplitude of sound generation considering detailed chemistry model, specifically in the case of circular hydrogen flame implosion.

These factors, although critical, are not explicitly considered in the scaling law eq. (5.14) as presented by Talei et al. [101]. By manipulating the equivalence ratio, serving as a proxy for the Lewis number [5, 49], and the ambient pressure, acting as a proxy for either ϵ or Zel'dovich number β, we aim to demonstrate how deviations in the predictive accuracy of the scaling law eq. (5.14) emerge in comparison to simulations. This approach allows for comprehensively evaluating the influence these two factors play on the generation of sound, while also simultaneosuly allowing us to assess the ability and limitations of the scaling law to accurately predict sound generation.

Varying Equivalence ratio: Effect of Lewis number

The laminar flame speed significantly influences the amplitude of sound generated; hence, the amplitude peaks near an equivalence ratio of $\phi = 1.5$, as evidenced in both simulations and scaling law (fig.5.15). While the scaling law eq. (5.14) effectively predicts the qualitative trend, it tends to underestimate the magnitude as the equivalence ratio – and consequently, the Lewis number – increases. Nevertheless, it is noteworthy

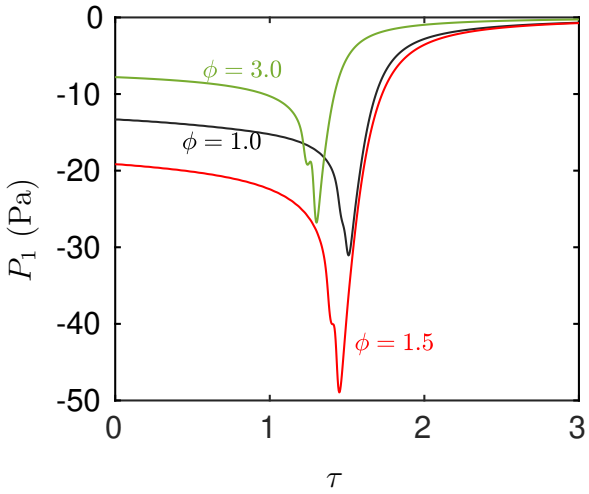

(a) Pressure fluctuations at X_r across various equivalence ratios

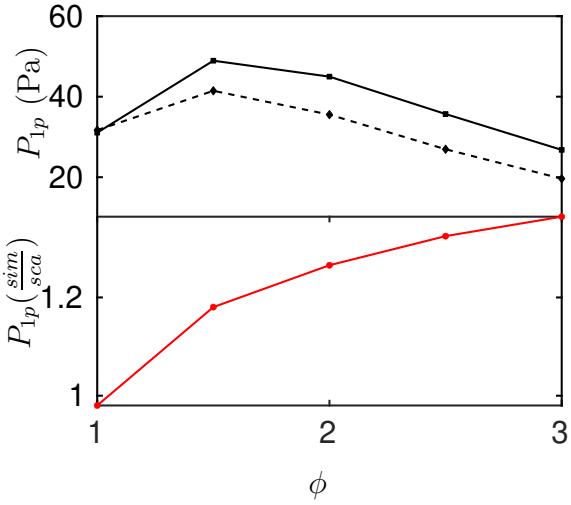

(b) Comparative Analysis of Pressure Peak Magnitudes: Simulations (solid lines) versus Scaling Law (5.14) (dashed lines). The red curve represents the ratio of simulated pressure fluctuation magnitudes to those predicted by scaling laws.

Figure 5.15: Influence of the Lewis Number on Scaling Law Predictions: This figure demonstrates how varying equivalence ratios (Lewis number) affect the predictive accuracy of the scaling law (5.14).

that the qualitative trend remains remarkably consistent.

Varying ambient pressure : Effect of ϵ

Considering that elevated ambient pressures are known to result in decreased laminar flame speeds and and thinner thermal flame layers, it is of significant interest that such conditions, characterized by denser fluids, lead to the generation of higher sound amplitudes. This phenomenon aligns with the predictions made by the scaling law in eq. (5.14). Correspondingly, a series of parametric simulations were conducted, focusing on the implosion of circular hydrogen-air flames under varying operating pressures, with an equivalence ratio set at $\phi = 1.5$. These simulations are detailed in Fig. 5.16a.

One striking finding from these simulations is that, at an operating pressure of 10 atm, the implosion event of a circular hydrogen-air flame induces a pressure peak of 500 Pa at a distance of 9 δ_T from the center of annihilation. This substantial pressure peak equates to an impressive 148 dB on the Sound Pressure Level (SPL) scale, highlighting the significant sound generation potential under such conditions.

However, upon comparing the magnitude of pressure peaks derived from the scaling law eq. (5.14) with those obtained from the simulations (as depicted in Fig. 5.16b), it is observed that the scaling law consistently underestimates the sound magnitude at increased pressures. Furthermore, plotting the ratio of simulated pressure fluctuation magnitudes to those predicted by the scaling laws a clear trend of increasing deviation is observed. Computations revealed that the value of ϵ also follows a similar trend to the deviation in the accuracy of scaling law, highlighting the need to integrate the effects of ϵ into future scaling law formulations.

5.4.3 Pressure peaks in Planar flame Annihilation

In this section, we investigate the influence of equivalence ratio (Lewis number) and elevated pressures (ϵ) in the context of planar flame annihilation.

Effect of Lewis number: 1S-H_2-Air Model

Figure 5.17 illustrates the temporal evolution of normalized pressure fluctuations and temperature profiles in the center during the planar flame annihilation process. We consider four different equivalence ratios: $\phi = 0.5, 1.0, 1.5$, and 3.0.

It is evident that equivalence ratios of $\phi = 0.5$ and 1.0 do not exhibit any spikes in pressure fluctuations, and the temperature at the end of annihilation remains lower than the adiabatic temperature. In contrast, for $\phi = 1.5$ and 3.0, noticeable peaks are

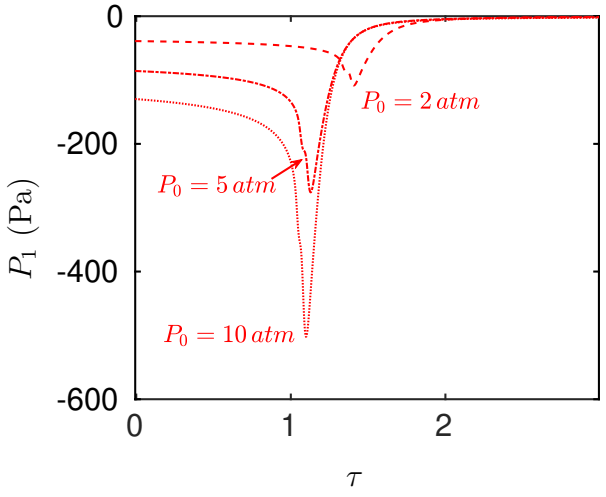

(a) Pressure fluctuations at X_r at different ambient pressures.

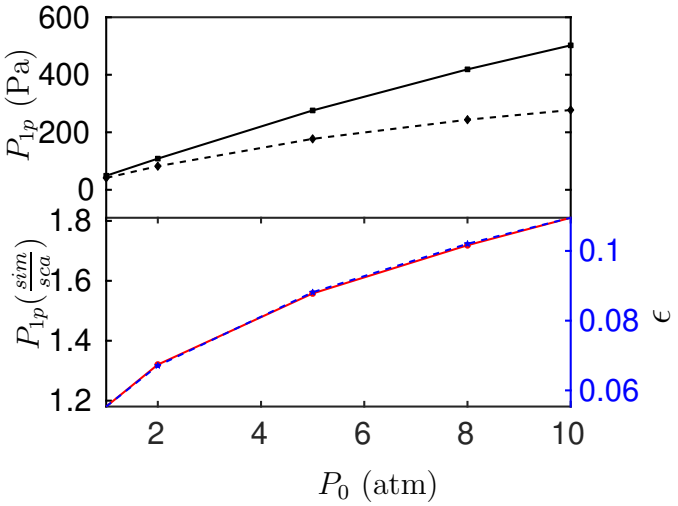

(b) Comparison of Pressure Peak Magnitudes: Simulation Results (solid lines) Against Scaling Law (5.14) (dashed lines). The red curve illustrates the ratio of simulated to scaling law-predicted pressure fluctuation magnitudes, while the blue curve depicts ϵ – the ratio of diffusive to thermal flame thickness.

Figure 5.16: Influence of ϵ on Scaling Law Predictions: This figure demonstrates how varying ambient pressure ($\sim \epsilon$) increases the amplyude of sound generation and also how it affects the predictive accuracy of the scaling law (5.14).

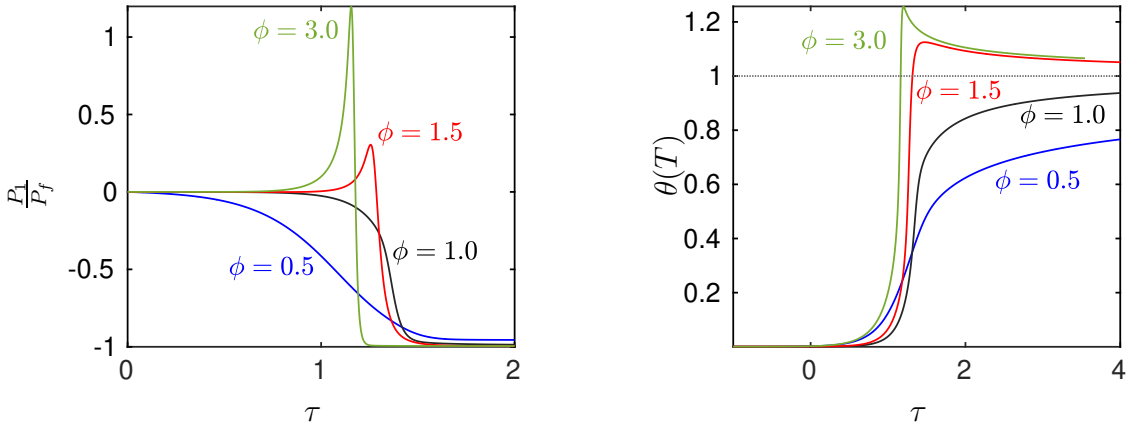

(a) Normalized pressure fluctuations

(b) Progress variable of temperature

Figure 5.17: Evolution in the center (X_c) during flame annihilation for 1S-H_2-Air chemistry for different equivalence ratios: $\phi = 0.5$ (blue), $\phi = 1.0$ (black), $\phi = 1.5$ (red) and $\phi = 3.0$ (green).

observed in both pressure fluctuations and temperature profiles during annihilation.

To further characterize this behavior, we calculate the effective Lewis number (Le^0_{eff}) using the formula commonly employed in the research community [5, 49]:

$$Le^0_{\text{eff}} = 1 + \frac{(Le_E - 1) + (Le_D - 1) \cdot A}{1 + A}, \tag{5.15}$$

where, $A = 1 + \beta(\phi - 1)$ represents a measure of the mixture's strength, where β is the Zel'dovich number. Le_E and Le_D correspond to the Lewis numbers of the excess and deficient reactants, H_2 and O_2, respectively, when $\phi > 1$.

However for $\phi = 1.0$, we obtain an effective Lewis number of $Le_{\text{eff}} = 1.12$, which is in contradiction to the observations in Figure 5.11b, where during annihilation, burnt temperatures are higher than adiabatic temperature for $Le \geq 1$ and lower for $Le < 1$. Consequently, we conclude that for $\phi = 1.0$, the 1S- H_2-Air model effectively results in $Le_{\text{eff}} < 1$, and based on this observation we propose a new normalization of the effective Lewis number (Le^n_{eff}) based on the number of moles diffusing into one another:

$$Le^n_{\text{eff}} = \frac{X_F + X_O}{\frac{X_F}{Le_O} + \frac{X_O}{Le_F}}, \tag{5.16}$$

where X_O & X_F are the molar fractions of the oxidizer and fuel, respectively. The values of both the effective Lewis number formulations for H_2-Air are depicted in Fig-

ure 5.18.

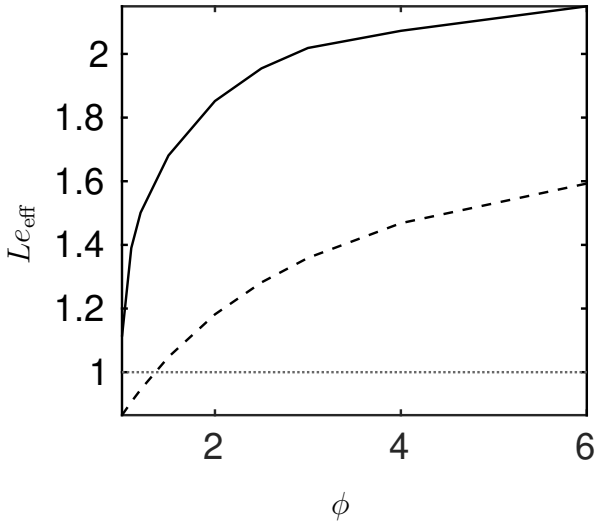

Figure 5.18: Different approximations of Le_{eff} for H_2-Air combustion. The solid line denotes Le^0_{eff} calculated using (5.15) and the dashed line is the newly proposed effective Lewis number Le^n_{eff} computed using (5.16).

Effect of Lewis number: Detailed H_2-Air model

Next, we investigate the influence of equivalence ratio using the detailed H_2-Air model. Figure 5.19b once again displays the same trend observed in the 1S-H_2-Air model. For $\phi = 0.5$ and 1.0, the temperature at the end of annihilation remains lower than the adiabatic temperature, while for $\phi = 1.5$ and 3.0, it exceeds the adiabatic temperature. This behavior aligns with the newly proposed effective Lewis number formulation, providing further support for its validity in this particular scenario.

Furthermore, the discrepancy in the nature of pressure peaks between the single-step and detailed chemistry models, as discussed earlier, can be attributed to the variation of ϵ between the two models.

Parametric studies on planar hydrogen flame annihilation

Figure 5.20 provides valuable insights into the impact of equivalence ratio (ϕ) and ambient pressure (P_0) on sound generation using the detailed chemistry model

- At an equivalence ratio of $\phi = 1.2$ and an ambient pressure of $P_0 = 6$ atm, no pressure peak is generated.

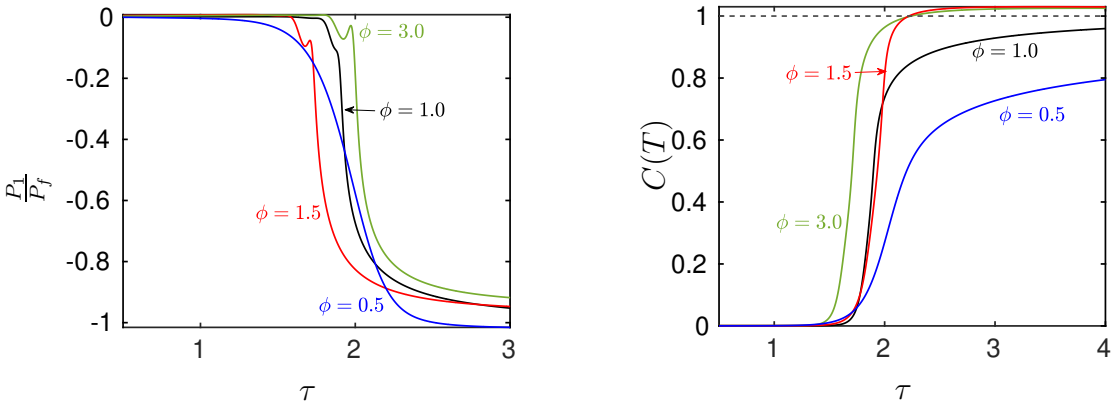

(a) Normalized pressure fluctuations (b) Progress variable of temperature

Figure 5.19: Evolution in the center (p_c) during flame annihilation for Detailed-H_2-Air chemistry for different equivalence ratios: $\phi = 0.5$ (blue), $\phi = 1.0$ (black), $\phi = 1.5$ (red) and $\phi = 3.0$ (green) at 1 atm.

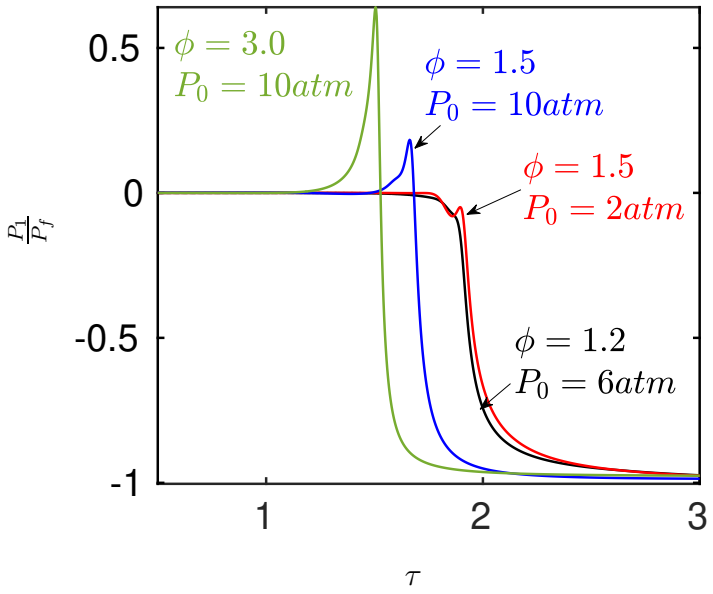

Figure 5.20: Evolution of normalized pressure fluctuations in the center (p_c) during 1D flame annihilation for detailed H_2-Air chemistry at different equivalence ratios and ambient pressures. The peak generated at $\phi = 1.5$ and $P_0 = 2$ atm is considered "secondary".

- For $\phi = 1.5$, small "secondary" pressure peaks can be observed at relatively low ambient pressures of $P_0 = 2$ atm. Here, "secondary" peaks refer to peaks that exist but have lower amplitudes compared to P_0.
- Comparing cases of $\phi = 1.5$ at different ambient pressures ($P_0 = 10$ atm and $P_0 = 2$ atm), it becomes evident that an increase in the equivalence ratio (ϕ) leads to higher pressure peak amplitudes. This behavior is linked to the increase in the effective Lewis number (Le_{eff}) as the mixture becomes richer, as indicated in Figure 5.18.
- Furthermore, when comparing cases of $\phi = 1.5$ at different ambient pressures ($P_0 = 2$ atm and $P_0 = 10$ atm), it is apparent that an increase in ambient pressure (ϵ) results in a significant increase in pressure peak amplitude, with the peaks even transitioning from secondary to primary.

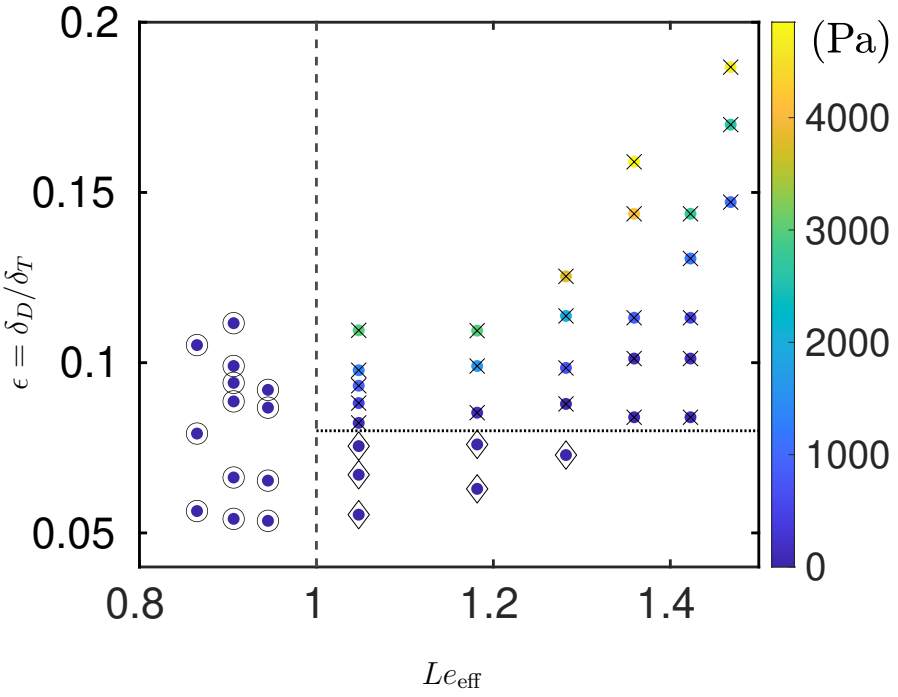

Figure 5.21: Demarcation of regions depicting the generation of peak pressures (or lack of) based on the Le^n_{eff} criteria. The variation in the amplitude of generated peak pressures due to ϵ is also shown. Crosses (Circles) represent the generation (lack of) of pressure peaks during annihilation. Diamonds represent the "secondary" peak generation.

Figure 5.21 provides further insights into this relationship, clearly showing that:

- Pressure peaks generated during hydrogen flame annihilation can be categorized based on the newly proposed Le^n_{eff}. Specifically, when $Le^n_{\text{eff}} < 1$, no pressure peaks are observed. Conversely, pressure peaks are generated when $Le^n_{\text{eff}} > 1$.

- Furthermore, the figure illustrates that as the value of ϵ increases, the amplitude of the generated pressure peaks also increases. This suggests that the ratio between the diffusive and thermal thickness (ϵ) plays a significant role in determining the magnitude of pressure peaks.

In summary, these findings illustrate the interplay among ambient pressure, equivalence ratio, effective Lewis number, and the diffusive and thermal thickness ratio in shaping the generated pressure peaks during planar hydrogen flame annihilation.

Finally, it is essential to reiterate that these observations exclusively pertain to the behavior of pressure peaks. The far-field steady-state pressure in planar annihilation, as predicted by Equation (5.13), remains relatively unaffected by variations in the Lewis number and the ratio of diffusive to thermal flame thickness (ϵ).

5.5 Conclusion

In this chapter, we demonstrated the dissipative and isotropic properties of our Hybrid LBM solver in the context of acoustic transport. Additionally, using a simple single-step chemistry model, we have identified the principal mechanisms of sound generation during combustion processes, namely Pinch-off and Flame Annihilation. Building upon the insights from Talei et al. [102], we also examined the influence of the Lewis number on sound generation.

Additionally, by transitioning to hydrogen fuel, we highlighted potential limitations of simple chemistry models, particularly their tendency for severe over-prediction due to inadequate representation of flame thickness. Moreover, we delved into the effects of the Lewis number and introduced a new term, ϵ, which denotes the ratio of diffusive to thermal flame thickness. This aspect was crucial in understanding the limitations of chemistry models on sound generation. Our analysis also extended to the exploration of the predictive capabilities of scaling laws proposed by Talei et al. [101].

Our extensive simulations conclusively demonstrated that the intensity of sound generation is primarily dependent on the laminar flame speed. Specifically, in Hydrogen-air combustion, we highlighted that the maximal sound production occurs near an equivalence ratio of $\phi = 1.5$. Moreover, we established that increasing ambient pressure amplifies the sound generated, a critical consideration for designing burners.

Furthermore, we investigated how the ratio ϵ and the Lewis number influence the amplitude of the pressure peak in planar annihilation scenarios. Observing variations in the adiabatic burnt temperature during annihilation, we proposed a new formulation of the effective Lewis number, which aligns well with both simple and detailed chemistry models. Utilizing this new formulation, we successfully delineated distinct regions of pressure peak generation in planar annihilation cases.

In summary, this chapter validates the dissipative and isotropic capabilities of our solver and corroborates the phenomenon of sound generation based on prior insights, while also delving into the complexities of sound generation in hydrogen-fueled scenarios.

Chapter 6

Large Eddy Simulation of PRECCINSTA Burner

Contents

6.1 Introduction 121

6.2 Filtered LES Equations for Reactive Flows 123

6.2.1 Closure Models 123

6.3 Preccinsta burner 126

6.3.1 Numerical Setup 127

6.4 Non-Reacting case 129

6.5 Reacting case 130

6.5.1 Quiet case ($\phi = 0.83$) 130

6.5.2 Pulsating case ($\phi = 0.7$) 133

6.6 Heat Losses 140

6.7 Summary 142

6.1 Introduction

Turbulent combustion processes stand at the heart of various practical systems, including industrial burners, rocket engines, and aircraft engines. These systems, characterized by high Reynolds numbers, present a multitude of challenges, ranging from managing thermoacoustic instabilities arising from the interplay of acoustic waves and

unsteady heat release – to navigating the complexities of chemical reactions within turbulent flows. In this landscape, the need for cost-efficient yet accurate computational methods becomes paramount. This is where the Lattice Boltzmann Method (LBM) comes into play.

Recent investigations into the Lattice Boltzmann method (LBM) have revealed its potential, especially when addressing reactive flows [7, 10, 46, 99]. Yet, much of the existing work, while foundational, has centered on simpler flow scenarios. The broader applications of LBM, encompassing high Reynolds numbers, intricate geometries, and non-uniform grids in reactive flows, remain less explored [47, 103]. This chapter seeks to bridge this gap by directing its focus on the detailed simulation of the PRECCINSTA burner [73, 90]. Representing micro gas Turbine (mgT) burners prone to thermoacoustic instabilities, the PRECCINSTA burner – short for "PREdiction and Control of Combustion INSTAbilities" – serves as a valuable benchmark. By incorporating characteristic boundary conditions, turbulent combustion modeling, and multi-level grid refinements, this study pioneers the use of LBM for predicting thermoacoustic instabilities in intricate burners.

Furthermore, when investigating the characteristics of turbulent combustion, one is confronted with a spectrum of scales, ranging from the largest integral lengths (l_t) to the smallest Kolmogorov scales (η_k). While Direct Numerical Simulations (DNS) serve as the gold standard, capturing the entire spectrum, their high computational cost often renders them impractical for industrial applications [83]. Thus, the search for more practical alternatives leads to two dominant contenders: Reynolds Averaged Numerical Simulations (RANS) and Large Eddy Simulations (LES).

The allure of RANS lies in its computational economy, focusing solely on time-averaged flow attributes. However, this approach limits its effectiveness in handling transient unsteady phenomena effectively. This is where LES excels. Although more computationally demanding than RANS, LES captures the inherent unsteadiness of the flow, making it well-suited for addressing combustion instabilities [83, 90], which is the central focus of this thesis.

Within this context, this chapter aims to validate the Lattice Boltzmann methods in simulating thermoacoustic instabilities in complex, aero-engine-like burners through Large Eddy Simulations. We begin with an introduction to LES governing equations and associated turbulent models in section (6.2), followed by a meticulous exploration of various configurations of the PRECCINSTA burner.

6.2 Filtered LES Equations for Reactive Flows

In Large Eddy Simulations (LES), the larger scale eddies of turbulence are explicitly resolved, while the smaller scales are approximated using subgrid scale closure models. The process involves performing simulations over the filtered form of the Navier-Stokes equations. The spatial LES filter, denoted as F, applied to an arbitrary quantity f, is expressed as:

$$\overline{f}(\boldsymbol{x}) = \int f(\boldsymbol{x'})F(\boldsymbol{x} - \boldsymbol{x'})d\boldsymbol{x'}, \tag{6.1}$$

Following this filtration, the quantity f can be decomposed into filtered $\overline{f}$ (resolved) and residual f' (modeled) components:

$$f = \overline{f} + f'. \tag{6.2}$$

Additionally, when dealing with variable density ρ, a mass-weighted Favre filter $\widetilde{f}$ is introduced [83]:

$$\overline{\rho}\widetilde{f}(\boldsymbol{x}) = \int \rho f(\boldsymbol{x'})F(\boldsymbol{x} - \boldsymbol{x'})d\boldsymbol{x'}, \qquad \overline{\rho}\widetilde{f} = \overline{\rho f}. \tag{6.3}$$

Subsequently, the Favre-filtered NSF equations are expressed as [117]:

$$\frac{\partial \overline{\rho}}{\partial t} + \frac{\partial \overline{\rho}\tilde{u}_\alpha}{\partial x_\alpha} = 0 \tag{6.4}$$

$$\frac{\partial \overline{\rho}\tilde{Y}_k}{\partial t} + \frac{\partial \overline{\rho}\tilde{u}_\alpha \tilde{Y}_k}{\partial x_\alpha} = \frac{\partial \check{J}^k_\alpha}{\partial x_\alpha} + \check{\dot{\omega}}_k \tag{6.5}$$

$$\frac{\partial \overline{\rho}\tilde{u}_\beta}{\partial t} + \frac{\partial \overline{\rho}\tilde{u}_\beta \tilde{u}_\alpha}{\partial x_\alpha} = -\frac{\partial \overline{p}}{\partial x_\beta} + \frac{\partial \check{\tau}_{\alpha\beta}}{\partial x_\alpha} \tag{6.6}$$

$$\frac{\partial \overline{\rho}\tilde{E}}{\partial t} + \frac{\partial \overline{\rho}\tilde{H}\tilde{u}_\alpha}{\partial x_\alpha} = \frac{\partial \check{\tau}_{\alpha\beta}\tilde{u}_\alpha}{\partial x_\alpha} - \frac{\partial \check{q}_\alpha}{\partial x_\alpha} \tag{6.7}$$

Here, the notation $\check{\cdot}$ denotes terms that require further modeling.

6.2.1 Closure Models

- **Vreman Model:**

  The fundamental concept behind Subgrid-Scale (SGS) turbulence models is to account for the impact of unresolved scales (f') on the resolved scales ($\overline{f}$). This

is crucial, as the behavior of these unresolved, smaller scales impact the larger ones through processes like turbulent mixing and energy transfer. The inclusion of these models then enable Large Eddy Simulation (LES) to simulate turbulent flows while only directly resolving larger energy-containing scales.

A variety of subgrid-scale models have been developed, all sharing the common aim of representing the impacts of unresolved turbulence through additional terms that mimic diffusive behavior. These models often involve introducing a turbulent viscosity (μ_t). In our thesis, building upon previous work [22, 48, 103], we integrate our Hybrid LBM model with the Vreman SGS model [111] to address unresolved eddies.

The modeling of the turbulent viscous tensor is expressed as:

$$\check{\tau}_{\alpha\beta} \equiv (\mu + \mu_t)\left(\frac{\partial \tilde{u}_\alpha}{\partial x_\beta} + \frac{\partial \tilde{u}_\beta}{\partial x_\alpha} - \delta_{\alpha\beta}\frac{2}{3}\frac{\partial \tilde{u}_\gamma}{\partial x_\gamma}\right) . \tag{6.8}$$

here the expression for μ_t is given by:

$$\mu_t = \overline{\rho} c \sqrt{\frac{B_j}{\alpha_{\alpha\beta}\alpha_{\alpha\beta}}} \tag{6.9}$$

where the model constant c is related to the Smagorinsky constant C_s as approximately $c \approx 2.5 C_s$, with $C_s = 0.18$. Further details regarding the remaining terms can be found in references such as [22, 104, 111].

From the perspective of the Lattice Boltzmann Method, the incorporation of the SGS model can be simply achieved by modifying the characteristic relaxation time τ in eq.(3.14) as:

$$\bar{\tau} = \underbrace{\frac{\mu + \mu_t}{\rho c_s^2}}_{\tau} + \frac{\Delta t}{2} \tag{6.10}$$

- **Thickened Flame LES Model (TFLES)**

  In the context of Large Eddy Simulation (LES), the thermal flame thickness (δ_T) that defines the reaction zone is often considerably smaller than the mesh resolution (Δx) used in the simulation. This discrepancy often results in the insufficient resolution of the reaction zones, posing a substantial numerical problem. To mitigate this issue, one approach is to artificially increase the flame thickness while retaining the original laminar flame speed (S_l) [12]. .

Following the fundamental laminar premixed theories, the relationship between flame speed and flame thickness can be expressed as follows:

$$s_L \propto \sqrt{\dot{\omega} D}, \qquad \delta_T \propto \sqrt{\frac{D}{\dot{\omega}}}, \tag{6.11}$$

Where, D represents diffusivity, and $\dot{\omega}$ corresponds to the reaction rate. It is apparent from the above relationship that flame thickness can be artificially increased by multiplying the diffusion term and dividing the reaction rate by a thickening factor $\mathcal{F}$:

$$D \to \mathrm{F} D, \qquad \dot{\omega} \to \frac{\dot{\omega}}{\mathcal{F}}, \tag{6.12}$$

which leads to:

$$s_L \propto \sqrt{\dot{\omega} D}, \qquad \delta_T \propto \mathcal{F} \sqrt{\frac{D}{\dot{\omega}}}, \tag{6.13}$$

As a result, the artificially thickened flame ($\mathcal{F}\delta_T$) can now be resolved with larger grid resolutions, all while maintaining the original flame propagation speed. However it is well-known that artificially thickened flame exhibits reduced sensitivity to turbulence [2, 21], which manifests as a decreased level of flame surface wrinkling. To address the reduction in flame surface induced by the thickening process, an efficiency function Ξ was introduced by Colin et al. [21]. In our studies, we adopt the formulation proposed by Charlette et al. [15], wherein Ξ is defined as a sub-grid scale wrinkling factor that quantifies the ratio between the total and the resolved flame surface.

Consequently, the unresolved heat transfer, species diffusion, and chemistry source terms of the filtered LES-NS equations are modeled as

$$\check{q}_\alpha = -\left[\mathcal{S}\mathcal{F}\Xi\lambda + (1-\mathcal{S})\left(\lambda + \lambda_t\right)\right] \frac{\partial T}{\partial x_\alpha} + \sum_{k=1}^{\mathrm{N_{sp}}} h_k \check{J}_\alpha^k \tag{6.14}$$

$$\check{J}_\alpha^k = \left[\mathcal{S}\mathcal{F}\Xi + (1-\mathcal{S})\left(1 + \frac{\mathcal{D}_{k,t}}{\mathcal{D}_k}\right)\right] J_\alpha^k \tag{6.15}$$

$$\check{\dot{\omega}}_k = \mathcal{S}\frac{\Xi}{\mathcal{F}}\dot{\omega}_k \tag{6.16}$$

Furthermore, the factor $\mathcal{S}$ functions as a flame sensor, taking a value of one within the flame region and zero elsewhere. In regions outside the flame (i.e., $\mathcal{S} = 0$), this method incorporates sub-grid scale heat diffusion and species diffusion using turbulent conductivity λ_t and turbulent species diffusivity $\mathcal{D}_{k,t}$ via:

$$\lambda_t = \frac{\mu_t c_p}{\mathrm{Pr_t}} \ , \ \mathcal{D}_{k,t} = \frac{\mu_t}{\overline{\rho}\mathrm{Sc_t}} \ , \tag{6.17}$$

Here, $\mathrm{Sc_t}$ and $\mathrm{Pr_t}$ denote the turbulent Schmidt and Prandtl numbers, respectively; which are chosen as 0.7 in our explorations. Inside the flame region ($\mathcal{S} = 1$), the flame thickness is artificially increased by a factor of $\mathcal{F}$ to ensure adequate resolution by the mesh grid. Finally, the sub-grid scale efficiency function Ξ is evaluated as

$$\Xi = \left(\frac{\Delta}{\delta_T}\right)^{\beta_F} \tag{6.18}$$

with Δ representing the LES filter size, typically chosen to be around the thickened flame thickness $\mathcal{F}\delta_t$. The exponent β_f in the above equation can be a fixed constant or determined dynamically (either globally or locally) [110]. For our LES computations of the Preccinsta Burner, we have observed that setting $\beta_F = 0.5$ already yields satisfactory results.

6.3 Preccinsta burner

Swirl combustors have gained significant prominence in industrial burner applications due to their numerous advantages. The incorporation of swirl into combustion processes can lead to a variety of flow patterns, including phenomena such as Central Re-circulation zone (CRZ) and Outer Re-circulation Zones (ORZ), as well as the formation of coherent structures like Precessing Vortex Cores (PVC) [62]. These flow structures play a pivotal role in enhancing flame stability and expanding the flammability limits of the combustion process [83]. A quintessential example of this technology is the Preccinsta burner.

Originating from a collaborative initiative within the European Union, the Preccinsta burner draws its inspiration from an industrial design pioneered by SAFRAN Helicopter Engines. This design closely replicates the intricacies of a genuine aeronautical gas turbine combustor. As illustrated in the figure 6.1, the geometry consists of three main parts: the inlet plenum where the mixture is initially injected, the swirler comprising twelve radial veins connected to a converging nozzle with a central conical bluff body, and the square-section combustion chamber (measuring $86 \times 86\,\mathrm{mm}^2$) with

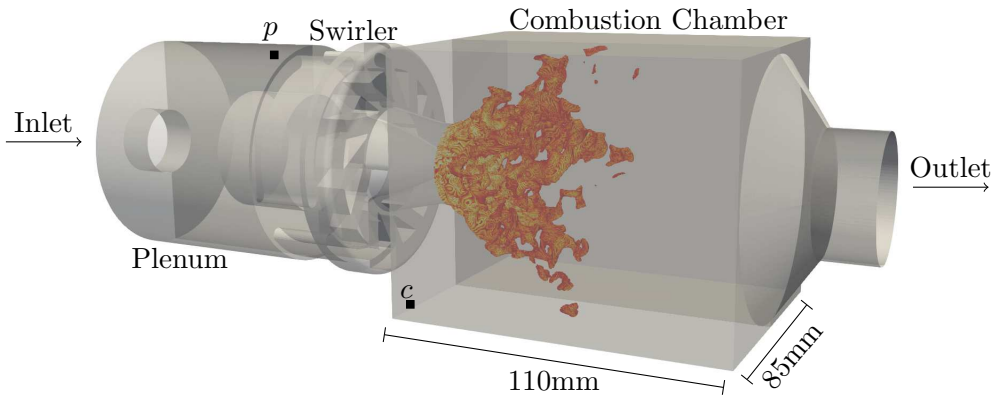

Figure 6.1: Global view of the Preccinsta setup

a length of 110 mm. The burnt gases exit through a cone-shaped exhaust nozzle with a diameter of 39.5 mm.

The Preccinsta burner has been extensively studied both experimentally and numerically and is considered a benchmark test case for reactive Large Eddy Simulation (LES) models. Some key findings from previous studies include:

- Precessing vortex cores (PVC) can be observed in cold flows, but their presence is damped in reacting flows [90].
- Variations in equivalence ratios allow for the transition between quiet and pulsating modes. This significant difference in stability is evident when fuel and air are injected separately [39].
- On the contrary, Volpiani et al. [110] demonstrated that dynamic sub-grid scale efficiency models can reproduce both quiet and pulsating modes of the burner using premixed mixtures at the inlet, eliminating the need for separate fuel injection.
- Additionally, Bénard et al. [6] highlighted that accounting for heat losses on the wall led to improved statistical averages and, notably, more accurate flame shapes and lift-off distances.

6.3.1 Numerical Setup

The global mesh configuration is presented in Figure 6.2. To avoid the need for specifying precise acoustic impedances upstream and downstream of the combustion chamber,

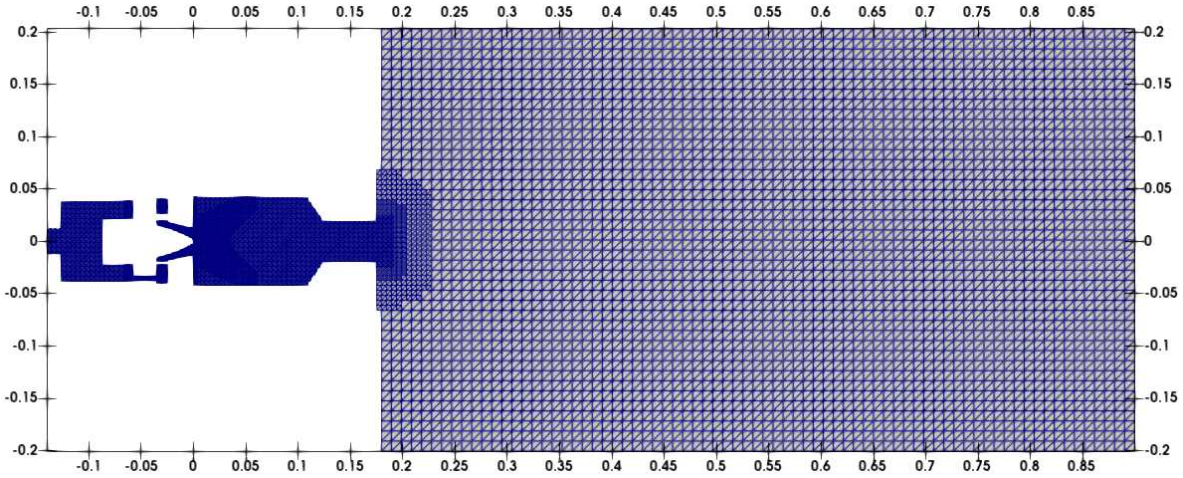

(a) Global Topology

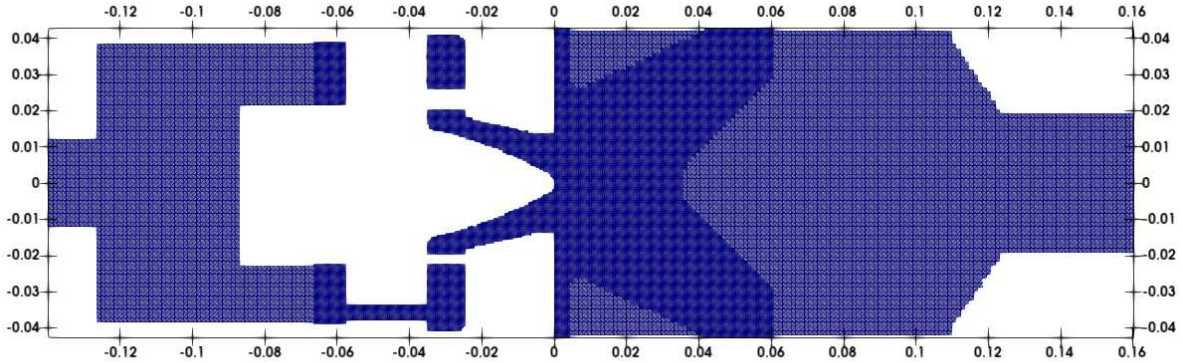

(b) Refinement near the flame region.

Figure 6.2: Mesh configuration along the axis cut-plane.

the swirler and the injector were also included in the mesh. Additionally, the computational domain downstream of the combustion chamber extends to encompass a portion of the external atmosphere. Characteristic boundary conditions, such as the NRI-NSCBC boundary condition (as described in Section 3.4.1), were applied at the inlet, while a non-reflecting outlet boundary with a specified pressure at infinity, as outlined in [82], was employed at the outlet. Additionally, unless specified otherwise, non-slip adiabatic boundary conditions were imposed on the walls of this burner.

Furthermore, a comprehensive grid convergence study, detailed in [117], confirmed that a mesh size with a minimum grid spacing of $\Delta x = 0.3\,\text{mm}$ was sufficient for accurate simulations. This mesh comprised approximately 19.9 million grid points.

In the case of reacting flows, the simulation utilized the two-step methane/air chemical mechanism proposed by Franzelli et al. [39]. This mechanism involves two reactions among six species (CH_4, O_2, CO_2, H_2O, CO, N_2).

6.4 Non-Reacting case

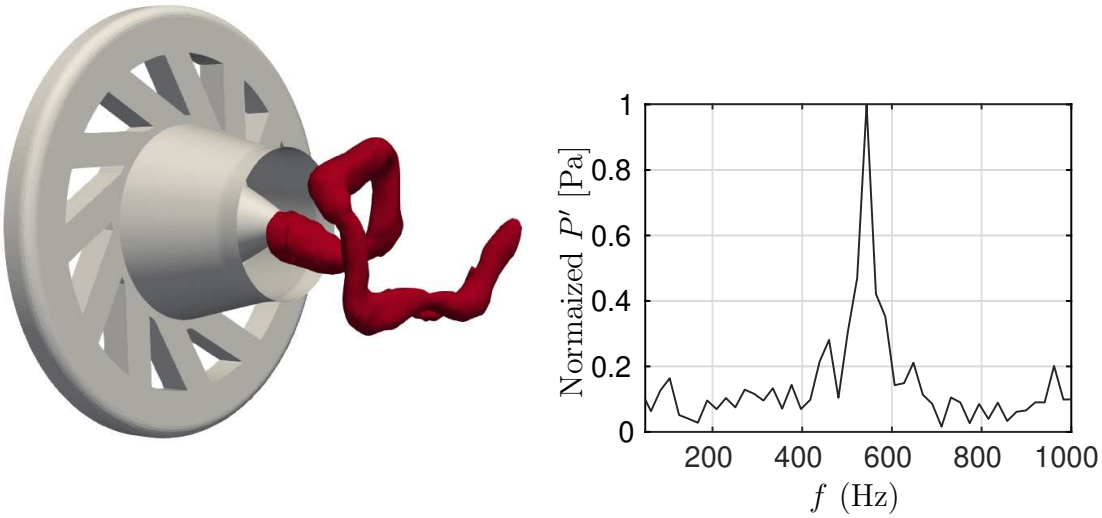

(a) PVC (b) Normalized Pressure fluctuations

Figure 6.3: Illustration of the hydrodynamic instability: **(a)** Precessing Vortex Core (PVC) depicted by the contour of low-pressure. **(b)** Normalized Pressure fluctuation spectrum in this region.

We begin the validation of our LBM-LES code with a simple non-reacting (cold) flow simulation. In this cold flow setup, we impose a mass flow rate of $12\,\text{g}\,\text{s}^{-1}$ of air at a temperature of $T = 300\,\text{K}$ at the inlet, resulting in an average inlet velocity of

$27\,\mathrm{m\,s^{-1}}$.

As previously mentioned, Precessing Vortex Cores (PVC) have been observed in both experiments and numerical simulations [90]. Figure 6.3a provides a snapshot of this large rotating spiral structure around the burner axis. Spectral analysis in this region, as depicted in the 6.3b, reveals that this hydrodynamic structure rotates at a frequency of 542 Hz. This frequency is consistent with the findings of previous numerical studies and experiments [90], which reported frequencies of 540 and 510 respectively.

6.5 Reacting case

After having provided a brief picture of the nature of swirled flows in the cold configuration of Preccinsta in the previous section, this section is dedicated to the validation of the LBM-LES method in the context of the reactive Preccinsta burner. The evaluation begins with an analysis of descriptive statistics in reacting cases and then subsequently considering the pulsating configuration, we aim to demonstrate the method's capability to faithfully reproduce the inherent thermo-acoustic instability of this system. The parameters for the investigated quiet and pulsating cases are detailed in Table 6.1.

Case	ϕ	S_l $(\mathrm{m\,s^{-1}})$	T_{ad} (k)	δ_t (m)	$\mathcal{F}$	Inlet velocity $(\mathrm{m\,s^{-1}})$	P_{th} (kW)
Quiet	0.83	0.3	2058	0.41×10^{-3}	6	24.0	30
Pulsating	0.7	0.2	1847	0.55×10^{-3}	3.5	24.0	25

Table 6.1: Simulation parameters for the quiet and pulsating modes of Preccinsta.

Furthermore, once stabilized, the statistical averages are calculated over 18 cycles of flame characteristic times t_c, where the characteristic convective time $t_c \approx 2ms$ is defined as the ratio of the flame length to the bulk inlet velocity.

6.5.1 Quiet case ($\phi = 0.83$)

Qualitative analysis

By conducting a simple qualitative analysis of the axial cut-plane fields, several important features of this swirled combustor can be observed:

- Figure 6.4a illustrates the presence of the Central Recirculation Zone (CRZ) and the Outer Recirculation Zone (ORZ), both of which are known to play a crucial role in maintaining flame stability and shortening. These images are generated

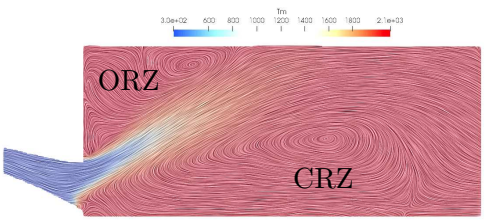

(a) Re-circulation Zones

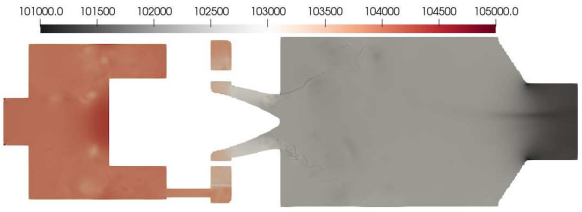

(b) Pressure drop

.

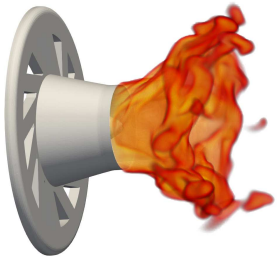

(c) Volume rendering of HRR

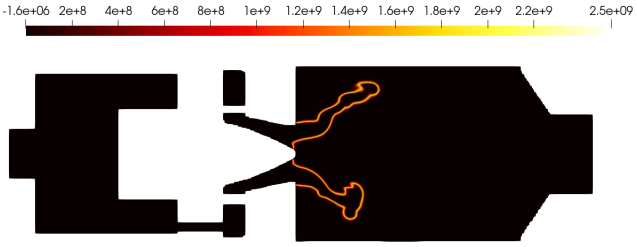

(d) Axial cut-plane illustrating HRR

Figure 6.4: Illustration of Quiet mode of Preccinsta burner

from the surface Line Integral Convolution (LIC) of mean velocity fields and are color-coded by mean temperature.

- Figure 6.4b demonstrates that the pressure drop across the swirler, i.e., between the inlet plenum and the combustion chamber, is recovered.
- Both the 3D iso-volume view rendered by the heat-release rate ($\dot{\omega}_T$) in Figure 6.4c and the axial cut-plane of $\dot{\omega}_T$ in Figure 6.4d reveal an M-shaped flame, which deviates from experimental observations. In the forthcoming sections, we will explore how the adiabatic treatment of the burner walls contributes to this deviation.

Statistical analysis

To perform a quantitative analysis of the flow fields, time-averaged statistics are computed on cut-planes that are orthogonal to the burner axis within the combustion chamber. These quantities are azimuthally averaged at cut-planes located at distances of 6, 10, 15, 20, 30, and 40 mm from the injector exit and the results are presented in Fig. 6.5. When available, experimental measurements are represented by red triangles,

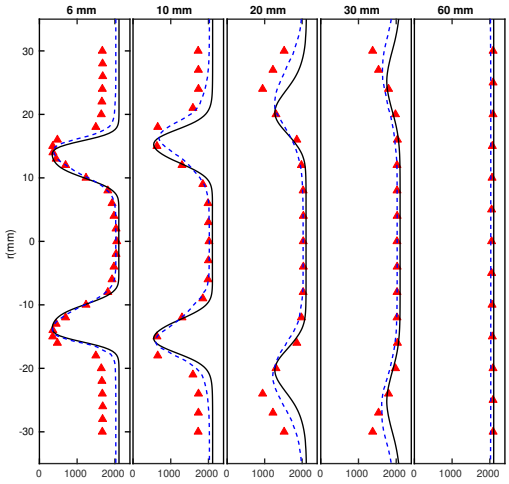

(a) Average Temperature

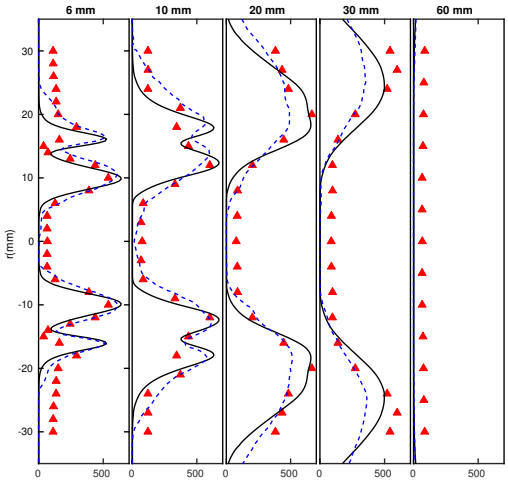

(b) RMS Temperature

.

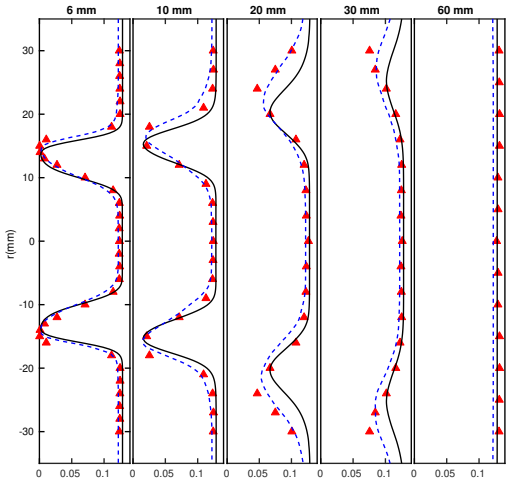

(c) Average CO_2 mass fractions

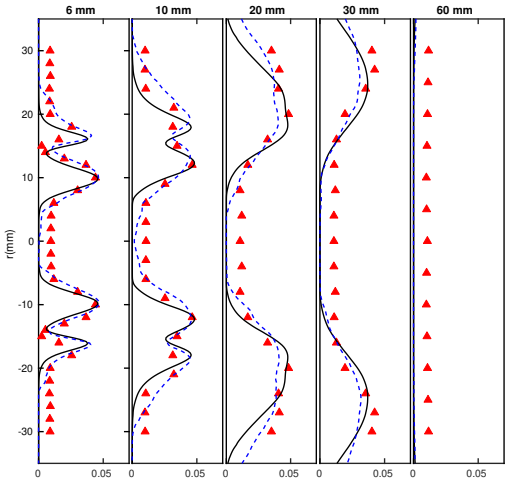

(d) RMS CO_2 mass fractions

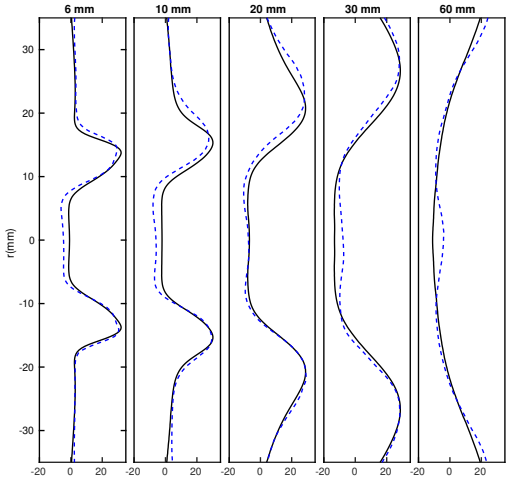

(e) Average Axial velocity

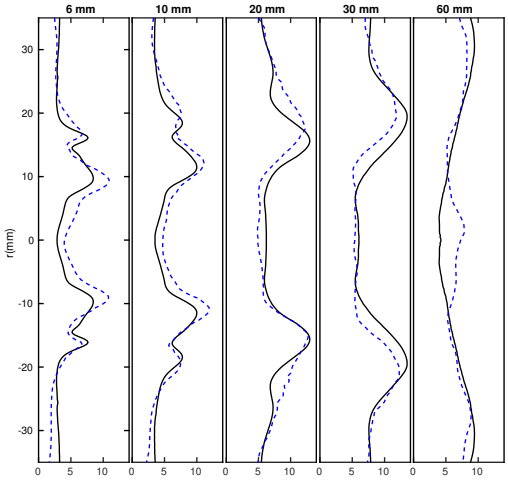

(f) RMS Axial velocity

Figure 6.5: Average and RMS statistics for the Quiet case (tab:6.1). ▬ (experiments [73]), ▬ (Ref. simulation [76]), ▬ (ProLB).

and for reference, results from a previous numerical simulation conducted by Moureau et al. [76] using the YALES2 solver are also included.

Some key observations from the statistical analysis are as follows:

- Within the Central Re-circulation Zone (CRZ), the average temperature profiles and CO_2 mass fractions align closely with the experimental data. However, an absence of fluctuations in the RMS profiles is noted in this region, marking a deviation from experimental findings.
- A quantitative deviation in both the average and RMS of the temperature profiles from experimental observations is noted in the Outer Re-circulation Zone (ORZ).
- Comparison with the reference simulation [76] reveals a satisfactory agreement with the Average axial velocity profiles.

While these discrepancies in the RMS profiles at CRZ and the Averages at ORZ compared to experimental results are notable, it's important to highlight that a similar trend is observed in the reference simulation. This suggests that these discrepancies primarily arise from the assumption of adiabatic walls – absence of heat loss conditions. In the final section of this chapter, we will lift this assumption to observe the impact of heat losses on the flame shape and flow fields.

6.5.2 Pulsating case ($\phi = 0.7$)

In this subsection, we transition to the pulsating configuration by adopting the operating conditions of $\phi = 0.7$ and a thermal power of $P_{th} = 25\,\text{kW}$. Experiments conducted by Meier et al. [73] have demonstrated that under these conditions, the combustor exhibits self-excited thermoacoustic instabilities characterized by the pulsation of the flame up and down the stream within the combustion chamber.

Comparison

We begin by highlighting the distinctions between the quiet and pulsating modes. Firstly, in Figure 6.6a, we plot the pressure drops, – defined as the difference in absolute pressure between the plenum probe P_p and the combustion chamber probe P_c (probe locations are indicated in Figure 6.1 for reference). We observe that the mean pressure drop (ΔP) for both quiet and pulsating cases falls within the range of 1500 to 1800 Pa, which corroborates the findings of [39]. However, it is noteworthy that

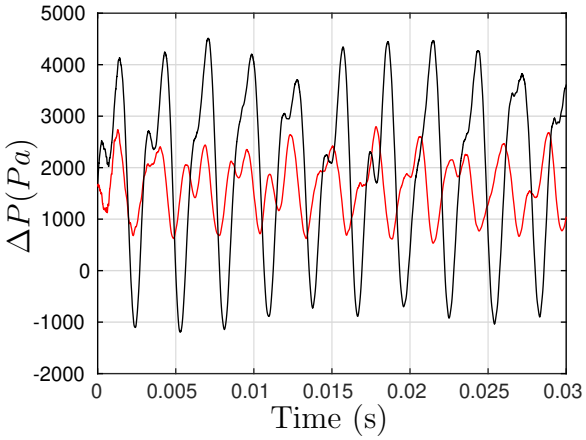

(a) Pressure drop

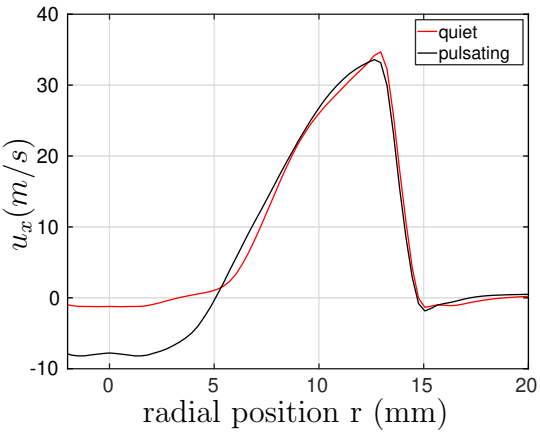

(b) Average axial velocity

.

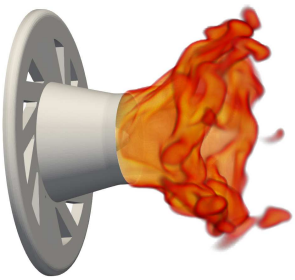

(c) Quiet flame

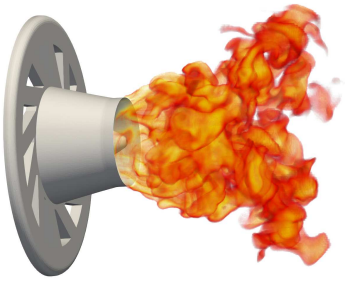

(d) Pulsating flame

Figure 6.6: Comparison between the Quiet and Pulsating modes of Preccinsta — (Quiet), — (Pulsating). Flame HRR are illustrated in (***c*** and ***d***) by volume rendering.

the maximum pressure drop in the pulsating case is significantly higher and exhibits negative pressure drops during its oscillation cycles. This behavior indicates that the combustion chamber pressure occasionally overtakes the plenum pressure, inducing a reversal of flow that pushes the flame upstream. This phenomenon can be considered one of the indicators of the instability in this configuration.

Next, by plotting the azimuthally averaged axial velocity at $h = 1.5\,\text{mm}$ in Figure 6.6b, we can observe that the reverse flow in the pulsating case is notably more pronounced in the pulsating case compared to the quiet case – a direct consequence of the aforementioned negative pressure drops. Nevertheless, it is worth mentioning that the simulated values in our study are lower than those observed experimentally by Meier et al. [73]. We have observed that adopting dynamic β_F and refining the mesh can help address these discrepancies.

Finally, Figures 6.6c and 6.6d renders the flames for both modes utilizing the iso-volume of $\dot{\omega_T}$. In the pulsating case, due to the lower laminar flame speed S_l, the flame length is extended, and more pockets of fresh gases are pinched off when compared to the quiet case. We postulate that the combustion of these enclosed pockets significantly contributes to the pronounced amplification of thermo-acoustic instability characteristic of the pulsating mode.

Statistical analysis

The average and RMS profiles of temperature and CO_2 mass fractions for the pulsating case are depicted in Fig. 6.7. Once more, the agreement between the simulated and experimental mean profiles is reasonable, except for the previously noted over-prediction in the ORZ region which is attributed to the influence of adiabatic walls. Although there is a slight underestimation, the RMS profiles of temperature and CO_2 mass fraction in this configuration unequivocally reveal the pulsations within the CRZ.

Thermoacoustic Instability

Figure. 6.8a illustrates the pressure signal fluctuations in both the plenum and the combustion chamber. In accordance with the experimental findings [73], it's evident that the pressure fluctuation trace from the plenum, represented in black, exhibits a smoother profile compared to that of the combustion chamber, shown in blue. Additionally, the pressure fluctuation in the plenum lags behind that of the combustion chamber.

Furthermore in fig. 6.8b, it is notable that the peak of the self-excited frequency is

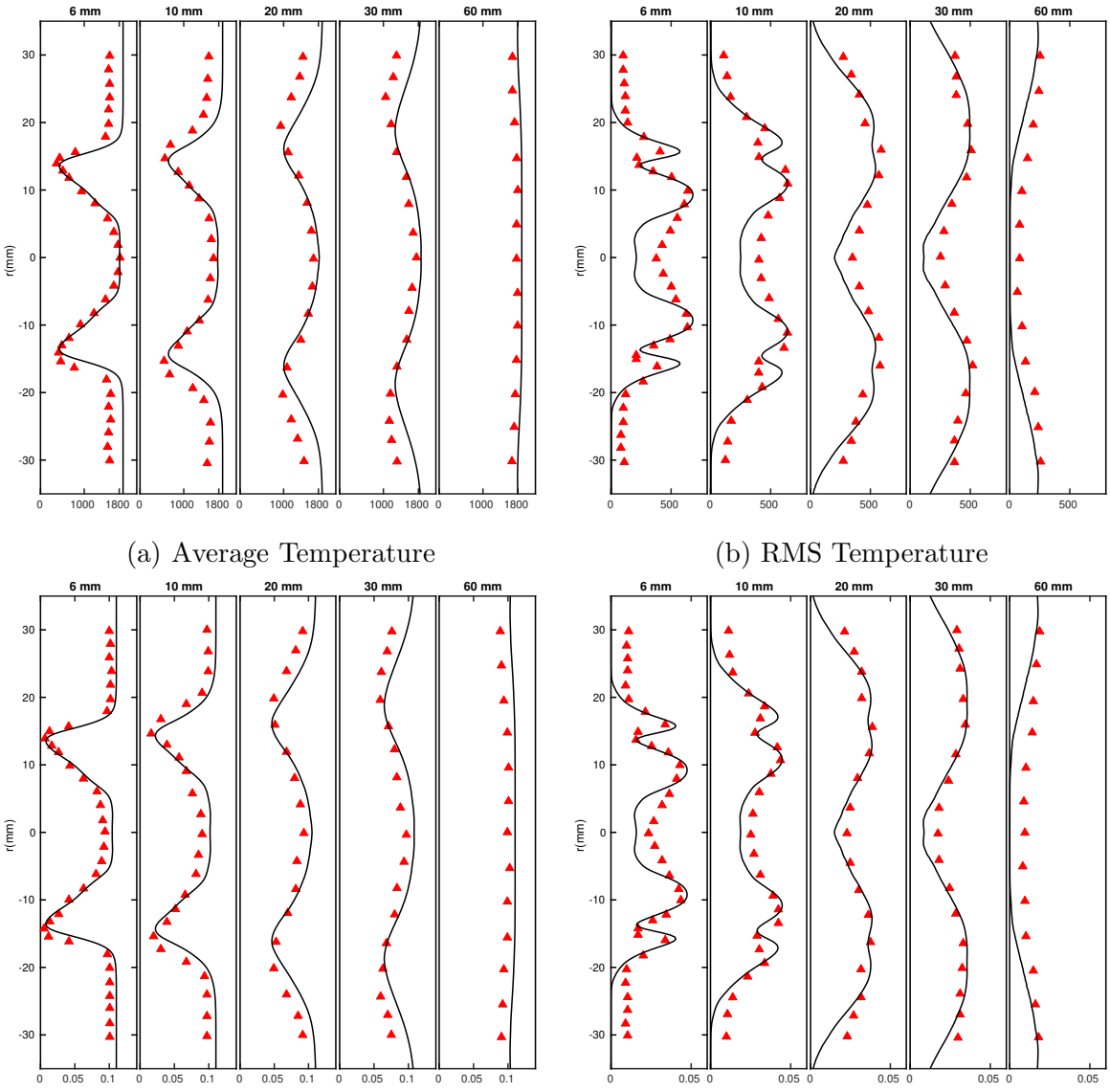

(a) Average Temperature

(b) RMS Temperature

(c) Average CO_2 mass fractions

(d) RMS CO_2 mass fractions

Figure 6.7: Average and RMS statistics for the pulsating case (tab:6.1). ▲ (experiments [73]), ▬ (ProLB).

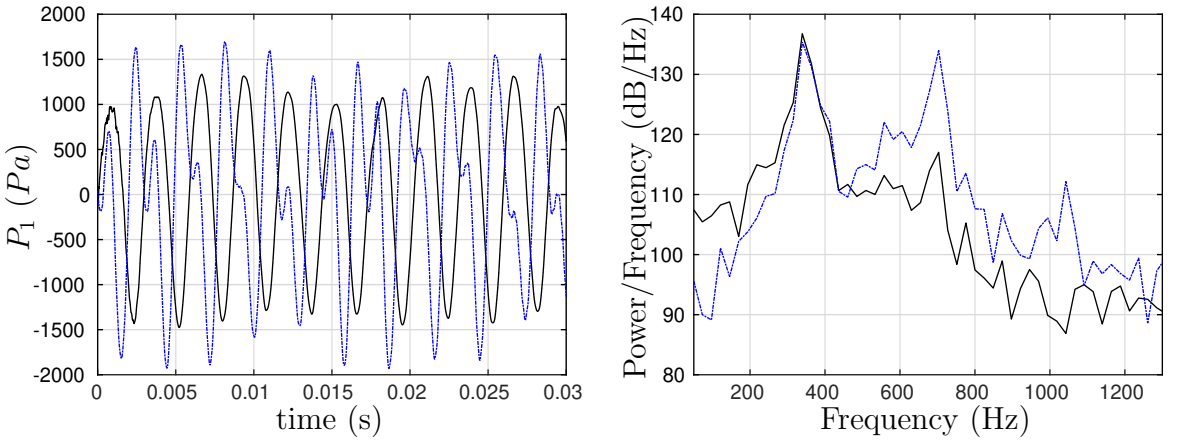

(a) Pressure fluctuations (b) Power Spectral Density (PSD) signals

Figure 6.8: Dynamic fluctuations of pressure in the plenum (▬) and chamber (▪▪) for the pulsating case ($\phi = 0.7$) and their respective power spectral density (PSD) signals.

approximately 340 Hz, and its harmonic is also discernible at around 680 Hz. Interestingly, the power of the primary frequency appears to be slightly greater in the plenum, while its harmonics are more pronounced in the combustion chamber.

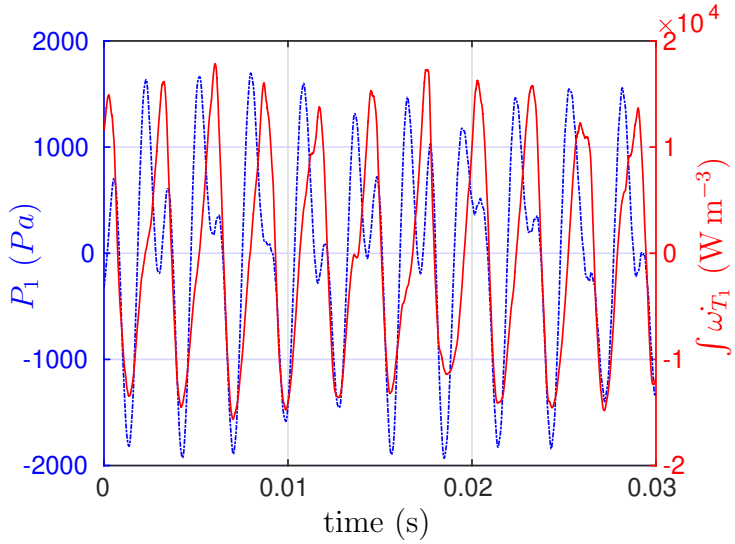

Figure 6.9: "In-phase" relationship between pressure fluctuations in the chamber (▪▪) and the total heat release fluctuations (▬) for the pulsating case ($\phi = 0.7$).

Fig. 6.9 presents the temporal fluctuations of the total heat release rate and pressure in the combustion chamber. Notably, these fluctuations are in phase, indicating that the instability is sustained by the coupling of flame and acoustics [39, 73, 110]. It's worth mentioning that similar acoustic modes exist in both quiet and cold cases, although their amplitudes are relatively small.

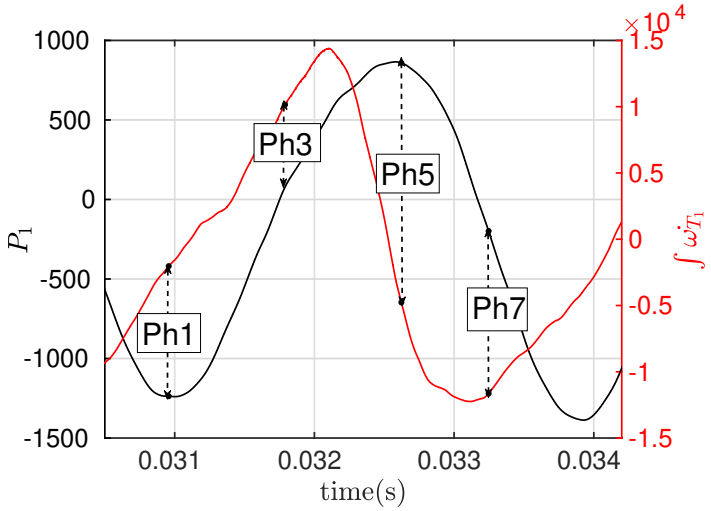

(a) Temporal fluctuations of the plenum pressure (—) and the total HRR fluctuations (—). Plenum pressure based phase angles chosen for the illustration of self-sustained oscillation cycle.

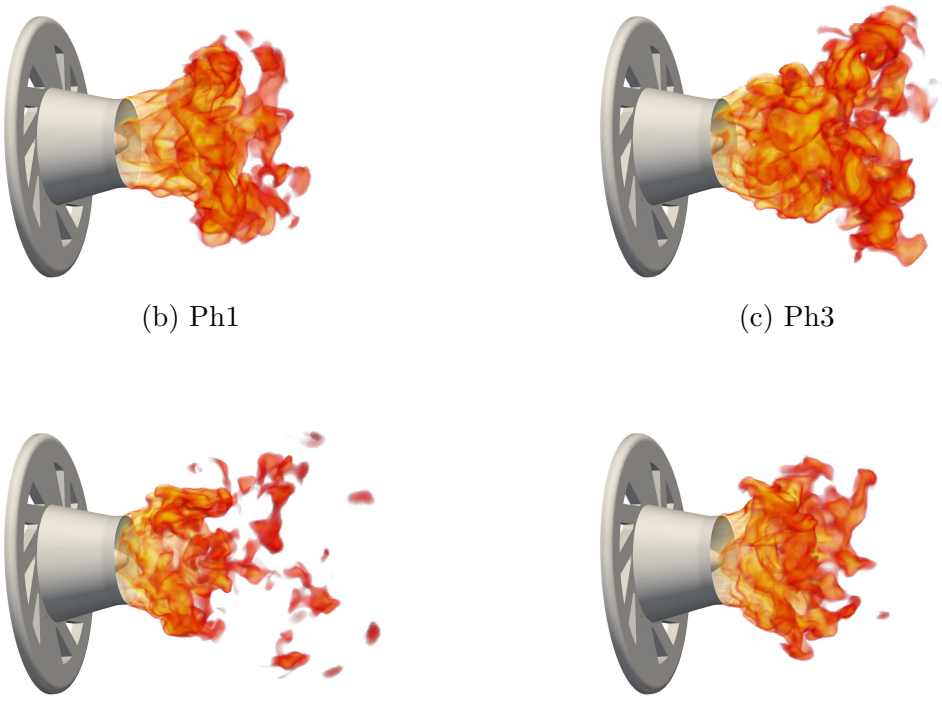

(b) Ph1

(c) Ph3

(d) Ph5

(e) Ph7

Figure 6.10: Illustration of single self-sustained oscillation cycle of the pulsating Preccinsta mode through instantaneous phase-locked volume-visualization of HRR in junction with the temporal fluctuations of plenum pressure and total HRR.

Finally, in Fig.6.10, we illustrate a cycle of self-sustained oscillations using the iso-volume of Heat Release Rate (HRR) as our illustrative metric. Simultaneously, Fig.6.10a presents the pressure fluctuations in the plenum alongside the total HRR fluctuations. Given the observation that the pressure drop ΔP closely follows the phase of the plenum pressure fluctuations, to illustrate the oscillatory behavior of the pulsating flame, we've selected four distinct phase angles of the plenum pressure fluctuations. These phase angles are chosen to roughly align with those selected by Meier et al. [73] for their experimental analysis of the pulsating Preccinsta mode.

- Plenum pressure is at its minimum during Phase Ph1 (Fig. 6.10b). However, due to its time-lag, both heat release rate and chamber pressure fluctuations are increasing rapidly during this phase.
- Combustion chamber pressure and combustion intensity peak shortly after Phase Ph3 (Fig. 6.10c). This high chamber pressure tends to push the flame upstream, causing it to disintegrate.
- Plenum pressure reaches its maximum at Phase Ph5 (Fig. 6.10e). The flame has significantly disintegrated and moved upstream. A rapid drop in the combustion intensity and chamber pressure can be seen.
- Just before Phase Ph7 (Fig. 6.10d), combustion intensity and pressure in the combustion chamber reach their minimum. The positive pressure drop between the plenum and chamber begins pushing the flame downstream and restarting the cycle.

While we succeed in reasonably capturing the quiet and pulsating mode of the Preccinsta burner, it is evident that there are clear areas for improvement. Notably, predicting temperature fields near walls and the amplitude of reverse flow/flame pulsations in pulsating configuration could benefit from further refinement. To address these issues, several strategies can be considered:

- Including measurements of wall temperature or heat flux could enhance the accuracy of temperature predictions near the wall. This aspect will be briefly discussed in the forthcoming section.
- Implementing a more comprehensive chemistry model, such as the 17-species reduced chemistry model proposed by [61], may improve precision, particularly for inner flame structures.

- Exploring the exponent parameter β_F for the sub-grid wrinkling factor Ξ within the TFLES framework could be beneficial. Prior research [110] has shown that this parameter plays a decisive role in amplifying flame-acoustic interactions. Although our initial investigations with the LBM-LES method indicates the same, more comprehensive analysis is required for conclusive insights.

6.6 Heat Losses

To address the issues of temperate discrepancy near the wall boundaries , we implemented a new wall heat transfer boundary condition capable of incorporating heat losses at the boundaries. This boundary condition is aligned with the basic idea of the Heat Resistance Tuning (HRT) approach proposed by Agostinelli et al. [1]. And much like HRT approach, our boundary condition presupposes prior knowledge of the thermal conductivity, thickness and length of wall, all of which can be readily acquired.

Assuming a linearized heat transfer model, where the heat transfer between the fluid and the wall equates to that between the wall and the ambient atmosphere, the relationship can be expressed as:

$$\frac{T_{\text{flow}} - T_{wall}}{R_{\text{flow}}} = \frac{T_{wall} - T_{ref}}{R_{\text{solid}}} \tag{6.19}$$

In this equation, T_{flow} denotes the fluid temperature in close proximity to the wall, a value obtained from the simulation. T_{ref} represents the ambient temperature, typically around 300 K. T_{wall} stands for the temperature at the wall, which needs to be specified but is currently an unknown variable. The parameters R_{flow} and R_{solid} correspond to the thermal resistances at the fluid-wall interface and the wall-ambient interface, respectively.

The thermal resistance R_{flow} can be defined as $R_{\text{flow}} = \frac{disn_0}{\lambda_{\text{fluid}}}$, where $disn_0$ signifies the distance normal from the wall to the nearest fluid point, and λ_{fluid} represents the thermal conductivity of the fluid (gas mixture) obtained from the simulation.

The wall-ambient resistance R_{solid} is determined as $R_{\text{solid}} = R_{\text{cond}} = L_s/\lambda_{\text{solid}}$, where L_s represents the characteristic length – the thickness of the wall, and λ_{solid} denotes the thermal conductivity of the solid wall material. If convection and radiation effects need to be considered, the total resistance can be calculated by treating convection and radiation as parallel processes [1]:

$$R_{\text{solid}} = R_{\text{cond}} + \frac{1}{\frac{1}{R_{\text{conv}}} + \frac{1}{R_{\text{rad}}}} \tag{6.20}$$

Ultimately, the previously unknown variable T_{wall} can now be determined using Equation (6.19). Provided correct resistances can be imposed, it is observed that the implementation of a this wall heat transfer boundary condition offers a simple solution to address heat loss near walls in LES simulations.

We implemented the thermal resistance R_{solid} at various solid boundary locations, utilizing values obtained from Agostinelli et al. [1]. These values are as follows:

$R_{\text{backplane}}$	$4.3 \times 10^{-3}\,\text{m}^2\,\text{K}\,\text{W}^{-1}$
$R_{\text{bluffbody}}$	$7.5 \times 10^{-3}\,\text{m}^2\,\text{K}\,\text{W}^{-1}$
$R_{\text{sidewalls}}$	$7 \times 10^{-2}\,\text{m}^2\,\text{K}\,\text{W}^{-1}$

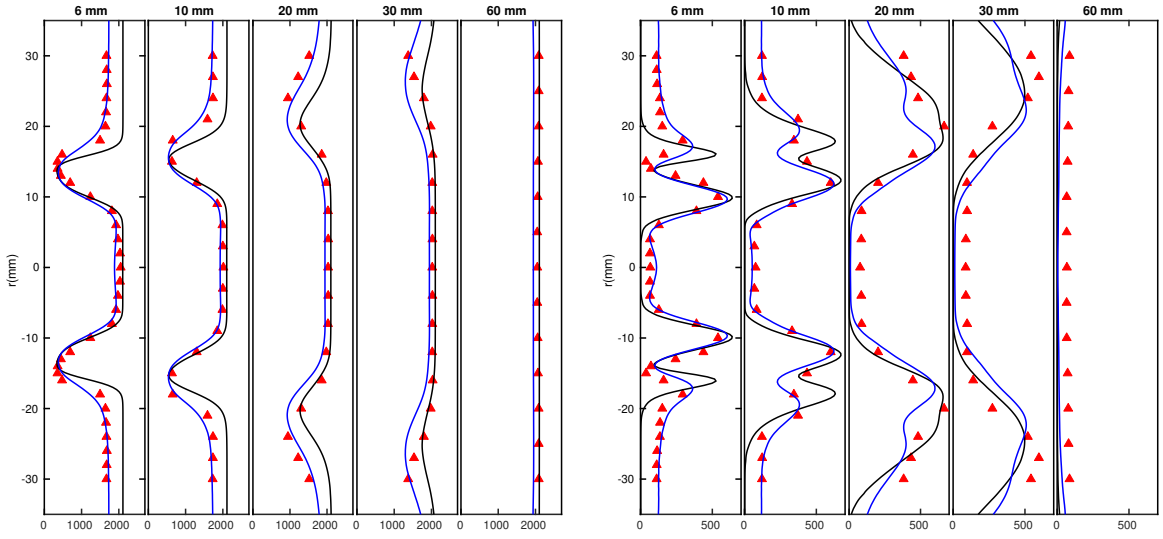

(a) Average Temperature (b) RMS Temperature

Figure 6.11: Average and RMS statistics for the quiet case with non-adiabatic boundaries. (experiments [73]), (ProLB adiabatic walls), (ProLB non-adiabatic walls).

Figure 6.11 demonstrates the improvement in temperature fields near the walls, both in average and RMS statistics, for the quiet Preccinsta configuration ($\phi = 0.83$). Additionally, the illustration of flame shapes, represented through temperature conditioned to HRR values exceeding 10% of their maximum, for simulations with adiabatic walls and walls with heat losses is presented in figure 6.12. It is evident that adopting wall boundaries with heat losses leads to "V" shaped flames [6], in contrast to the "M" shaped flames observed with adiabatic conditions.

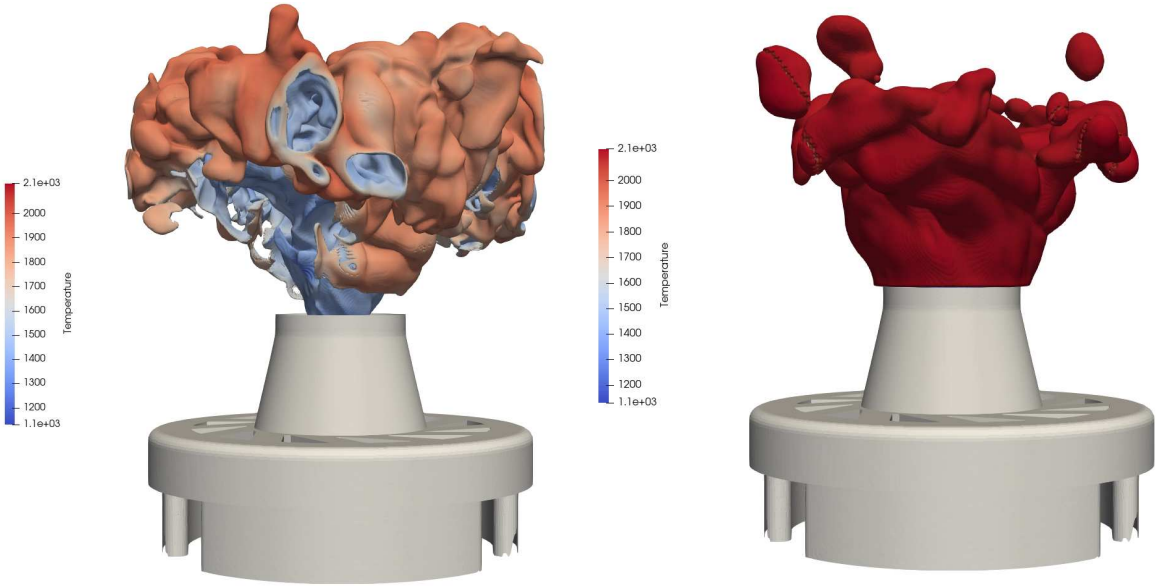

(a) Non-Adiabatic walls (b) Adiabatic walls

Figure 6.12: Illustration of flame shapes with and without heat-losses on the wall boundaries using contours colored by temperature, conditioned to HRR values exceeding 10% of their maximum.

6.7 Summary

In this chapter, we undertook a comprehensive exploration of the dynamics of Preccinsta burner, especially focusing on the manifestation of thermoacoustic modes in this burner. Notably, we leveraged the Lattice Boltzmann solver for the first time in this context, and our findings demonstrate the promising capabilities of Lattice Boltzmann methods for simulating complex burners, even when dealing with intricate geometries, non-uniform grid sizes and turbulent reactive flows plagued by thermoacoustic instabilities.

During our analysis of the thermoacoustic instability in this burner, we gained valuable insights into the oscillatory behavior of the pulsating flame. We observed the critical role of the coupling between flame and acoustics in sustaining this instability, supported by various pressure signals, power spectral densities, and heat release rate fluctuations, corroborating findings from Meier et al. [73].

Recognizing the challenges posed by temperature discrepancies in regions close to walls, we introduced a wall heat transfer boundary condition, which, in combination with thermal resistance values from previous studies [1], significantly improved flame shapes and temperature fields.

While the Lattice Boltzmann-driven approach accurately captured the core behavior of the Preccinsta burner across quiet and pulsating modes, it is clear that avenues for

further refinement exist. Future directions may encompass the incorporation of a more detailed kinetic description, advanced approximations for the efficiency exponent β_F, or the implementation of a PDF turbulent model.

In summary, this chapter has deepened our understanding of the dynamics of the Preccinsta burner. However, its achievement lies in emphasizing the remarkable effectiveness of the Lattice Boltzmann Method (LBM) in tackling complex combustion phenomena in such intricate burners.

Conclusion and Perspectives

Conclusion

The overarching objective of this research was to validate and demonstrate the effectiveness of the Hybrid-Lattice Boltzmann Method (LBM) in accurately resolving flame-acoustic interactions and addressing thermoacoustic instabilities. Our research encompassed a broad spectrum of investigations, ranging from fundamental theoretical validations to complex practical applications in advanced combustion scenarios.

The initial phase of our research centered on assessing the capability of LBM to model flame-acoustic interactions and thermoacoustic instabilities in simplified canonical cases. By examining the ability of the solver to accurately simulate the response of flame to external acoustic excitation and conducting detailed simulations within closed 2D channels, we established the potential of the LB method as a dependable tool for predicting combustion instabilities in various scenarios. Expanding our investigations, we highlighted the critical role of boundary conditions in the initial development and amplification of combustion instabilities. Moreover, through parametric studies on the impact of channel width, we demonstrated that the amplification of instability is a nuanced phenomenon, challenging the notion that wider channels invariably lead to greater instability.

Advancing our investigation, we delved into the dissipative and isotropic properties of the Hybrid-LBM in the context of acoustic transport, a crucial aspect for comprehensively studying sound generation and propagation during combustion. Our research reaffirmed that principal mechanisms such as Pinch-off and Flame Annihilation are key contributors to sound production. However, a significant revelation came from our investigation of sound generation due to hydrogen-air combustion, which highlighted the potential limitations of simple chemistry models, especially their tendency to over-predict due to inadequate representation of flame thickness. This prompted the intro-

duction of a new variable, ϵ, denoting the ratio of diffusive to thermal flame thickness, which played a crucial role in understanding the constraints of chemistry models on sound generation.

Furthermore, we conclusively established that the intensity of sound generation is predominantly influenced by the laminar flame speed, with a notable peak in sound production observed near an equivalence ratio $\phi = 1.5$ in hydrogen-air combustion. We also discovered that higher ambient pressures intensify sound generation, an insight crucial for burner design. Additionally, our research examined how the ratio epsilon and the Lewis number influence the amplitude of the pressure peak in planar annihilation events, leading to a new formulation of the effective Lewis number that aligns well with both simple and detailed chemistry models. These investigations not only validated the capability of the method in exploring combustion noise phenomena but also unveiled the complexities of sound generation in hydrogen-fueled scenarios.

The final phase of our research involved applying the LBM to the complex dynamics of an aeronautical burner known as the Preccinsta burner. Our specific focus was on understanding and simulating the manifestation of thermoacoustic modes within this system. This endeavor highlighted the robustness and versatility of the method in handling intricate geometries and turbulent reactive flows characterized by thermoacoustic instabilities. Our investigation provided insights into the oscillatory behavior of the pulsating flame and the critical role of the coupling between flame and acoustics in sustaining thermoacoustic instability. These findings were corroborated by various pressure signals and power spectral densities, aligning with prior research. Furthermore, we also addressed challenges posed by temperature disparities near walls by introducing a wall heat transfer boundary condition. These explorations were instrumental in validating the capabilities of LBM in real-world scenarios.

In conclusion, this thesis has made substantial advancements in showcasing the versatility and promise of the Lattice Boltzmann Method, with a particular emphasis on the Hybrid-LBM, in the analysis of flame-acoustic interactions and thermoacoustic instabilities. Spanning from foundational theoretical validations to practical implementations in complex burner, this research has not only highlighted the potential of LBM, but also reaffirmed established insights and broadened our understanding of thermoacoustic phenomena across these various settings. Through its diverse demonstrations, it has laid the foundation for future explorations, encouraging continued development and application of this powerful tool in increasingly sophisticated combustion systems.

Perspectives

This section outlines future research directions related to this study:

- In semi-open long slip channels, as depicted in Figure 4.16a, there was a notable and sudden increase in flame consumption speed (flame surface area). While this phenomenon was not thoroughly investigated at the time, its further exploration could be valuable, especially considering its potential implications for the transition from Deflagration to Detonation (DDT).

- With the precise Non-reflecting Inlet boundary conditions already established (Sec: 3.4.1), there is an opportunity for investigation of the newly discovered Intrinsic Thermoacoustic Instability (ITA) using LBM.

- An examination of Figure 5.6c reveals that flame pinch-off events result in more pronounced pressure variations. This thesis primarily concentrated on the less intense flame annihilation events. Therefore, a deeper exploration of pinch-off events might be essential for a comprehensive understanding of the major contributors to the 'Direct Sound' phenomenon.

- The proposed effective Lewis number, as outlined in Equation (5.16), was derived solely from observational data. If this formulation is applicable to other fuels, additional research is required to establish its theoretical foundation.

- Leveraging the proven capabilities of LBM, future research could explore the relationship between combustion noise and thermoacoustic instabilities. Additionally, this could extend to investigating active control methods for these instabilities.

- The observation of thermoacoustic modes in the Preccinsta burner (fig: 6.10), particularly with premixed injection raises intriguing questions regarding the emergence of these modes. In addition to the validations already carried out, a thorough parametric analysis that includes various fuel injection modes, and potentially incorporates the dynamic formulation of the sub-wrinkling model or other advanced turbulent models may be essential for a deeper understanding of how these modes arise in this system.

- The notable variation in flame shape (fig: 6.12) caused by the heat loss boundary condition calls for more in-depth exploration, particularly in the unstable case. Furthermore, given the available experimental data, a valuable research direction would be to examine the impact of Hydrogen-Methane blends on the thermoacoustic modes of this complex burner.

Bibliography

[1] P W Agostinelli, D Laera, I Boxx, L Gicquel, and T Poinsot. Impact of wall heat transfer in large eddy simulation of flame dynamics in a swirled combustion chamber. *Combustion and Flame*, 234:111728, 2021.

[2] C Angelberger, D Veynante, F Egolfopoulos, and T Poinsot. Large eddy simulations of combustion instabilities in premixed flames. In *Proc. of the summer program*, pages 61–82. Citeseer, 1998.

[3] F Baillot and A Bourehla. Burning velocity of pockets from a vibrating flame experiment. *Combustion science and technology*, 126(1-6):201–224, 1997.

[4] Françoise Baillot, Daniel Durox, Sébastien Ducruix, Geoffrey Searby, and L Boyer. Parametric response of a conical flame to acoustic waves. *Combustion science and technology*, 142(1-6):91–109, 1999.

[5] Joachim Beeckmann, Raik Hesse, Stephan Kruse, André Berens, Norbert Peters, Heinz Pitsch, and Moshe Matalon. Propagation speed and stability of spherically expanding hydrogen/air flames: Experimental study and asymptotics. *Proceedings of the Combustion Institute*, 36(1):1531–1538, 2017.

[6] Pierre Bénard, Ghislain Lartigue, Vincent Moureau, and Renaud Mercier. Large-eddy simulation of the lean-premixed preccinsta burner with wall heat loss. *Proc. Combust. Inst.*, 37:5233–5243, 2019.

[7] Karthik Bhairapurada, Bruno Denet, and Pierre Boivin. A lattice-boltzmann study of premixed flames thermo-acoustic instabilities. *Combust. Flame*, 240: 112049, 2022.

[8] Prabhu Lal Bhatnagar, Eugene P Gross, and Max Krook. A model for collision processes in gases. i. small amplitude processes in charged and neutral one-component systems. *Physical review*, 94(3):511, 1954.

[9] Pierre Boivin, Carmen Jiménez, Antonio L Sánchez, and Forman A Williams. An explicit reduced mechanism for H2–air combustion. *Proceedings of the Combustion Institute*, 33(1):517–523, 2011.

[10] Pierre Boivin, M Tayyab, and S Zhao. Benchmarking a lattice-boltzmann solver for reactive flows: Is the method worth the effort for combustion? *Phys. Fluids*, 33:071703, 2021.

[11] Guillaume Bres, Franck Pérot, and David Freed. Properties of the lattice boltzmann method for acoustics. In *15th AIAA/CEAS aeroacoustics conference (30th AIAA aeroacoustics conference)*, page 3395, 2009.

[12] TD Butler and Peter J O'Rourke. A numerical method for two dimensional unsteady reacting flows. In *Symposium (international) on combustion*, volume 16, pages 1503–1515. Elsevier, 1977.

[13] Sébastien Candel, Daniel Durox, Sébastien Ducruix, A-L Birbaud, Nicolas Noiray, and Thierry Schuller. Flame dynamics and combustion noise: progress and challenges. *International Journal of Aeroacoustics*, 8(1):1–56, 2009.

[14] Damiano Casalino, André FP Ribeiro, Ehab Fares, and Swen Nölting. Lattice–Boltzmann aeroacoustic analysis of the lagoon landing-gear configuration. *AIAA J.*, 52:1232–1248, 2014.

[15] Fabrice Charlette, Charles Meneveau, and Denis Veynante. A power-law flame wrinkling model for les of premixed turbulent combustion part i: non-dynamic formulation and initial tests. *Combust. Flame*, 131:159–180, 2002.

[16] Shiyi Chen and Gary D Doolen. Lattice boltzmann method for fluid flows. *Annu. Rev. Fluid Mech.*, 30:329–364, 1998.

[17] Boa-Teh Chu. On the energy transfer to small disturbances in fluid flow (part i). *Acta Mechanica*, 1(3):215–234, 1965.

[18] Paul Clavin. Dynamics of combustion fronts in premixed gases: from flames to detonations. *Proceedings of the Combustion Institute*, 28(1):569–585, 2000.

[19] Paul Clavin and Pedro Garcia. The influence of the temperature dependence of diffusivities on the dynamics. *Journal de Mécanique Théorique et Appliquée*, 2 (2):245–263, 1983.

[20] Paul Clavin, Pierre Pelcé, and Longting He. One-dimensional vibratory instability of planar flames propagating in tubes. *Journal of Fluid Mechanics*, 216:299–322, 1990.

[21] O Colin, Frédéric Ducros, D Veynante, and Thierry Poinsot. A thickened flame model for large eddy simulations of turbulent premixed combustion. *Phys. Fluids*, 12:1843–1863, 2000.

[22] T Coratger, G Farag, S Zhao, Pierre Boivin, and P Sagaut. Large-eddy lattice-boltzmann modeling of transonic flows. *Phys. Fluids*, 33:115112, 2021.

[23] Christophe Coreixas, Gauthier Wissocq, Guillaume Puigt, Jean-François Boussuge, and Pierre Sagaut. Recursive regularization step for high-order lattice boltzmann methods. *Physical Review E*, 96(3):033306, 2017.

[24] Christophe Guy Coreixas. *High-order extension of the recursive regularized lattice Boltzmann method*. PhD thesis, 2018.

[25] Emilien Courtine, Laurent Selle, and Thierry Poinsot. Dns of intrinsic thermoacoustic modes in laminar premixed flames. *Combustion and Flame*, 162(11): 4331–4341, 2015.

[26] G Darrieus. Propagation d'un front de flamme. *La Technique Moderne*, 30:18, 1938.

[27] Guillaume Daviller, Gorkem Oztarlik, and Thierry Poinsot. A generalized non-reflecting inlet boundary condition for steady and forced compressible flows with injection of vortical and acoustic waves. *Computers & Fluids*, 190:503–513, 2019.

[28] Virginia Parker Dawson. *Taming liquid hydrogen: the Centaur upper stage rocket, 1958-2002*, volume 4230. National Aeronautics and Space Administration,[NASA History Office,] Office, 2004.

[29] Anne Dejoan, Carmen Jiménez, and Vadim N. Kurdyumov. Critical conditions for non-symmetric flame propagation in narrow channels: Influence of the flow rate, the thermal expansion, the lewis number and heat-losses. *Combust. Flame*, 209:430–440, 2019. ISSN 0010-2180.

[30] B Denet and A Toma. Numerical study of premixed flames parametric acoustic instability. *Combust Sci Technol*, 109(1-3):23–33, 1995.

[31] Giovanni Di Ilio, Benedikt Dorschner, Gino Bella, Sauro Succi, and Iliya V Karlin. Simulation of turbulent flows with the entropic multirelaxation time lattice boltzmann method on body-fitted meshes. *Journal of Fluid Mechanics*, 849:35–56, 2018.

[32] Ann P Dowling, MM Sevik, and JE Ffowcs-Williams. Sound and sources of sound. 1984.

[33] Roger A Dunlap. Resonance of a flame in a parallel-walled combustion chamber. Technical report, 1950.

[34] D Durox, F Baillot, G Searby, and L Boyer. On the shape of flames under strong acoustic forcing: a mean flow controlled by an oscillating flow. *Journal of fluid mechanics*, 350:295–310, 1997.

[35] Thomas Emmert, Sebastian Bomberg, and Wolfgang Polifke. Intrinsic thermoacoustic instability of premixed flames. *Combustion and Flame*, 162(1):75–85, 2015.

[36] Gabriel Farag, Song Zhao, Thomas Coratger, Pierre Boivin, Guillaume Chiavassa, and Pierre Sagaut. A pressure-based regularized lattice-boltzmann method for the simulation of compressible flows. *Physics of Fluids*, 32(6), 2020.

[37] Gabriel Farag, Song Zhao, Guillaume Chiavassa, and Pierre Boivin. Consistency study of lattice-boltzmann schemes macroscopic limit. *Physics of Fluids*, 33(3), 2021.

[38] ML Frankel and GI Sivashinsky. The effect of viscosity on hydrodynamic stability of a plane flame front. *Combustion Science and Technology*, 29(3-6):207–224, 1982.

[39] Benedetta Franzelli, Eleonore Riber, Laurent YM Gicquel, and Thierry Poinsot. Large eddy simulation of combustion instabilities in a lean partially premixed swirled flame. *Combustion and flame*, 159(2):621–637, 2012.

[40] Nicolò Frapolli, Shyam S Chikatamarla, and Iliya V Karlin. Entropic lattice boltzmann model for compressible flows. *Physical Review E*, 92(6):061301, 2015.

[41] Nicolò Frapolli, Shyam Sunder Chikatamarla, and Iliya V Karlin. Entropic lattice boltzmann simulation of thermal convective turbulence. *Computers & Fluids*, 175: 2–19, 2018.

[42] Aurel Galántai. The theory of newton's method. *Journal of Computational and Applied Mathematics*, 124(1-2):25–44, 2000.

[43] David G. Goodwin, Harry K. Moffat, and Raymond L. Speth. Cantera: An object-oriented software toolkit for chemical kinetics, thermodynamics, and transport processes. http://www.cantera.org, 2017.

[44] Xiaoyi He and Li-Shi Luo. Theory of the lattice boltzmann method: From the boltzmann equation to the lattice boltzmann equation. *Physical review E*, 56(6): 6811, 1997.

[45] Xiaoyi He, Shiyi Chen, and Gary D Doolen. A novel thermal model for the lattice boltzmann method in incompressible limit. *Journal of computational physics*, 146 (1):282–300, 1998.

[46] Seyed Ali Hosseini, Amir Eshghinejadfard, Nasser Darabiha, and Dominique Thévenin. Weakly compressible lattice boltzmann simulations of reacting flows with detailed thermo-chemical models. *Comput. Math. with Appl*, 79:141–158, 2020.

[47] Seyed Ali Hosseini, Nasser Darabiha, and Dominique Thévenin. Low mach number lattice boltzmann model for turbulent combustion: flow in confined geometries. *Proc. Combust. Inst.*, 2022.

[48] Jérôme Jacob, Orestis Malaspinas, and Pierre Sagaut. A new hybrid recursive regularised bhatnagar–gross–krook collision model for lattice boltzmann method-based large eddy simulation. *Journal of Turbulence*, 19(11-12):1051–1076, 2018.

[49] C Jiménez, A Haghiri, MJ Brear, M Talei, and ER Hawkes. Sound generation by premixed flame annihilation with full and simple chemistry. *Proceedings of the Combustion Institute*, 35(3):3317–3325, 2015.

[50] Carmen Jiménez, Daniel Fernández-Galisteo, and Vadim N Kurdyumov. Flame-acoustics interaction for symmetric and non-symmetric flames propagating in a narrow duct from an open to a closed end. *Combust. Flame*, 225:499–512, 2021.

[51] WE Kaskan. An investigation of vibrating flames. In *Symposium (International) on Combustion*, volume 4, pages 575–591. Elsevier, 1953.

[52] Mehdi R Khorrami and Ehab Fares. Simulation-based airframe noise prediction of a full-scale, full aircraft. In *22nd AIAA/CEAS aeroacoustics conference*, page 2706, 2016.

[53] Timm Krüger, Halim Kusumaatmaja, Alexandr Kuzmin, Orest Shardt, Goncalo Silva, and Erlend Magnus Viggen. The lattice boltzmann method. *Springer International Publishing*, 10:4–15, 2017.

[54] Pierre Lallemand and Li-Shi Luo. Theory of the lattice boltzmann method: Acoustic and thermal properties in two and three dimensions. *Physical review E*, 68(3):036706, 2003.

[55] LD Landau. Slow combustion theory. *Zh. Eksp. Teor. Fiz*, 14(6):240–244, 1944.

[56] Jonas Latt and Bastien Chopard. Lattice boltzmann method with regularized pre-collision distribution functions. *Mathematics and Computers in Simulation*, 72(2-6):165–168, 2006.

[57] Timothy C Lieuwen and Vigor Yang. *Combustion instabilities in gas turbine engines: operational experience, fundamental mechanisms, and modeling*. American Institute of Aeronautics and Astronautics, 2005.

[58] A Linan and FA Williams. Fundamental aspects of combustion. 1993.

[59] Peter J Linstrom and William G Mallard. The nist chemistry webbook: A chemical data resource on the internet. *J Chem. Eng. Data*, 46:1059–1063, 2001.

[60] Rainald Löhner. Towards overcoming the LES crisis. *Int. J. Comput. Fluid Dyn.*, pages 1–11, 2019.

[61] Tianfeng Lu and Chung K. Law. A criterion based on computational singular perturbation for the identification of quasi-steady state species: A reduced mechanism for methane oxidation with no chemistry. *Combustion and Flame*, 154(4): 761–774, 2008. ISSN 0010-2180. doi: https://doi.org/10.1016/j.combustflame.2008.04.025.

[62] Weeratunge Malalasekera, KKJ Ranga-Dinesh, Salah S Ibrahim, and Assaad R Masri. Les of recirculation and vortex breakdown in swirling flames. *Combustion Science and Technology*, 180(5):809–832, 2008.

[63] Ernest Mallard. Recherches experimentales et theoriques sur la combustion des melanges gaseux explosifs. *Ann. mines*, 8(4):274–568, 1883.

[64] Simon Marié, Denis Ricot, and Pierre Sagaut. Comparison between lattice boltzmann method and navier–stokes high order schemes for computational aeroacoustics. *J. Comput. Phys.*, 228:1056–1070, 2009.

[65] G. H. Markstein. Interaction of Flow Pulsations and Flame Propagation. *J. Aeronaut. Sci.*, 18:428–429, June 1951. ISSN 1936-9956.

[66] George H Markstein. *Nonsteady flame propagation: AGARDograph*. Elsevier, 2014.

[67] GH Markstein. Flames as amplifiers of fluid mechanical disturbances. In *Proceedings of the 6th National Congress for Applied Mechanics, Cambridge, MA*, pages 11–33, 1970.

[68] Moshe Matalon and Bernard J Matkowsky. Flames as gasdynamic discontinuities. *Journal of Fluid Mechanics*, 124:239–259, 1982.

[69] Keijo K Mattila, Paulo C Philippi, and Luiz A Hegele. High-order regularization in lattice-boltzmann equations. *Physics of Fluids*, 29(4), 2017.

[70] James Clerk Maxwell. V. illustrations of the dynamical theory of gases.—part i. on the motions and collisions of perfectly elastic spheres. *The London, Edinburgh, and Dublin Philosophical Magazine and Journal of Science*, 19(124):19–32, 1860.

[71] Bonnie J McBride. *Coefficients for calculating thermodynamic and transport properties of individual species*, volume 4513. NASA Langley Research Center, 1993.

[72] Norman William McLachlan. Theory and application of Mathieu functions. *Publisher to the University Geoffrey Cumberlege, Oxford University Press*, 1951.

[73] WEIGAND Meier, Peter Weigand, Xuru R Duan, and Robert Giezendanner-Thoben. Detailed characterization of the dynamics of thermoacoustic pulsations in a lean premixed swirl flame. *Combust. Flame*, 150:2–26, 2007.

[74] Marek Krzysztof Misztal, Anier Hernandez-Garcia, Rastin Matin, Henning Osholm Sørensen, and Joachim Mathiesen. Detailed analysis of the lattice boltzmann method on unstructured grids. *Journal of Computational Physics*, 297:316–339, 2015.

[75] Philip McCord Morse and K Uno Ingard. *Theoretical acoustics*. Princeton university press, 1986.

[76] Vincent Moureau, P Domingo, and Luc Vervisch. From large-eddy simulation to direct numerical simulation of a lean premixed swirl flame: Filtered laminar flame-pdf modeling. *Combust. Flame*, 158:1340–1357, 2011.

[77] Franck Nicoud and Thierry Poinsot. Thermoacoustic instabilities: Should the rayleigh criterion be extended to include entropy changes? *Combustion and flame*, 142(1-2):153–159, 2005.

[78] F. Osmanlic and C. Körner. Lattice Boltzmann method for Oldroyd-B fluids. *Computers and Fluids*, 124:190–196, 2016.

[79] Pierre Pelce and Paul Clavin. Influence of hydrodynamics and diffusion upon the stability limits of laminar premixed flames. *Journal of Fluid Mechanics*, 124: 219–237, 1982. doi: 10.1017/S002211208200247X.

[80] Pierre Pelce and Paul Clavin. Influence of hydrodynamics and diffusion upon the stability limits of laminar premixed flames. In *Dynamics of Curved Fronts*, pages 425–443. Elsevier, 1988.

[81] Arkady Petchenko, Vitaly Bychkov, V'yacheslav Akkerman, and Lars-Erik Eriksson. Flame–sound interaction in tubes with nonslip walls. *Combust. Flame*, 149: 418–434, 2007.

[82] T Poinsot and SK Lele. Boundary conditions for direct simulations of compressible viscous flows. *Journal of computational physics*, 101(1):104–129, 1992.

[83] T Poinsot and D Veynante. *Theoretical and numerical combustion*. RT Edwards, Inc., 2005.

[84] W Polifke, C Wall, and P Moin. Partially reflecting and non-reflecting boundary conditions for simulation of compressible viscous flow. *Journal of Computational Physics*, 213(1):437–449, 2006.

[85] Yue-Hong Qian, Dominique d'Humières, and Pierre Lallemand. Lattice bgk models for navier-stokes equation. *Europhysics letters*, 17(6):479, 1992.

[86] Ruo-Fan Qiu, Cheng-Xiang Zhu, Rong-Qian Chen, Jian-Feng Zhu, and Yan-Cheng You. A double-distribution-function lattice boltzmann model for high-speed compressible viscous flows. *Computers & Fluids*, 166:24–31, 2018.

[87] Basile Radisson. *Dynamique non linéaire de fronts de flammes: expériences et modélisation*. PhD thesis, Aix-Marseille, 2019.

[88] Basile Radisson, Juliette Piketty-Moine, and Christophe Almarcha. Coupling of vibro-acoustic waves with premixed flame. *Phys. Rev. Fluids*, 4:121201, 2019.

[89] BV Rauschenbach. Vibrational combustion. *Moscow: Mir*, 1961.

[90] Sebastién Roux, G Lartigue, Thierry Poinsot, Ulrich Meier, and Claude Bérat. Studies of mean and unsteady flow in a swirled combustor using experiments, acoustic analysis, and large eddy simulations. *Combustion and Flame*, 141(1-2): 40–54, 2005.

[91] Andreas W Schafer, Steven RH Barrett, Khan Doyme, Lynnette M Dray, Albert R Gnadt, Rod Self, Aidan O'Sullivan, Athanasios P Synodinos, and Antonio J Torija. Technological, economic and environmental prospects of all-electric aircraft. *Nature Energy*, 4(2):160–166, 2019.

[92] Thierry Schuller, Thierry Poinsot, and Sébastien Candel. Dynamics and control of premixed combustion systems based on flame transfer and describing functions. *J. Fluid Mech.*, 894, 2020.

[93] Geoff Searby. Acoustic instability in premixed flames. *Combustion science and technology*, 81(4-6):221–231, 1992.

[94] Geoffrey Searby and Daniel Rochwerger. A parametric acoustic instability in premixed flames. *J. Fluid Mech.*, 231:529–543, 1991.

[95] Alois Sengissen, Jean-Christophe Giret, Christophe Coreixas, and Jean-Francois Boussuge. Simulations of lagoon landing-gear noise using lattice boltzmann solver. In *21st AIAA/CEAS Aeroacoustics Conference*, page 2993, 2015.

[96] GI Sivashinsky. Nonlinear analysis of hydrodynamic instability in laminar flames—i. derivation of basic equations. In *Dynamics of Curved Fronts*, pages 459–488. Elsevier, 1988.

[97] GI Sivashinsky and P Clavin. On the nonlinear theory of hydrodynamic instability in flames. *Journal de Physique*, 48(2):193–198, 1987.

[98] George P Sutton and Oscar Biblarz. *Rocket propulsion elements*. John Wiley & Sons, 2016.

[99] Said Taileb, Alejandro Millán-Merino, Song Zhao, and Pierre Boivin. Lattice-boltzmann modeling of lifted hydrogen jet flames: A new model for hazardous ignition prediction. *Combust. Flame*, 245:112317, 2022.

[100] Mohsen Talei, Michael J Brear, and Evatt R Hawkes. Sound generation by laminar premixed flame annihilation. *Journal of Fluid Mechanics*, 679:194–218, 2011.

[101] Mohsen Talei, Michael John Brear, and Evatt Robert Hawkes. A parametric study of sound generation by premixed laminar flame annihilation. *Combustion and Flame*, 159(2):757–769, 2012.

[102] Mohsen Talei, Evatt R Hawkes, and Michael J Brear. A direct numerical simulation study of frequency and Lewis number effects on sound generation by two-dimensional forced laminar premixed flames. *Proceedings of the Combustion Institute*, 34(1):1093–1100, 2013.

[103] M Tayyab, S Zhao, and Pierre Boivin. Lattice-boltzmann modeling of a turbulent bluff-body stabilized flame. *Phys. Fluids*, 33:031701, 2021.

[104] Muhammad Tayyab. *Development of combustion modelling within lattice Boltzmann framework*. PhD thesis, Aix-Marseille, 2020.

[105] Muhammad Tayyab, Basile Radisson, Christophe Almarcha, Bruno Denet, and Pierre Boivin. Experimental and numerical Lattice-Boltzmann investigation of the Darrieus–Landau instability. *Combustion and Flame*, 221:103–109, 2020.

[106] Muhammad Tayyab, Song Zhao, Yongliang Feng, and Pierre Boivin. Hybrid regularized Lattice-Boltzmann modelling of premixed and non-premixed combustion processes. *Combust. Flame*, 211:173–184, 2020.

[107] A Thomas and GT Williams. Flame noise: sound emission from spark-ignited bubbles of combustible gas. *Proceedings of the Royal Society of London. Series A. Mathematical and Physical Sciences*, 294(1439):449–466, 1966.

[108] P Tudisco, R Ranjan, S Menon, S Jaensch, and W Polifke. Application of the time-domain impedance boundary condition to large-eddy simulation of combustion instability in a shear-coaxial high pressure combustor. *Flow, Turbulence and Combustion*, 99:185–207, 2017.

[109] Stefano Ubertini and Sauro Succi. A generalised lattice boltzmann equation on unstructured grids. *Communications in Computational Physics*, 3(2):342–356, 2008.

[110] P S Volpiani, Thomas Schmitt, and Denis Veynante. Large eddy simulation of a turbulent swirling premixed flame coupling the tfles model with a dynamic wrinkling formulation. *Combust. Flame*, 180:124–135, 2017.

[111] AW Vreman. An eddy-viscosity subgrid-scale model for turbulent shear flow: Algebraic theory and applications. *Phys. Fluids*, 16:3670–3681, 2004.

[112] FA Williams. Theory of combustion in laminar flows. *Annual Review of Fluid Mechanics*, 3(1):171–188, 1971.

[113] FA Williams et al. Chemical-kinetic mechanisms for combustion applications, University of California, San Diego. *http://web.eng.ucsd.edu/mae/groups/combustion/mechanism.html*, 2018.

[114] Dieter A Wolf-Gladrow. *Lattice-gas cellular automata and lattice Boltzmann models: an introduction*. Springer, 2004.

[115] JB Zel'dovich and DA Frank-Kamenetzki. A theory of thermal propagation of flame. In *Dynamics of curved fronts*, pages 131–140. Elsevier, 1988.

[116] S Zhao, G Farag, Pierre Boivin, and P Sagaut. Toward fully conservative hybrid lattice boltzmann methods for compressible flows. *Phys. Fluids*, 32:126118, 2020.

[117] Song Zhao, Karthik Bhairapurada, Muhammad Tayyab, Renaud Mercier, and Pierre Boivin. Lattice-boltzmann modeling of the quiet and unstable preccinsta burner modes. *Computers & Fluids*, 260:105898, 2023.

Appendix A

Simulation parameters

Name	Symbol	Value
Mach number	Ma	0.0028
Flame speed	S_l	$1\,\mathrm{m\,s^{-1}}$
Activation energy	E_a	$30\,\mathrm{kcal\,mol^{-1}}$
Pre-exponential factor	A	$14.85 \times 10^{14}\,\mathrm{cm^3\,mol^{-1}\,s^{-1}}$
Thermal diffusivity in unburnt state	D_T^f	$1 \times 10^{-4}\,\mathrm{m^2\,s^{-1}}$
Flame diffusive thickness	$\delta_D = \frac{D_T^f}{S_l}$	$1 \times 10^{-4}\,\mathrm{m}$
Constant pressure specific heat	C_p	$1250\,\mathrm{J\,kg^{-1}\,K^{-1}}$
Thermal expansion parameter	$E_T = \frac{T_b}{T_u}$	8
Zel'dovich number	$\beta = \frac{E_a(T_b - T_u)}{RT_b^2}$	5.5
Lewis number	Le	1
Prandtl number	$Pr = \frac{\nu}{D_{th}}$	0.15
Acoustic Reynolds number	$Re_a = \frac{\delta_T . c_0}{\nu_0}$	2225
Space discretization step	Δx	$5 \times 10^{-5}\,\mathrm{m}$
Time discretization step	Δt	$2.624 \times 10^{-8}\,\mathrm{s}$

Table A.1: Parameters used in Sec. 4.3 and Sec. 4.5

Name	Symbol	Value
Flame speed	S_l	$0.20\,\mathrm{m\,s^{-1}}$
Activation energy	E_a	$30\,\mathrm{kcal\,mol^{-1}}$
Pre-exponential factor	A	$4.45 \times 10^{13}\,\mathrm{cm^3\,mol^{-1}\,s^{-1}}$
Thermal diffusivity in unburnt state	D_T^f	$2.17 \times 10^{-5}\,\mathrm{m^2\,s^{-1}}$
Flame diffusive thickness	$\delta_D = \frac{D_T^f}{S_l}$	$1.085 \times 10^{-4}\,\mathrm{m}$
Flame transit time	$\tau = \frac{D_{th}}{S_l^2}$	$5.425 \times 10^{-4}\,\mathrm{s}$
Expansion parameter	$E_\rho = \frac{\rho_u}{\rho_b}$	7.7
Reduced acoustic frequency	$\tilde{\omega_a} = 2\pi f \tau$	3.40
Inlet perturbation amplitude	A_0	0.25, 0.84, 1.86
Wave number of structures on the flame	$\tilde{k} = \frac{2\pi\delta_T}{\lambda}$	0.08
Prandtl Number	Pr	0.68
Markstein Number	$\mathcal{M}$	4.5
Space discretization step	Δx	$5 \times 10^{-5}\,\mathrm{m}$
Time discretization step	Δt	$2.624 \times 10^{-8}\,\mathrm{s}$

Table A.2: Parameters used in Sec. 4.4

Name	Unburnt	Burnt	Sc_k
C_3H_8	0.0569794	0	1.241
O_2	0.260046	0.0533094	0.728
CO_2	0	0.170602	0.941
H_2O	0	0.0931139	0.537
N_2	0.682975	0.682975	0.690

Table A.3: Mass fraction composition of fresh and burnt gases used in Sec. 4.3, 4.4, and 4.5. Schmidt numbers (Sc_k) are utilized only in Sec. 4.4. Unity Lewis number is applied in other sections.

Appendix B

F→P chemistry model

This appendix presents the F→P chemistry model, a framework for analyzing simple, irreversible chemical reactions.

An arbitrary single-step, irreversible chemical reaction is represented as:

$$F \rightarrow P \tag{B.1}$$

Here, F represents any reactant transforming into product P. The rate of consumption of reactant F is given by:

$$\dot{\omega}_F = -\rho Y_F A \exp\left(\frac{-\beta(1-\theta)}{1-\alpha(1-\theta)}\right) \tag{B.2}$$

In this equation, $\dot{\omega}_F$ denotes the consumption rate of F, ρ is the density, Y_F is the mass fraction of F, and θ is the progress variable of temperature. The rate of production of P is directly related, with $\dot{\omega}_P = -\dot{\omega}_F$.

The parameter A is defined as:

$$A = B_0 \exp\left(\frac{-\beta}{\alpha}\right) \tag{B.3}$$

where B_0 is the pre-exponential factor. The parameters α and β, representing the flame heat release and the Zel'dovich number (activation temperature), respectively, are given by:

$$\alpha = 1 - \frac{T_f}{T_b} \qquad \beta = \alpha \frac{T_{a1}}{T_b} \tag{B.4}$$

Thermochemical parameters

For the sake of convenience, the NASA 7 coefficient Polynomial system [71] was employed for both the reactant F and product P. These polynomials provide the specific heat (see eq.(1.7)) and heat release values essential for the model. Table B.1 lists these coefficients.

	F	P
W_k	27.9667	27.9667
a_1	3.5	3.5
a_2	0.0	0.0
a_3	0.0	0.0
a_4	0.0	0.0
a_5	0.0	0.0
a_6	0.0	$-(T_b - T_f) * a_1$
a_7	0.0	0.0
a_8	3.5	3.5
a_9	0.0	0.0
a_{10}	0.0	0.0
a_{11}	0.0	0.0
a_{12}	0.0	0.0
a_{13}	0.0	$-(T_b - T_f) * a_1$
a_{14}	0.0	0.0

Table B.1: NASA polynomials for $F \rightarrow P$ chemistry

In addition to the NASA polynomials, several key parameters utilized in the F→P model are given in the table B.2:

Name	Symbol	Value
Fresh gas temperature	T_f	$300\,\mathrm{K}$
Expansion parameter	α	0.75
Zel'dovich number	β	8
Prandtl number	Pr	0.75
Viscosity exponent eq.(1.11)	β_v	0.7
Flame speed	S_l	$3.53\,\mathrm{m\,s^{-1}}$
Thermal diffusivity in unburnt state	D_T^f	$1 \times 10^{-4}\,\mathrm{m^2\,s^{-1}}$
Constant pressure specific heat	C_p	$1040\,\mathrm{J\,kg^{-1}\,K^{-1}}$

Table B.2: Parameters set for $F \rightarrow P$ chemistry

It is crucial to emphasize that we accommodated variations in Lewis numbers by adjusting the Schmidt numbers and modifying parameters such as viscosity and the pre-exponential factor (B_0), while keeping D_T and S_l constant. This approach was essential to ensure consistent comparisons across different scenarios.